

Ultrafast goes local

A dissertation submitted to the
Swiss Federal Institute of Technology Zürich
for the degree of
Doctor of Natural Sciences

presented by
Marc Achermann
Dipl.-Phys. (ETH Zürich)
born on June 11, 1972
citizen of Switzerland

accepted on the recommendation of
Prof. Dr. Ursula Keller, Supervisor
PD Dr. Uwe Siegner, Co-Examiner
date of examination: October 30, 2001

2001

Table of Contents

LIST OF ABBREVIATIONS AND PHYSICAL SYMBOLS.....	V
PUBLICATIONS	IX
ABSTRACT	XIII
KURZFASSUNG	XV
1 INTRODUCTION	1
2 ULTRAFAST NEAR-FIELD SCANNING OPTICAL MICROSCOPE	5
2.1 NEAR-FIELD OPTICS	5
2.1.1 <i>Aperture near-field optical probes</i>	7
2.1.2 <i>Shear-force feedback system</i>	9
2.2 PUMP-PROBE TECHNIQUE	11
2.2.1 <i>Carrier relaxation dynamics</i>	12
2.2.2 <i>Carrier transport dynamics</i>	14
2.3 EXPERIMENTAL SETUP.....	15
2.3.1 <i>Signal-to-noise considerations</i>	18
2.3.2 <i>Maintaining high time resolution in a NSOM</i>	21
2.4 TOPOGRAPHICAL ARTIFACTS.....	24
2.5 SEMICONDUCTOR SAMPLE PREPARATION FOR NF MEASUREMENTS.....	24
2.6 PROOF OF PRINCIPLE OF THE ULTRAFAST NSOM	26
2.6.1 <i>Focused-ion beam implanted quantum well</i>	26
2.6.2 <i>First spatially and temporally resolved measurements</i>	27
3 DIFFERENT DIFFUSIVE TRANSPORT REGIMES IN FOCUSED ION BEAM IMPLANTED SEMICONDUCTOR QUANTUM WELLS.....	31
3.1 EXPERIMENTAL RESULTS IN THE INITIAL DIFFUSION REGIME	31
3.1.1 <i>Spatially dependent time scans</i>	31
3.1.2 <i>Numerical model of the carrier diffusion dynamics</i>	34
3.1.3 <i>Time dependent line scans</i>	37
3.2 EXPERIMENTAL RESULTS IN THE LONG-TIME DIFFUSION REGIME	39

3.3	FIB QW SUMMARY.....	42
4	CARRIER AND FIELD DYNAMICS AROUND NANO-SCALE SCHOTTKY CONTACTS	43
4.1	SAMPLE DESCRIPTIONS AND EXPERIMENTAL SET-UP.....	45
4.1.1	<i>W disk structure</i>	45
4.1.2	<i>LT-GaAs sample</i>	48
4.1.3	<i>Experimental set-up</i>	48
4.2	THEORETICAL MODEL.....	48
4.3	FAR-FIELD EXPERIMENTS	52
4.4	NEAR-FIELD EXPERIMENTS.....	56
4.4.1	<i>Low-density regime</i>	56
4.4.2	<i>High-density regime</i>	61
4.4.3	<i>Annealed LT-GaAs</i>	67
4.5	NANOSCALE W-DISK SUMMARY	68
5	QUANTIZATION ENERGY MAPPING OF SINGLE V-GROOVE GAAS QUANTUM WIRES.....	71
5.1	V-GROOVE GAAS QWRs.....	71
5.2	EXPERIMENTAL RESULTS.....	75
5.2.1	<i>Spatially resolved QWRs</i>	75
5.2.2	<i>Single QWR carrier dynamics</i>	76
5.2.3	<i>QWR quantization energy fluctuations</i>	78
5.3	V-GROOVE QWR SUMMARY	82
6	CONCLUSION AND OUTLOOK	83
	REFERENCES.....	85
	CURRICULUM VITAE.....	95
	DANKSAGUNG.....	97

List of Abbreviations and Physical Symbols

1D	one dimensional
2D	two dimensional
AFM	atomic force microscope
Al	aluminum
AlAs	aluminum arsenide
Al _x Ga _{1-x} As	aluminum gallium arsenide with aluminum content x
AOM	acousto-optic modulator
B	bimolecular recombination constant
CB	conduction band
CCD	charge coupled device
Cr:LiSAF	chromium doped LiSrAlF ₆
D	electric displacement
d	sample thickness
D _a	ambipolar diffusion constant
D _n	electron diffusion constant
D _p	hole diffusion constant
e ⁻	photoexcited electron
E	electric field
E _F	Fermi energy
E _{intern}	internal static electric field
E _X	exciton energy
f _e	distribution function of a photoexcited electron
FF	far-field
f _h	distribution function of a photoexcited hole

FIB	focused-ion beam
FWHM	full width at half maximum
GaAs	gallium arsenide
GaInP	gallium indium phosphide
GVD	group velocity dispersion
h^+	photoexcited hole
HF	hydrofluoric acid
j	current density
LT-GaAs	low-temperature grown gallium arsenide
MBE	molecular beam epitaxy
MOVPE	metalorganic vapor phase epitaxy
n	refractive index
N_d	donor impurity density
NF	near-field
NSOM	near-field scanning optical microscope
OMCVD	organometallic chemical vapor deposition
PL	photoluminescence
q	electron charge
Q_{capt}	capture charge density
QW	quantum well
QWR	quantum wire
R	linear reflectivity
RF	radio frequency
Si	silicon
SPM	scanning probe microscope
STM	scanning tunneling microscope
T	linear transmission
Ti:sapphire	titanium-doped sapphire

U	electric potential
VB	valence band
V_{bi}	built-in potential
w	edge of the depletion zone
W	tungsten
ΔR	pump-induced reflectivity change
ΔT	pump-induced transmission change
Δt	time delay
$\Delta T/T$	normalized differential transmission
Δx	diffraction limit in far-field optics
μ_n	electron mobility
μ_p	hole mobility
$\Delta\alpha$	pump-induced absorption change
α	absorption coefficient
ϵ	dielectric constant
ϵ_0	permittivity in vacuum
λ	vacuum wavelength
θ	opening angle
ρ	carrier density
τ	decay time
τ_D	diffusion decay time
τ_n	electron trapping time
τ_p	hole trapping time
τ_{rec}	recombination time
τ_t	trapping time

Publications

Parts of this thesis are published in the following journal papers and conference proceedings:

Journal Papers

M. Achermann, U. Siegner, U. Keller, "Ultrafast goes local," accepted by *Materials Science Forum*.

M. Achermann, U. Siegner, L.-E. Wernersson, U. Keller, "Nano-scale Schottky contacts: Ultrafast drift-diffusion dynamics studied in the optical near-field," accepted by *Physica E*.

M. Achermann, U. Siegner, L.-E. Wernersson, U. Keller, "Carrier dynamics around nano-scale Schottky contacts: A femtosecond near-field study," accepted by *Appl. Surf. Sci.*

M. Achermann, F. Morier-Genoud, W. Seifert, L.-E. Wernersson, U. Siegner, U. Keller, "Carrier and field dynamics around nano-scale Schottky contacts investigated by ultrafast near-field optics," accepted by *Phys. Rev. B*.

U. Siegner, M. Achermann, U. Keller, "Spatially resolved femtosecond spectroscopy beyond the diffraction limit," **Invited Paper**, *Meas. Sci. Technol.* **12**, 1847-1857 (2001).

M. Achermann, U. Siegner, L.-E. Wernersson, U. Keller, "Ultrafast carrier dynamics around nanoscale Schottky contacts studied by femtosecond far- and near-field optics," *Appl. Phys. Lett.* **77**, 3370-3372 (2000).

S. Schön, M. Haiml, M. Achermann, U. Keller, "Growth and nonlinear optical properties of GaAs absorber layers for AlGaAs/CaF₂ semiconductor saturable absorber mirrors," *J. Vac. Sci. Technol. B* **18**, 1701-1705 (2000).

M. Achermann, B.A. Nechay, U. Siegner, A. Hartmann, D. Oberli, E. Kapon, U. Keller, "Quantization energy mapping of single V-groove GaAs quantum wires by femtosecond near-field optics," *Appl. Phys. Lett.* **76**, 2695-2697 (2000).

M. Achermann, B. A. Nechay, F. Morier-Genoud, A. Schertel, U. Siegner, U. Keller, "Direct experimental observation of different diffusive transport regimes in semiconductor nanostructures," *Phys. Rev. B* **60**, 2101-2105 (1999).

B.A. Nechay, U. Siegner, M. Achermann, H. Bielefeldt, U. Keller, "Femtosecond Pump-Probe Near-Field Optical Microscopy," *Review of Scientific Instruments* **70**, 2758-2764 (1999).

B.A. Nechay, U. Siegner, M. Achermann, F. Morier-Genoud, A. Schertel, U. Keller, "Femtosecond Near-Field Scanning Optical Microscopy," *Journal of Microscopy* **194**, 329-334 (1999).

Conference Papers

M. Achermann, U. Siegner, U. Keller, "Ultrafast goes local," **Invited Talk**, *11th Symposium on Ultrafast Phenomena in Semiconductors (11 UFPS)*, Vilnius, Lithuania, 2001.

M. Achermann, U. Siegner, L.-E. Wernersson, U. Keller, "Nano-scale Schottky contacts: Ultrafast drift-diffusion dynamics studied in the optical near-field," Poster, *10th International Conference on Modulated Semiconductor Structures (MSS10)*, Linz, Austria, 2001.

M. Achermann, U. Siegner, L.-E. Wernersson, U. Keller, "Carrier dynamics around nano-scale Schottky contacts: A femtosecond near-field study," *International conference on the formation of semiconductor interfaces (ICFSI-8)*, Sapporo, Japan, 2001.

M. Achermann, U. Siegner, L.-E. Wernersson, U. Keller, "Carrier dynamics around nano-scale Schottky contacts studied by femtosecond near-field optics," Poster, *International Quantum Electronics and Laser Science Conference (QELS2001)*, Baltimore, Maryland, USA, 2001.

S. Schön, M. Haiml, L. Gallmann, M. Achermann, U. Keller, "Novel semiconductor materials and saturable absorber mirrors for sub-10-femtosecond pulse generation," **Invited Talk**, *Conference on Optoelectronic and Microelectronic Materials and Devices (COMMAD 2000)*, Melbourne, Australia, 2000.

M. Achermann, U. Siegner, B.A. Nechay, A. Hartmann, D. Oberli, E. Kapon, U. Keller, "Ultrafast SNOM," **Invited Talk**, *NFP36 Closing Meeting*, Bern, Switzerland, 2000.

M. Achermann, U. Siegner, B.A. Nechay, A. Hartmann, D. Oberli, E. Kapon, U. Keller, "Femtosecond near-field spectroscopy of single V-groove GaAs quantum wires," Poster, *NFP36 Closing Meeting*, Bern, Switzerland, 2000.

M. Achermann, U. Siegner, B.A. Nechay, A. Hartmann, D. Oberli, E. Kapon, U. Keller, "Femtosecond near-field spectroscopy of single V-groove GaAs quantum wires," *International Conference on Near Field Optics and Related Techniques (NFO-6)*, Twente, Netherlands, 2000.

M. Achermann, U. Siegner, B.A. Nechay, U. Keller, A. Hartmann, Y. Ducommun, D. Oberli, E. Kapon, "Characterization of quantization energy fluctuations in single quantum wires by femtosecond near-field optics," *International Quantum Electronics and Laser Science Conference (QELS2000)*, San Francisco, California, USA, 2000.

M. Achermann, U. Siegner, B.A. Nechay, Y. Ducommun, A. Hartmann, D. Oberli, E. Kapon, U. Keller, "Ultrafast SNOM measurements in semiconductor nanostructures," *International Conference on Nanoscale Optics*, Engelberg, Switzerland, 2000.

S. Schön, M. Haiml, M. Achermann, U. Keller, "Growth and nonlinear properties of GaAs absorber layers for AlGaAs/CaF₂ SESAMs," *18th North American Conference on Molecular Beam Epitaxy (NAMBE'99)*, Banff, Canada, 1999.

M. Achermann, B.A. Nechay, U. Siegner, U. Keller, "Ultrafast Carrier Dynamics in Semiconductor Nanostructures Studied by Femtosecond Scanning Near-field Optical Microscopy," Poster, *Nanoforum CH-US*, Zürich, Switzerland, 1999.

B.A. Nechay, M. Achermann, F. Morier-Genoud, A. Schertel, U. Siegner, U. Keller, "Femtosecond near-field spectroscopy of spatiotemporal carrier dynamics in locally disorder-patterned quantum wells," *International Quantum Electronics and Laser Science Conference (QELS'99)*, Baltimore, Maryland, USA, 1999.

B. A. Nechay, U. Siegner, M. Achermann, F. Morier-Genoud, A. Schertel and U. Keller, "Femtosecond near-field optical spectroscopy," *International Conference on Near Field Optics and Related Techniques (NFO-5)*, Shirahama, Japan, 1998.

B.A. Nechay, U. Siegner, M. Achermann, A. Schertel, F. Morier-Genoud, U. Keller, "Femtosecond-Resolved Scanning Near-Field Optical Microscopy," **Invited Talk**, *Workshop on Nanoscience*, Hasliberg, Switzerland, 1998.

Seminar talks

M. Achermann, "Ultrafast goes local," Solid State Physics/Nanometer Structure Consortium, Lund University, Sweden, August 2001.

M. Achermann, "Femtosecond scanning near-field optical microscope," Institute of Micro- and Optoelectronics, EPFL Lausanne, Switzerland, September 1999.

M. Achermann, "Ultrafast scanning near-field optical microscope," Tutorial at Zurich SNOM seminar, ETH Zurich, Switzerland, May 1999.

Abstract

In this thesis, we demonstrate the remarkable performance of a technique that connects the *ultrafast*, femtosecond regime with the *local*, nanometer world. The combination of the ultrafast pump-probe technique with near-field scanning optical microscopy allows to perform optical spectroscopy with simultaneous 250 fs temporal and 150 nm spatial resolution. Such spatiotemporal resolution obtained with the ultrafast near-field scanning optical microscope (NSOM) is crucial for transport studies in nanostructured materials, for the study of carrier dynamics in single nanostructures as well as for the characterization of inhomogeneities in nanostructured ensembles.

The design of an ultrafast NSOM has to be very deliberate. We employ a configuration in which carriers are excited globally by a far-field pump laser pulse and locally measured by a probe pulse sent through an NSOM tip and transmitted through the sample in the near field. A novel detection system allows for either two-color or degenerate pump and probe photon energies, permitting greater measurement flexibility over earlier published work. The capabilities of this instrument are proven through near-field degenerate pump-probe studies of carrier dynamics in GaAs/AlGaAs single quantum well samples locally patterned by focused-ion beam (FIB) implantation.

The details of the measured carrier dynamics in the FIB implanted quantum well sample reveal complex spatiotemporal diffusion dynamics. Implantation induced trapping centers cause carrier density gradients, which are the driving forces for diffusion. The diffusion dynamics is directly observed by measuring carrier density variations in both time and space. A comprehensive experimental study allows us to identify different diffusion regimes. We find an initial diffusion regime, characterized by non-sinusoidal carrier profiles and spatially dependent temporal diffusion decay. In a long-time regime, the carrier profile is quasi-sinusoidal and only weakly position-dependent temporal diffusion decay is observed.

Femtosecond NSOM can also disentangle more complex transport dynamics that involve both carrier drift and carrier diffusion. Such dynamics occurs in metal-semiconductor composite materials, where buried Schottky contacts and

built-in electric fields are formed at the semiconductor-metal interface. We have performed femtosecond NSOM measurements that reveal the dynamics of carrier transfer from a semiconductor into embedded metal clusters in the presence of Schottky contacts and built-in electric fields. The carrier transfer involves transport towards and trapping into the metal clusters. Our experiments show that efficient transport of electrons towards the metal only occurs at higher carrier densities. For these densities, the built-in field is screened. Only in this case, the metal clusters act as efficient trapping centers for electrons.

Beside transport measurements, studies of single nanostructures, such as low-dimensional systems, are one of the most important applications of the femtosecond NSOM technique. Such studies allow one to gain insight into the intrinsic properties of nanostructures, unperturbed by spatial averaging over an ensemble of structures. Moreover, growth inhomogeneities in nanostructured materials can be characterized. As an example, experiments on single one-dimensional semiconductor quantum wires (QWRs) are discussed. We demonstrate that femtosecond NSOM measurements on single V-groove QWRs are possible and reveal ultrafast exciton relaxation dynamics. Furthermore, a novel method is presented for the mapping of quantization energy fluctuations along single quantum wires with nanometer-scale spatial resolution.

Kurzfassung

In dieser Arbeit stellen wir die bemerkenswerte Leistungsfähigkeit einer Technik vor, die den *ultrakurzen* Femtosekunden-Bereich mit der *lokalen* Nanometer-Welt verbindet. Die Kombination von Ultrakurzzeit Pump-Probe Spektroskopie mit Nahfeld Mikroskopie ermöglicht optische Untersuchungen mit gleichzeitig hoher Zeit- und Ortsauflösung. Unser selbst gebautes sogenanntes Ultrakurzzeit Rasternahfeld-Mikroskop (NSOM) erlaubt Messungen mit einer Raumzeitauflösung von 150 nm / 250 fs. Mit diesem Instrument ist es dadurch möglich, Transport in nanostrukturierten Materialien zu studieren, Ladungsträgerdynamik in einzelnen niedrig-dimensionalen Systemen zu untersuchen oder Inhomogenitäten in nanostrukturierten Ensembles zu charakterisieren.

Das Ultrakurzzeit NSOM muss konzeptionell sehr gut durchdacht sein, damit seine Leistungsfähigkeit voll genutzt werden kann. Wir wenden eine Konfiguration an, bei der Ladungsträger global durch einen Fernfeld Laserpuls angeregt werden und deren Dynamik dann lokal durch einen Testpuls im Nahfeld ausgelesen wird. Ein neuartiges Detektionssystem berücksichtigt sowohl zwei Farben wie auch entartete Pump- und Probephotonenenergien, womit eine höhere Flexibilität gegenüber früheren Arbeiten erreicht wird. Das Leistungsvermögen des Instruments wird demonstriert durch zeitaufgelöste entartete Nahfelduntersuchungen der Ladungsträgerdynamik in GaAs/AlGaAs Quantenfilmen, welche lokal durch einen fokussierten Ionenstrahl (FIB) bearbeitet wurden.

Die Details der gemessenen Ladungsträgerdynamik im FIB implantierten Quantenfilm zeigen komplexe Diffusionsdynamik. Durch die Implantation erzeugte Haftzentren bewirken Ladungsträgergradienten, welche als treibende Kräfte für Diffusion agieren. Die Diffusionsdynamik wird direkt betrachtet durch Messung der räumlichen und zeitlichen Variationen der Ladungsträgerdichte. Wir stellen fest, dass die anfängliche Diffusionsdynamik charakterisiert ist durch nicht sinusförmige Ladungsträgerdichteprofile und räumlich abhängige Zerfallszeiten. Auf einer längeren Zeitskala hingegen ist das

Ladungsträgerdichtepprofile quasi sinusförmig und der Dichtezerfall hängt nur noch schwach von der Position ab.

Das Femtosekunden NSOM kann auch kompliziertere Transportdynamik entflechten, wenn sowohl Drift wie auch Diffusion involviert ist. Solche Dynamik findet man in Metall-Halbleiter Verbundmaterialien, in denen Schottkykontakte und elektrische Felder an der Halbleiter-Metallgrenzfläche vorhanden sind. Die durchgeführten Nahfeldmessungen erörtern die Transferdynamik von Ladungsträgern aus einem Halbleiter in eingebettete Metallkugeln hinein unter dem Einfluss von Schottkykontakten und eingebauten elektrischen Feldern. Unsere Experimente zeigen, dass effizienter Elektronentransport zum Metall nur bei hohen Ladungsträgerdichten vorkommt. Bei diesen Dichten sind die eingebauten Felder abgeschirmt. Nur in diesem Fall können die Metallkugeln die Elektronen effizient einfangen.

Neben Transportmessungen ist die Erforschung einzelner Nanostrukturen, wie z.B. niedrig-dimensionaler Systeme, eines der wichtigsten Anwendungsgebiete der Femtosekunden NSOM Technik. Dabei wird ein Einblick in die spezifischen Eigenschaften der Nanostruktur gewonnen, ungestört vom räumlichen Mittel über ein Ensemble von Strukturen. Ausserdem können Wachstumsinhomogenitäten in nanostrukturierten Materialien charakterisiert werden. Als Beispiel werde Experimente an einzelnen eindimensionalen Quantendrähten (QWRs) diskutiert. Wir zeigen, dass Femtosekunden NSOM Messungen an QWRs möglich sind und dadurch schnelle Exziton Relaxationsdynamik untersucht werden kann. Zudem wird eine neuartige Methode vorgestellt, um Fluktuationen der Quantisierungsenergie entlang einzelner Quantendrähte mit einer räumlichen Auflösung im Nanometerbereich aufzuzeichnen.

1 Introduction

Many fundamental physical processes in condensed matter and molecular and atomic systems take place on picosecond or sub-picosecond time scales. Examples include the vibrational motion of molecules [1], redistribution of charge carriers in the bands of semiconductors [2] and electron dynamics in metals [3, 4]. Though a variety of measurement techniques can probe such dynamical processes, only all-optical techniques have reliably achieved subpicosecond temporal resolution. Therefore, ultrafast optical spectroscopy techniques have substantially contributed to our understanding of fundamental physics as well as to the characterization and optimization of electronic and optoelectronic devices [1, 2].

In most femtosecond-resolved experiments, the information about the dynamic processes is spatially averaged. Spatial averaging occurs over an area with a typical diameter of 10-100 μm , determined by the beam diameter of the femtosecond laser with which the experiment is performed. This averaging is particularly disadvantageous if dynamic processes are investigated in nanostructured materials since their inherent inhomogeneity cannot be spatially resolved. Given the great potential of nanostructured devices for applications in photonics and electronics [5], the development of femtosecond-resolved measurement techniques with nanometer spatial resolution is called for. The same conclusion is reached if one considers studies of real-space transport. For example, an electron moving in the semiconductor GaAs at the saturation drift velocity of approximately 10^7 cm/s moves over a distance on the order of 100 nm in 1 ps. Thus, time-resolved studies of such transport processes will substantially benefit from nanometer-scale spatial resolution.

The most promising approach to achieve both high spatial and high temporal resolution is given by *ultrafast local probes*. These techniques combine ultrafast optical spectroscopy techniques with scanning probe microscopy (SPM). Possible local probe techniques include Scanning Tunneling Microscopy (STM) [6], Atomic Force Microscopy (AFM) [7] and Near-Field Scanning Optical

Microscopy (NSOM)¹ [8-10]. Ultrafast SPM techniques use internal nonlinearities inherent in STM, AFM and NSOM systems, as well as external nonlinearities added to these systems, such as external gating.

Historically, the first local ultrafast measurements have been performed with an ultrafast AFM [11] in 1992. In these experiments ultrafast voltage waveforms on a high-speed circuit were measured. The technique is based on the detection of the force between the tip and the sample that depends on the square of the voltage between tip and sample. This nonlinearity allows to sample the ultrafast signal waveform with ultrafast sampling pulses applied to the AFM tip, which acts as an extremely high-speed mixer. Not much later, in 1993, ultrafast measurements with STMs [12-14] were reported. In Ref. [12] the intrinsic nonlinearity of the I-V characteristic was used to measure ultrafast voltage pulses in transmission lines created by photoconductive switches. In Ref. [13, 14] ultrafast waveforms on transmission lines were sampled externally using a photoconductive switch on the STM tip. However, since both the ultrafast AFM and STM techniques rely either on photoconductive switches as time-gating devices or on electronics, it seems doubtful whether the time resolution can be pushed to the 100 fs range. All-optical techniques based on NSOM are much more promising in this respect.

Starting in 1995, femtosecond-resolved NSOM experiments have been reported by several groups [15-28]. Temporal and spatial resolutions in the 100 fs and 100 nm range, respectively, have been achieved. Besides the good temporal and spatial resolution, the ultrafast NSOM is particularly successful, as it combines near-field (NF) techniques with conventional well-known time-resolved optical spectroscopy techniques. Examples include degenerate equal pulse correlation, luminescence intensity autocorrelation and the most widely used degenerate or two-color pump-probe technique. Thus, time-resolved all-optical near-field microscopy has been established by now as an experimental

¹ The use of the term NSOM is not universal. The alternative term SNOM, which was introduced by the IBM group in Switzerland, stresses the scanning aspects of the instrument. This name also underscores the instrument's heritage as a member of the scanning probe microscope family. The term NSOM was suggested by the Cornell group in the United States. This name stresses instead the near-field aspects of the instrument.

tool that provides both spatial resolution beyond the diffraction limit and true femtosecond time resolution.

In this thesis, we will introduce the femtosecond near-field scanning optical microscope and show that its high performance allows for the measurement of ultrafast carrier dynamics in a variety of semiconductor nanostructures. In chapter 2, we first give an introduction to the conventional NSOM technique with some details on the fabrication of NSOM tips by tube etching and on the used shear-force feedback technique to keep the NSOM tip in a small distance above the sample. Afterwards we introduce the pump-probe technique and discuss shortly general carrier relaxation and transport dynamics in semiconductors. We then describe how the pump-probe technique has been combined with the NSOM technique to resolve spatiotemporal carrier dynamics with 150 nm spatial and 250 fs temporal resolution. Particular attention is devoted to the dispersion management in order to maintain good temporal resolution.

Typical ultrafast near-field experiments can be placed into two categories: (i) studies of real-space carrier transport and (ii) measurements on single nanostructures. With respect to transport studies, we have performed measurements on two different structures. Chapter 3 deals with diffusive carrier transport in semiconductor quantum wells, which have been patterned by local ion implantation. The implantation induces local carrier trapping, giving rise to a locally reduced carrier density. The resulting density gradients are the driving forces for the measured diffusive carrier transport. The extension to more complicated drift and diffusion dynamics is performed in chapter 4. In this chapter we study carrier transport in metal-semiconductor composite materials. They are characterized by the presence of buried metallic nanodisks. These nanodisks can trap carriers at the interface and form Schottky contacts to the embedding semiconductor. The resulting built-in electric fields induce drift forces on the carriers in addition to diffusion and trapping mechanisms. In both chapters 3 and 4, the measured carrier dynamics is successfully compared with numerical simulations of the carrier density dynamics.

Measurements on single nanostructures aim to provide a better understanding of the intrinsic properties of these structures. Often, insight into the intrinsic properties is difficult to obtain from far-field experiments, which average over the response of an ensemble of nanostructures. This averaging complicates the interpretation of the experimental data. Moreover, measurements on single

nanostructures allow the characterization of the inhomogeneity of the structures. In chapter 5, we present experiments on single semiconductor quantum wires. Local measurements allow for the interpretation of ultrafast carrier relaxation dynamics in a single quantum wire. Additionally, the analysis of the experimental data demonstrates that femtosecond NSOM measurement allow one to quantitatively determine fluctuations of optical transition energies along a single quantum wire with nanometer-scale spatial resolution. Information on the fluctuation in thickness of the wire can be obtained from these measurements. Finally, we present our conclusions and an outlook in chapter 6.

2 Ultrafast near-field scanning optical microscope

In this chapter we establish a basis for the experiments described in the chapters 3 - 5. First we introduce the fundamental ideas of near-field optics, which allow us to obtain sub-diffraction limit spatial resolution. More details are given to the formation of near-field optical probes and the used shear-force feedback system. Subsequently, the basics of femtosecond pump-probe spectroscopy are explained, including a short description of carrier relaxation and transport dynamics in semiconductors. The combination of NF optics and pump-probe spectroscopy results in our femtosecond NSOM, which is specified in the section on the experimental setup. We discuss the special requirements that are necessary to perform pump-probe measurements with simultaneously high temporal and spatial resolution. Finally, we demonstrate that the home-built femtosecond NSOM allows for the measurement of carrier dynamics in a patterned semiconductor quantum well with simultaneous 150 nm spatial and 250 fs temporal resolution and a high sensitivity of $\Delta T/T < 10^{-4}$.

2.1 Near-field optics

Recently, strong technological progress has pushed near-field optics to one of the cutting edge technologies in microscopy [29-43]. The success of the NSOM is based on the fruitful combination of scanning probe technology with the power of optical microscopy, which allows us to directly look into the nanoworld. Up to date research fields include single molecule spectroscopy [30-32], low dimensional electronic [33-35] and photonic structures [36, 37], surface plasmons [38, 39], etc. Also for theorists the optical near-field has become very attractive [40-43].

So far, the spatial resolution of conventional visible far-field optics has been limited roughly to the micrometer as a consequence of the diffraction limit. Already in 1873, Ernst Abbé [44] found, that there is a lower barrier for the smallest resolvable spacings Δx :

$$\Delta x = \frac{\lambda}{2n \sin \theta} \quad (2.1)$$

where λ is the wavelength, n the refractive index of an embedding medium and θ the aperture angle in the medium that may be a liquid or even a solid.

The first idea to circumvent the diffraction limit in order to obtain spatial resolution in the 100 nm range was proposed in 1928 by E.H. Syngé [45]. He suggested to illuminate an opaque metallic film from the backside with a strong light source. A small hole with a 100 nm diameter drilled in the metallic film should then act as a very local light source (Fig. 2.1(a)). Images were taken by raster scanning point by point the hole in a very short distance below 100 nm over the sample to guarantee the spatial resolution. In fact, this theoretical description comes very close to the modern NSOM instrument. However for technological reasons, the theoretical concept had never been realized by Syngé. Only in 1984 the first NF optical microscopes have been developed at IBM R schlikon by D. Pohl et al. [8] and independently at the Cornell University by A. Lewis et al.[9]. Both groups used so called aperture NSOMs. In such instruments light is coupled into an sharply tapered transparent probe tip that is metal coated, leaving a sub-wavelength aperture at the tip apex (Fig. 2.1(b)). Using a feedback system similar to the ones used in other SPM systems, the tip is raster scanned in close proximity over the sample, maintaining a constant tip-sample separation. The light emerging from the aperture is scattered by the sample and detected in the far-field with a photodetector. With such aperture NSOMs a spatial resolution below 50 nm can be routinely achieved nowadays.

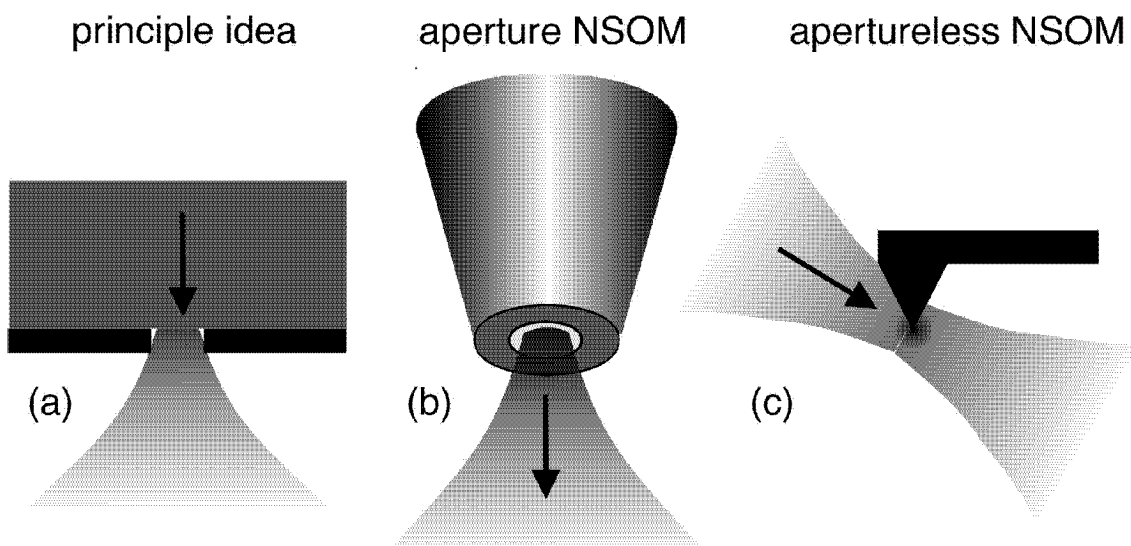


Fig. 2.1 Different schemes for NF optical microscopes: (a) first theoretical concept proposed by Syng , (b) conventional widespread aperture NSOM and (c) apertureless NSOM, based on local field enhancement at sharp probe tips.

Improved spatial resolution has been recorded by the apertureless NSOM [46-49]. This instrument takes advantage of the local field enhancement occurring when a strong laser beam is focused in the far-field on a very sharp probe tip (Fig. 2.1c)). The very confined optical field has shown to give a spatial resolution down to a few nanometer in laboratory experiments [46-49]. The strong drawback of the apertureless technique is the huge background signal of far-field scattered radiation that overshadows the small NF optical signal. Additionally, the interpretation of the measured signal can be difficult due to the strong dependency of the local field enhancement on the geometry of the probe tip and the topography of the measured sample. Therefore numerical simulations have often to be considered for the interpretation of the measured data.

In this work we have used a conventional aperture NSOM for the time-resolved measurements. In the following we will describe the two main elements of the NSOM, that are the aperture probe tip and the feedback mechanism.

2.1.1 Aperture near-field optical probes

Since the first publications of the aperture NSOM, there have been various attempts for the realization of high quality probe tips. The main quality factors concern reproducibility and throughput. The most successful techniques with respect to this considerations are pulling or etching of single-mode optical fibers. These techniques are widely used today, although they both suffer from the lack of the possibility for mass production. The power throughputs, for a 100 nm aperture at ~ 800 nm wavelengths, are typically 10^{-6} - 10^{-4} for pulled tips and 10^{-5} to 10^{-3} for etched tips. The throughput for etched tips is generally larger due to a larger cone angle, which minimizes the distance over which evanescent modes near the tip aperture must propagate, thereby minimizing the power loss. For both types of tips, the power throughput strongly depends on the aperture diameter d , as d^4 from the Bethe/Bouwkamp model [50, 51]. Therefore, a better spatial resolution comes at a great cost of useable signal power. However, the maximum input power is limited to a few mW by the damage threshold of the Aluminum fiber coating [52, 53], resulting in a NSOM fiber output for a 100 nm aperture of typically less than 100 nW.

The pulling method [54] is based on local heating of an optical fiber by a CO₂ laser or a filament and subsequent pulling apart. The advantage of the method

is the smooth surface at the apex that allows for the evaporation of metal layers without leakage holes. We have used probe tips of this type for initial measurements, but then abandoned them because of the poor throughput.

The etching technique produces probe tips by dipping the optical fibers in a 40% HF solutions [55] with an overlayer of an organic solvent (e.g. p-xylene C_8H_{10} or isooctane C_8H_{18}). The organic solvent is used to avoid evaporation of the HF, which would attack the entire fiber and not only the part dipped in the HF. The probe tips we used in our experiments were fabricated by the more elaborate tube-etching technique [56, 57]. In this method, the optical fibers are dipped *with the polymer coating* in the HF solution for 2-3 hours. The exact etching time depends on the brand and exact chemical composition of the optical fiber and the polymer coating. The self-terminating tip formation process is schematically shown in Fig. 2.2 at different stages. The polymer coating forms a cylindrical cavity around the tip during the etching, which results in a reduced surface roughness and therefore in an increased quality of the probe tips. After the etching the polymer coating is removed either by dissolving it into dichloromethane (CH_2Cl_2) or by mechanical stripping.

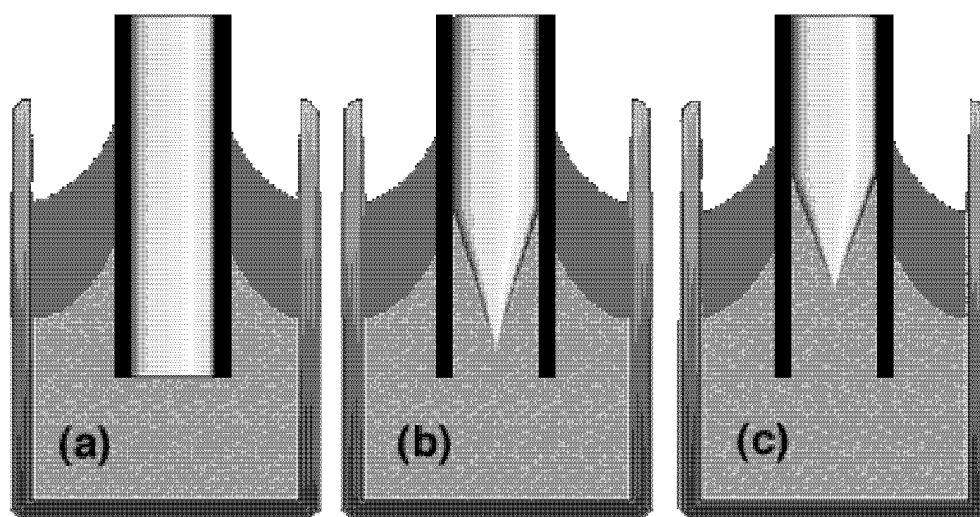


Fig. 2.2 Tube etching process at different stages (a) right after dipping the optical fiber in the HF solution, (b) during the etching, and (c) after the self-terminating formation of the probe tip. The polymer tube that is not removed during the etching is shown in black.

Subsequently, the bare etched fiber is metal coated. The evaporation is performed under a slight angle of $\sim 5^\circ$ from behind (Fig. 2.3). Due to the shadowing effect, the deposition rate is considerably reduced at the apex of the

tip compared to the sides resulting in the formation of an aperture at the tip apex. During the evaporation, the tip is rotated at a frequency of 2-5 Hz to ensure a homogenous metal layer thickness. First we evaporate a few monolayers of titanium at an evaporation rate of 3 Å/s. This layer acts as a sticking layer for the subsequent aluminum layer. It has been shown, that such a sticking layer rises the optical damage threshold [58]. For the confinement of the light we evaporate a ~70 nm thick aluminum coating at a rate of 1-2 nm/s. The thickness of the Al coating ensures that no light is leaking sideward out of the probe tip (the skin depth of Al at 800 nm is 7.5 nm).

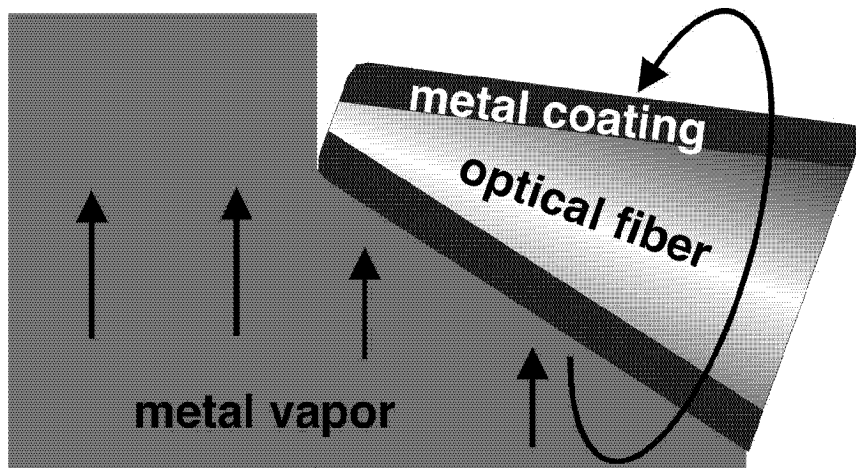


Fig. 2.3 The aperture at the tip apex is formed by evaporating metal on the taper sides under a small angle from behind.

2.1.2 Shear-force feedback system

Already Synge [45] suggested that in a NSOM experiment, the subwavelength aperture must be placed very close to the sample surface of interest. Synge's intuition was correct. Theoretical studies of the behavior of the electromagnetic near-field of a subwavelength aperture show it to be strongly diverging, except very near the aperture, i.e. for $z \ll \lambda$. Small tip-sample separations even during raster scanning can only be kept constant, when the tip-sample distance is actively controlled over a sensitive feedback loop. Among different feedback mechanisms known from other SPM techniques, shear-force feedback control [59] is currently the most popular one used for NSOMs. Our shear-force feedback control system based on a piezoelectric tuning fork [60] is depicted in Fig. 2.4. This kind of feedback technique avoids the effect of scattered light which can be present in optical feedback techniques.

For the shear-force feedback control, the optical fiber is glued on one leg of a 32'768 Hz quartz tuning fork from Grieder Bauteile AG. The tip together with the tuning fork are dithered laterally by the dither-piezotube at one of the resonance frequencies around 31-37 kHz, depending on the fiber shape and the exact mounting geometry. Best feedback conditions are found for resonances with ~150 Hz FWHM. The dithering leads to an oscillation of the tip apex with an amplitude of around 5 nm. The movement of the tip is transformed to a voltage signal by the piezo-electric tuning fork. Using a lock-in amplifier at the driver frequency, the amplitude of the oscillation is extracted.

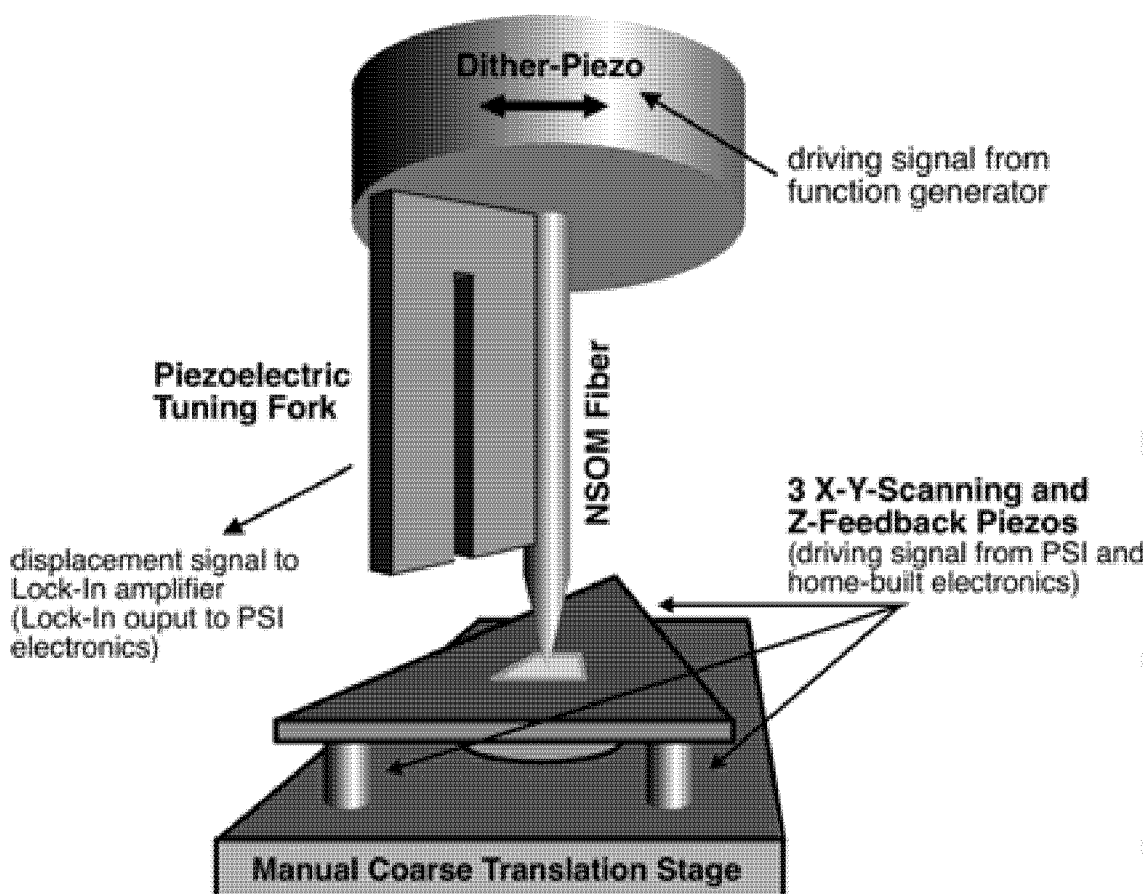


Fig. 2.4 Piezoelectric tuning fork shear force feedback system and scanner unit, driven by Park Scientific Instruments (PSI) or home-built electronics.

As the fiber is brought to within roughly 15 nm of the surface, the resonance is damped due to shear forces that act between tip and sample. As the tip-sample separation goes to zero, the tip amplitude becomes zero. By maintaining a constant tip oscillation amplitude, a constant tip-sample separations is obtained. The constant tip-sample flying height is controlled over a commercial Park Scientific Instruments AFM, which drives the z-feedback piezos of the sample

holder. Thus, while recording the distance necessary to move the sample to maintain this constant tip oscillation, one records a topographic image simultaneously with the NSOM image. The x-y raster scanning is performed by the three sample holder piezos.

The sample stage design and coarse and fine tip approach systems are similar to the designs described in Ref. [61], Secs. 5.4.3 and 5.5, respectively. The coarse sample positioning is done with manual translation stages.

2.2 Pump-probe technique

In order to obtain femtosecond time resolution, in all but a few cases the pump-probe technique has been combined with NSOM [15, 16, 18-26, 28]. In the context of this thesis, "pump-probe" refers to measurements of either the differential reflectivity or the differential transmission [2, 62]. In these pump-probe experiments, a pump pulse excites carriers in the sample. The excited carriers modify the absorption and the refractive index and, in turn the reflectivity and the transmission of the sample. The pump-induced reflectivity or transmission changes are measured by a probe pulse at various time delays Δt after the pump excitation, as shown in Fig. 2.5. The time delay Δt is adjusted by a mechanical delay stage.

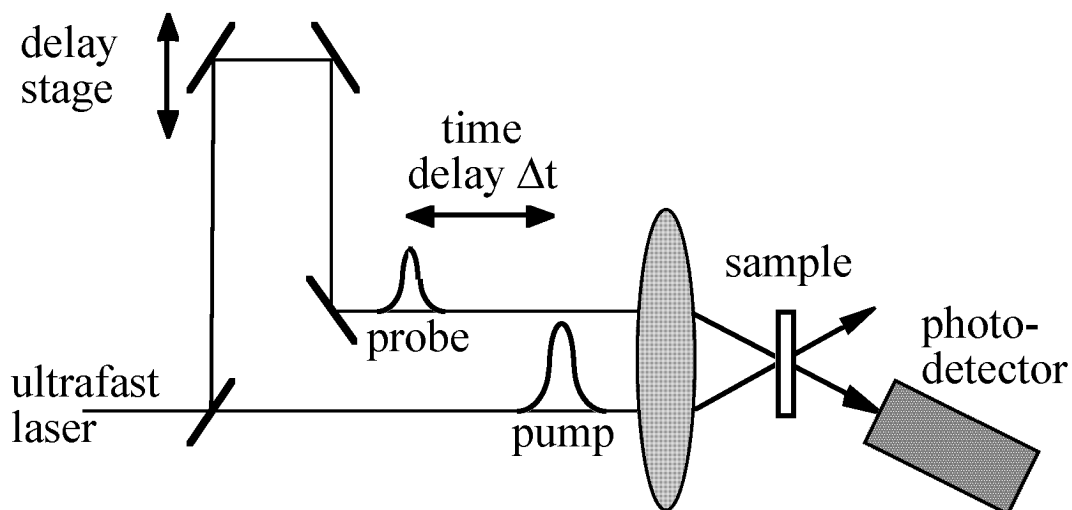


Fig. 2.5 Scheme of the pump-probe technique. The pump-induced transmission changes are measured with a probe pulse as a function of pump-probe time delay Δt .

More specifically, the pump-induced changes of the reflected or transmitted probe intensity are determined, which are proportional to the "differential reflectivity" $\Delta R = R_{\text{pump on}} - R$ and the "differential transmission" $\Delta T = T_{\text{pump on}} - T$, respectively. Here, T is the linear transmission of the sample and R its linear reflectivity. The time resolution in these experiments is only determined by the width of the pump and probe pulses. In this work, we will mainly concentrate on the differential transmission technique.

After coherence is lost, the differential transmission signal is determined by many-body effects (e.g. band gap renormalization or exciton energy changes) and occupation effects. In samples and under experimental conditions, where many-body effects can be neglected and occupation effects dominate the dynamics, the analysis of the experiments is considerably simplified. Assuming a constant matrix element for the interband transitions in the spectral region of interest, the pump induced change in the absorption coefficient α is given by [2]:

$$\Delta\alpha(\omega) = -(f_e + f_h)\alpha(\omega) \quad (2.2)$$

where f_e and f_h are the photoexcited electron and hole distribution functions at energies E_e and E_h , respectively, coupled by a photon of energy $\hbar\omega$. Under the simplifying assumptions that changes in reflectivity can be neglected and that the absorption changes $\Delta\alpha$ in a thin sample with thickness d are small, we can write the normalized differential transmission as:

$$\frac{\Delta T(\omega, \Delta t)}{T(\omega)} = \frac{T_{\text{pump on}}(\omega, \Delta t) - T(\omega)}{T(\omega)} = -\Delta\alpha(\omega, \Delta t)d \quad (2.3)$$

Hence, with the described simplifications, we conclude from Eq. 2.2 and 2.3 that the differential transmission signal is a measure for the excited carrier density. As a consequence, measurements of the differential transmission versus the time delay between the pump and the probe pulses reveal the temporal evolution of the carrier distribution.

2.2.1 Carrier relaxation dynamics

In general, the relaxation of photoexcited carriers in semiconductors to the thermodynamic equilibrium can be classified roughly into four time-regimes (see Fig. 2.6). In the first, coherent regime I the excitation in the semiconductor is in

a well-defined phase relationship with the electromagnetic field of the pump pulse. The coherence is destroyed by various scattering processes, such as carrier-carrier scattering, momentum scattering, etc. Typical dephasing times of e.g. free carriers in GaAs at room temperature are on the order of 10 fs [63, 64].

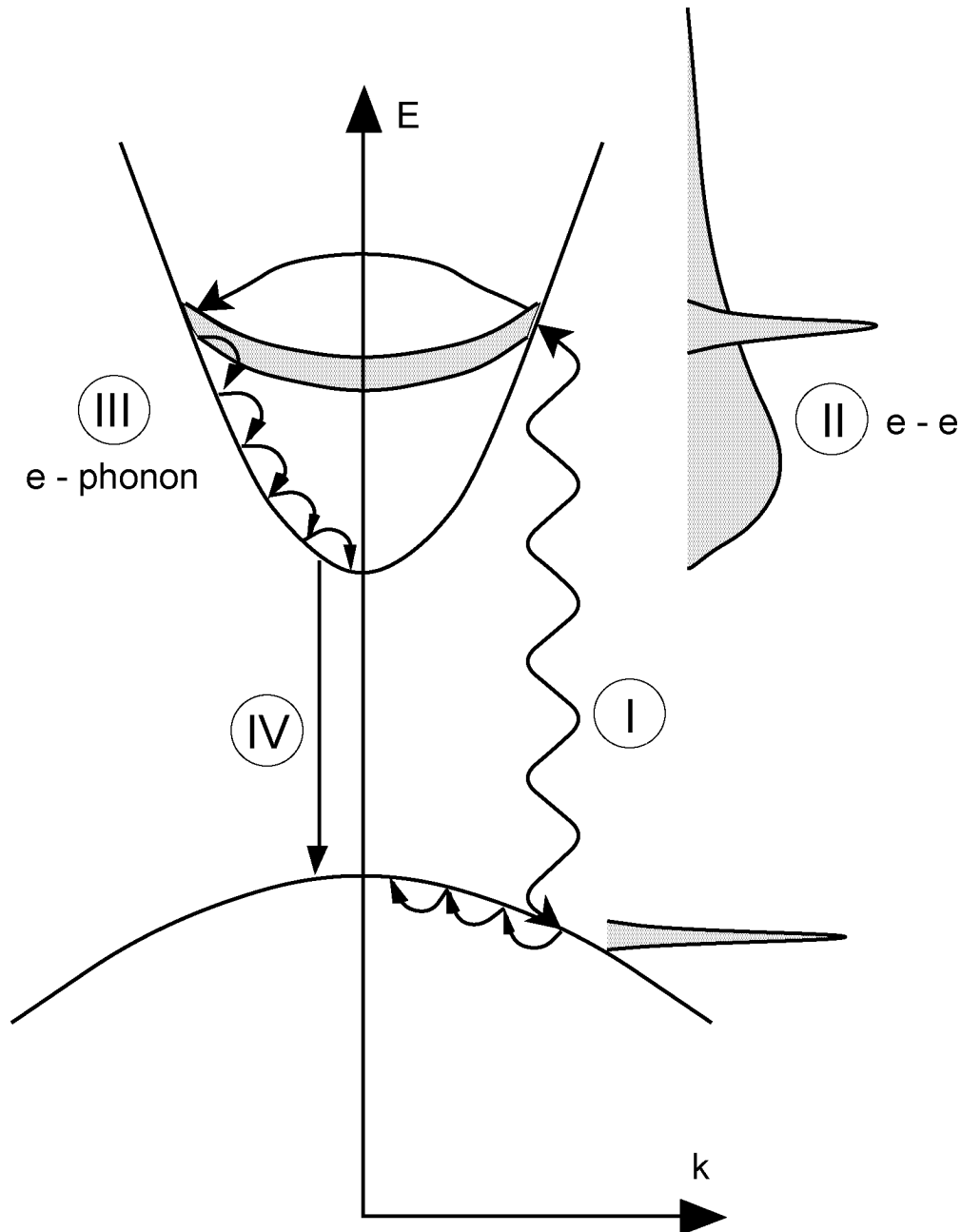


Fig. 2.6 The four carrier regimes that are significant for the relaxation of ultrafast excited carriers, depicted for a 2-band bulk semiconductor: Coherent regime I, non-thermal regime II, hot-(cold)-carrier regime III, and isothermal regime IV.

After the dephasing, the distribution of the free electron-hole pairs or excitons is non-thermal (regime II), i.e. the carrier distribution can not be characterized by a

temperature. Mainly carrier-carrier scattering evolves the non-thermal carrier distribution to a hot or cold thermal carrier distribution. The thermalization process in the case of electrons in GaAs takes place in around 200 fs [65, 66]. The thermalized carrier distribution has normally a higher or lower temperature than the lattice temperature, depending on the excitation photon energy and the excited carrier density. In the third hot-(cold)-carrier regime III the electron-hole pairs are cooled (heated) and reach the lattice temperature on a picosecond time-scale through interaction with various phonons in the semiconductor [2]. Finally all carriers, phonons and excitons are in equilibrium with each other and can be described by a single temperature, the one of the lattice. In this isothermal regime IV the excess electron-hole pairs or excitons recombine radiatively or non-radiatively and return to the thermodynamic equilibrium before optical pulse excitation.

It has to be highlighted that the four regimes temporally overlap. For example in samples with a high amount of defects, the electron-hole pairs can recombine non-radiatively on a very short time-scale of a few picoseconds.

For our femtosecond NSOM with a temporal resolution of ~250 fs coherent carrier dynamics is not accessible. We are only interested in carrier dynamics that play on a longer time scale of a few hundreds of femtosecond to hundreds of picoseconds.

2.2.2 Carrier transport dynamics

One of the most important features of a temporally and spatially resolving technique like the ultrafast NSOM is the ability to investigate the dynamics of lateral carrier transport. In chapter 3 and 4 we will describe carrier transport driven by carrier density gradients and electric fields, resulting in carrier diffusion and drift, respectively. The underlying theoretical description for the transport dynamics is the continuity equation:

$$\frac{\partial}{\partial t} \rho(t, \mathbf{x}) = -\nabla \cdot \mathbf{j}(t, \mathbf{x}) \quad (2.4)$$

where ρ is the carrier density and \mathbf{j} the current density. In the non-ballistic regime the current density consists of a diffusion and a drift term:

$$\mathbf{j}(\mathbf{x}) = \mathbf{j}_{diffusion}(\mathbf{x}) + \mathbf{j}_{drift}(\mathbf{x}) = -D\nabla\rho(\mathbf{x}) + \mu\rho(\mathbf{x})\mathbf{E}(\mathbf{x}). \quad (2.5)$$

D denotes the diffusion constant, μ the mobility and \mathbf{E} the electric field. The diffusion constant and the mobility are linked over the Einstein relation:

$$D = \frac{k_B T}{q} \mu \quad (2.6)$$

where k_B is the Boltzmann constant, T the temperature and q the electron charge. The electric field itself is related to the carrier density through Poisson's equation:

$$\rho(\mathbf{x}) = \nabla\mathbf{D}(\mathbf{x}) = \varepsilon\varepsilon_0\nabla\mathbf{E}(\mathbf{x}) \quad (2.7)$$

Here, \mathbf{D} is the electric displacement, ε the dielectric constant and ε_0 the permittivity in vacuum. These equations 2.4, 2.5 and 2.7 will allow us to derive rate equations for the electron and hole density. The numerical implementation of the rate equation model and the comparison of the calculated with the experimental data will allow us to verify the applied theoretical model and will be important for the discussion of the data.

2.3 Experimental setup

One can envision various configurations combining femtosecond pump-probe techniques with NSOM. For example, the pump pulse, the incident probe pulse, or both pulses can propagate through the NSOM fiber while the transmitted or reflected probe pulse is detected in the far-field. Alternatively, the transmitted or reflected probe pulse can be picked up by the NSOM fiber while the excitation pulses propagate in the far-field. For all these configurations, the excitation and detection can either be at two different wavelengths (i.e. two-color) or they can be degenerate.

A few of these configurations have been realized by various groups. In the system described in this thesis, a global pump / local transmitted probe configuration was chosen, shown in Fig. 2.7. The sample is excited from the bottom side by a pump pulse that is focused to a $\sim 10 \mu\text{m}$ spot by a 40 X microscope objective. The pump-induced changes in transmission are detected by a near-field probe pulse that is sent through the NSOM fiber and transmitted

through the sample. The novel detection system described later can be used for both degenerate or two-color excitation. This novel combination allows for a high degree of measurement flexibility. All experiments are performed at room temperature.

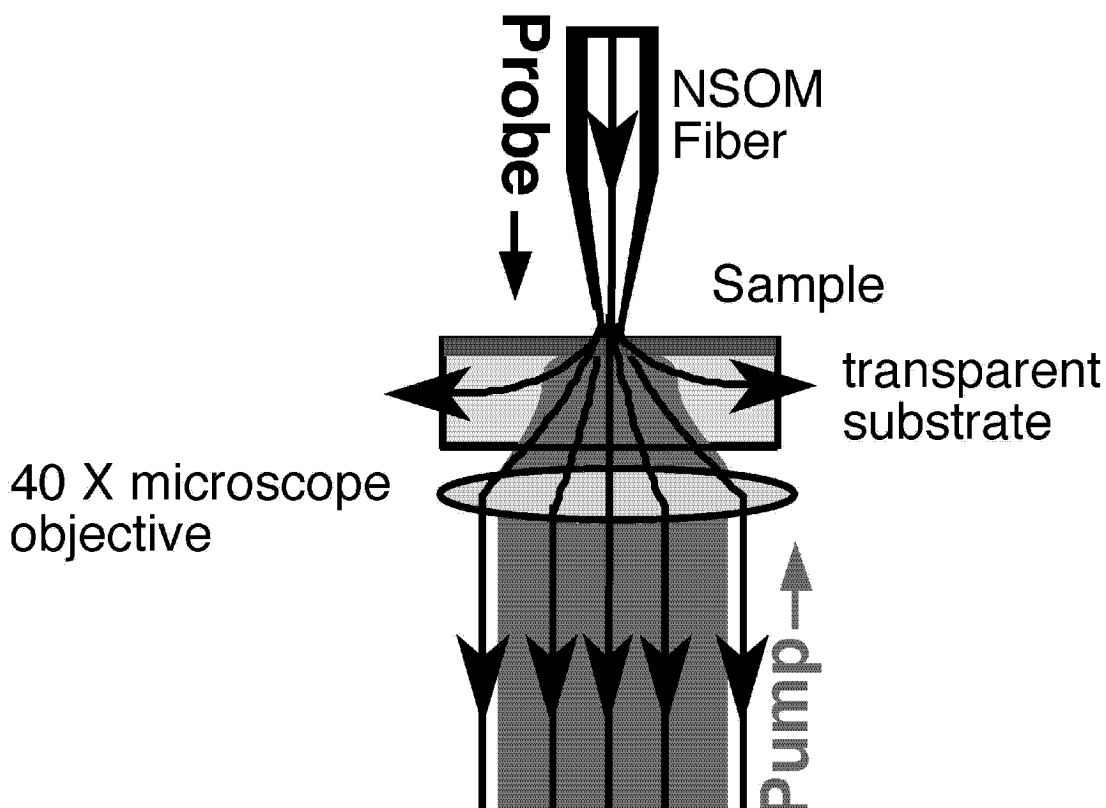


Fig. 2.7 The far-field pump / near-field transmitted probe configuration.

The choice between global or local pump excitation is largely determined by the requirements of the experiment. Global pump excitation was chosen mainly due to the greater excitation intensity that can be applied in the far-field, as opposed to the near-field. Specifically, pump excitation through the NSOM tip is limited in the maximum excitation intensity due to the very low power throughput of NSOM tips and the tip damage threshold of a few mW of input power to the fiber [52, 53]. In global pump excitation, the excitation intensity is only limited by the damage thresholds of the sample so potentially larger nonlinear responses can be measured. Additionally, the pump intensity and thereby the excited carrier density is more precisely determined in FF excitation than in NF excitation.

Since global pump excitation was chosen, the differential probe transmission signal had to be measured locally with the NSOM tip. The main consideration in the decision between measuring in illumination versus collection mode was signal to noise. The general experience in the NSOM experiment community is that there is considerably more signal to work with in illumination mode NSOM, as opposed to collection mode [61]. Therefore, the higher efficiency of illumination mode NSOM determined our preference for this configuration.

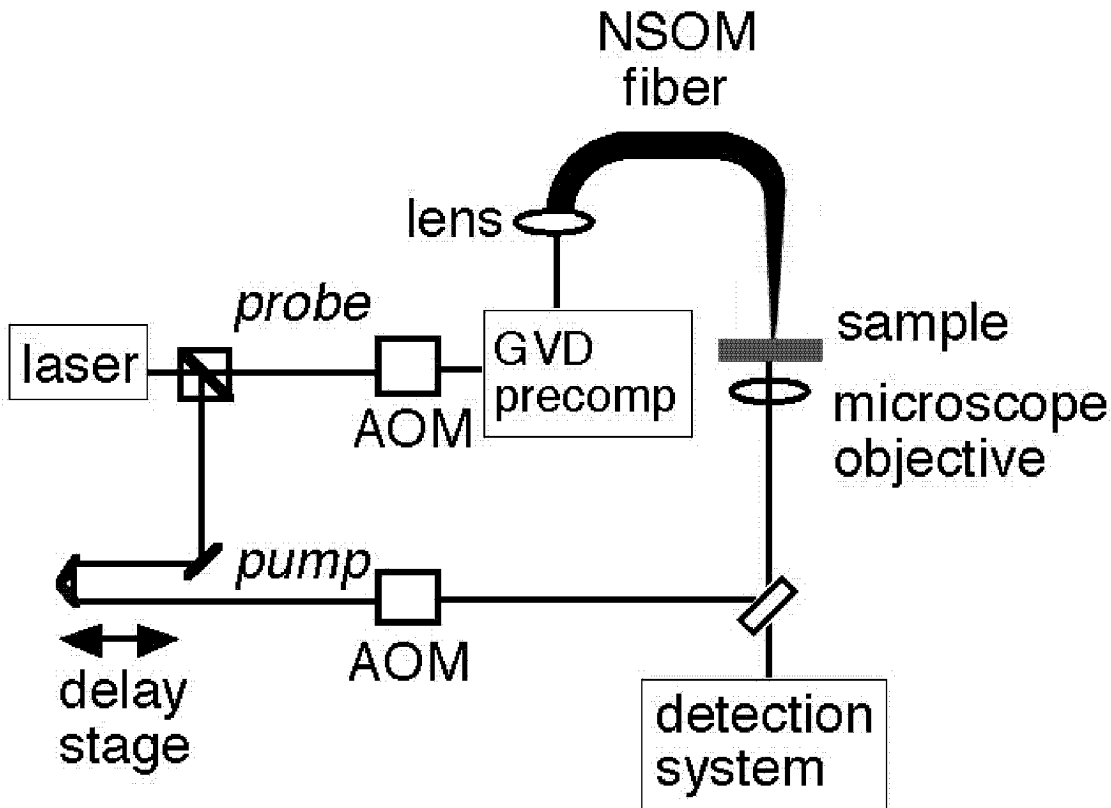


Fig. 2.8 Experimental pump-probe set-up. AOM: acousto-optic modulator, GVD: group velocity dispersion.

Details of the pump-probe NSOM set-up are shown in Fig. 2.8. A modelocked laser source (either a home-built Ti:Sapphire or a commercial Cr:LiSAF laser) generates a train of ~ 100 fs pulses tunable at wavelengths around 800 nm and a repetition rate of ~ 100 MHz. The pulse train is split into pump and probe pulses by a polarizing beamsplitter cube. The pump beam is sent through a motorized variable delay stage, which determines the time delay between the pump and probe pulses. It is then square-wave modulated at 1 MHz by an acousto-optic modulator (AOM) from IntraAction Corp (model AOM-40N) before being sent up through the NSOM objective and focused to a $\sim 10\mu\text{m}$ spot on the

sample. The probe pulse is first square-wave modulated at 1.05 MHz by an AOM and then sent through a group velocity dispersion (GVD) precompensation set-up. The resulting negatively chirped probe pulse is then coupled into a single mode NSOM fiber, emerging at the output NSOM tip aperture with pulsewidths typically below ~ 200 fs. The output from the NSOM tip aperture is transmitted through the thin sample in the near-field and collected in the far-field through the NSOM objective to the detection optics and an avalanche photodiode (APD). The differential probe transmission signal ΔT is measured at the 50 kHz difference frequency using a lock-in amplifier (Stanford Research Systems SR830). The linear transmission signal T is simultaneously measured at 1.05 MHz with a RF lock-in amplifier (Stanford Research Systems SR844) to calculate the normalized differential transmission signal $\Delta T/T$. The probe and backreflected pump light collected by the NSOM objective lens can alternatively be directed to a CCD imaging system to facilitate alignment for pump-probe spatial overlap.

2.3.1 Signal-to-noise considerations

Typical differential probe transmission signals lie in the pW range. This pW-range signal is accompanied by large background signals which include the transmitted probe power that is unaffected by the pump and the backreflected pump power, which can not be easily avoided with the NSOM geometry. These background signals dwarf the differential probe transmission signal. Therefore, modulation and lock-in detection is used to differentiate between the differential probe transmission and the unaffected probe and backreflected pump. Specifically, as mentioned in the previous section, the input pump and probe pulse trains are modulated at 1 MHz and 1.05 MHz respectively. The effect of pump excitation on probe transmission corresponds to a nonlinear response which mixes the pump and probe signals, introducing a differential probe transmission signal at the 50 kHz difference frequency, which can be measured with lock-in detection. The high frequencies of the pump and probe modulation reduce thermal effects of the tip-sample interaction [52] and, together with the high difference frequency, reduce the effect of laser noise.

Despite these measures, the unaffected probe and the back-reflected pump can still affect the measurement by increasing the measured shot and laser noise or even saturating the detector. Unfortunately, detection of the unaffected probe

signal cannot be avoided, since it cannot be purely optically separated from the desired differential probe signal. Fortunately, this unaffected probe signal is small enough that it does not introduce significant problems, only slightly increasing the noise floor above detector dark noise. However, the back-reflected pump signal is typically many orders of magnitude larger, so that measures need to be taken to reduce this signal as much as possible. In order to avoid the noise and saturation problems associated with detected pump signal, other groups have used two-color set-ups with spectral filtering or symmetric arrangements of pump and probe through equal-pulse correlation, sending both pump and probe through the fiber so that both the transmitted pump and unaffected transmitted probe background signals are small. In the experiment described in this work, two measures are taken to reduce the back-reflected pump while avoiding the wavelength limitations of the two-color requirement and the limitations on the measurement flexibility in the equal-pulse set-up. These are shown in Fig. 2.9. First, the pump and probe beams are orthogonally polarized so that a Glan-Thomson polarizer filters out the pump by a factor of typically more than 100, and even as high as 500, while passing most of the probe. Though the polarization of the probe light output from the NSOM tip is not perfectly linear, measurements reveal that the polarization stays quite constant over the pump-probe measurement period. Therefore, no artifacts are introduced into the pump-probe scan by the polarization sensitive detection.

A second method for reducing the back-reflected pump light involves a confocal arrangement consisting of a 50 μm pinhole that spatially filters out the light outside of a 1.25 μm diameter sample area, thereby reducing the back-reflected pump by as much as a factor of 100 (see Fig. 2.9).

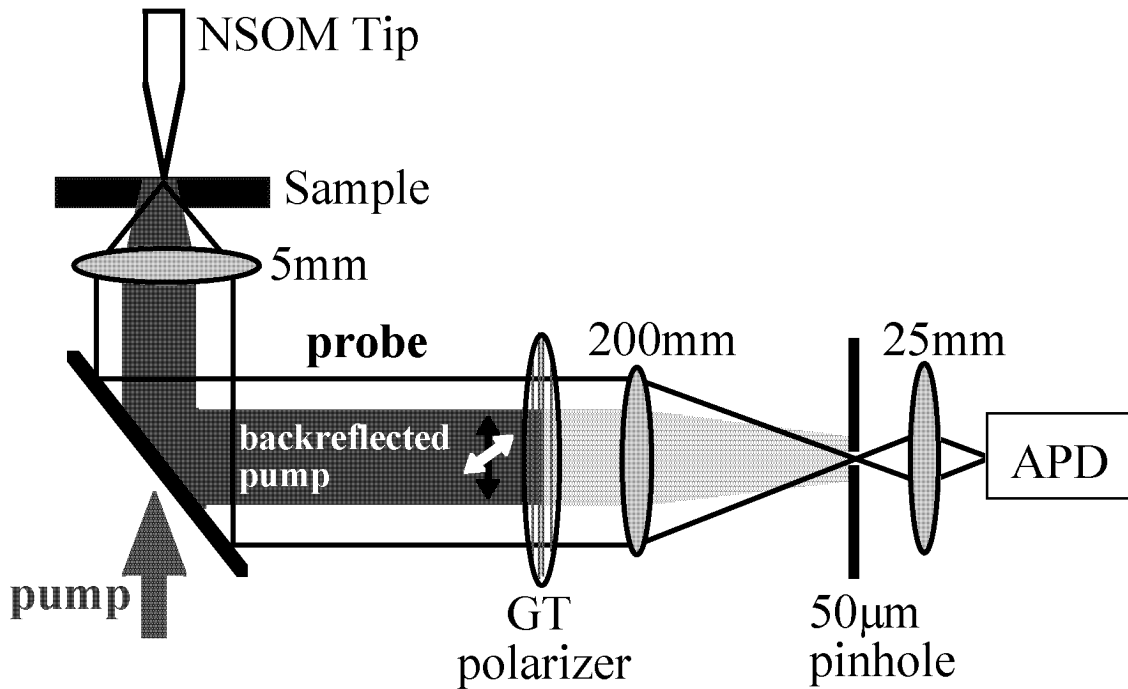


Fig. 2.9 Detection system, incorporating polarization discrimination and a confocal setup to reduce the back-reflected pump signal. GT: Glan Thomson, APD: avalanche photodiode.

These precautions significantly reduce the back-reflected pump light and therefore lower the shot noise level of the electrical signal obtained from the avalanche photodiode (APD). The APD module in our setup is a home-built low-noise module with an avalanche photodiode from Hamamatsu (S6045) and a low-noise operational amplifier from Analog Devices (AD744). Due to a thorough design the dark noise-equivalent power is below $10 \text{ fW}/\sqrt{\text{Hz}}$. This small dark noise level has actually always been below the shot noise level originating from background signal and has therefore not limited the detectable signal.

One artifact of the APD module detection is an electrical mixing of the pump and probe pulses at high gain operation of the avalanche module. This introduces a time-delay dependent background signal at the 50 kHz difference frequency at which the differential probe transmission signal is measured. For large back-reflected pump signals, this can be significant enough to warp the pump-probe trace. In all the measurements shown in this work, this mixing effect was sufficiently suppressed by the reduction of the background signals. It

is noteworthy that with a commercial APD module we used before, this mixing problem was even much more pronounced.

Including all these considerations, our setup allows us to measure normalized differential probe transmission signals, $\Delta T/T$, below 1×10^{-4} .

2.3.2 Maintaining high time resolution in a NSOM

Besides signal to noise considerations, time resolution and the limits imposed on it by group velocity dispersion (GVD) is also an important issue. Of highest concern is the GVD of the NSOM fiber, a meter of which can stretch a 100 fs pulse at 800 nm to a chirped 1 ps pulse. Therefore, a GVD precompensation set-up was introduced before the fiber coupler in order to add a negative GVD to the pulse, which balances the positive GVD of the ~50 cm length of fiber. The GVD precompensator consisted of a standard two-prism set-up [67] shown in Fig. 2.10 [67], in which different spectral components of the pulse travel different distances, introducing a net negative GVD which depends on prism spacing and insertion.

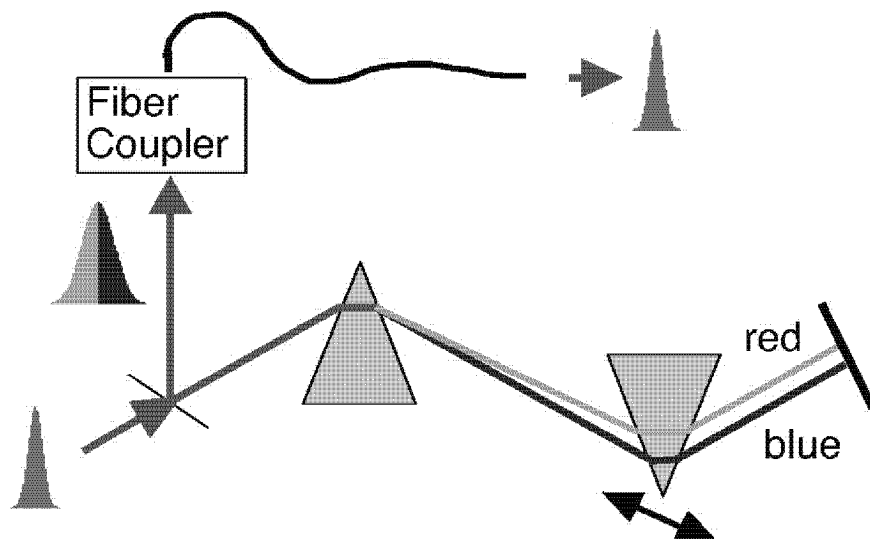


Fig. 2.10 Standard prism pair setup to precompensate the group velocity dispersion in the NSOM optical fiber.

Fig. 2.11 shows the pulsewidth at the output of a 46 cm open-ended fiber after precompensation, deconvoluted from measured autocorrelation traces, as a function of prism separation, for a 90 fs input pulse. As can be seen, the pulsewidth can be largely recovered with proper GVD optimization.

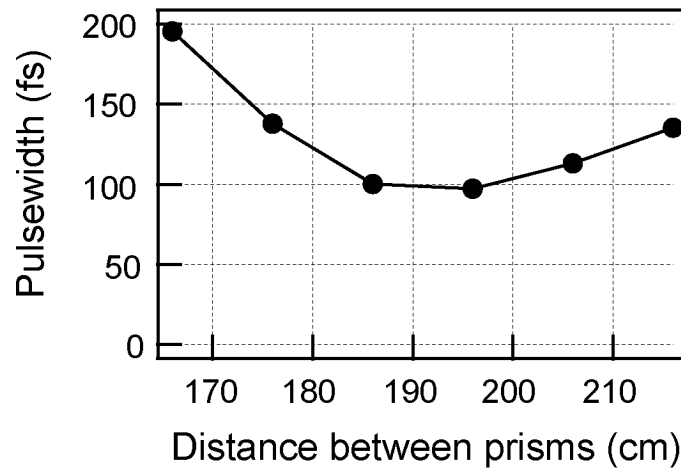


Fig. 2.11 Measured pulse-width at the output of a 46 cm fiber vs spacing between the prisms of the two-prism GVD precompensation setup, for a ~ 90 fs input pulse-width.

The precompensation for 100 fs pulses should not be affected by the NSOM tip itself, which does not show much effect on GVD [16]. Given this precompensation, we have measured time-responses as fast as ~ 250 fs. This is shown in the pump-probe trace of Fig. 2.12, which was taken on the FIB implanted quantum well sample 100/2000, described later in this chapter.

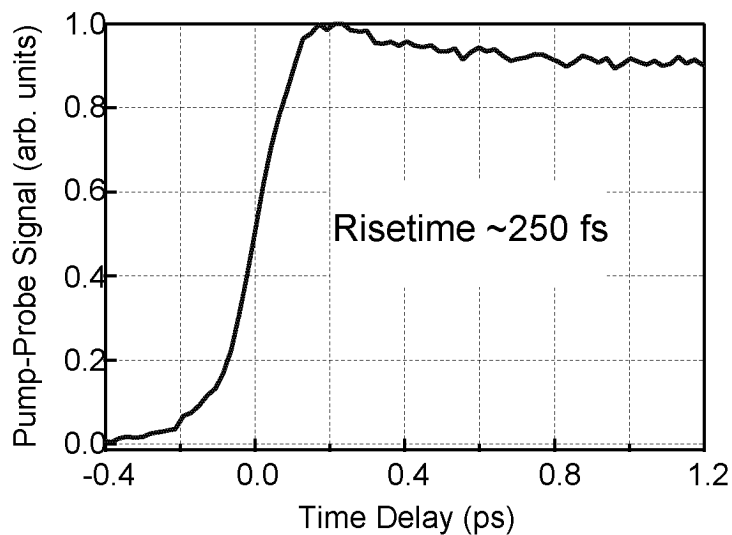


Fig. 2.12 Local pump-probe measurements of the FIB implanted quantum well sample 100/2000, showing a temporal resolution of ~ 250 fs.

The ~ 250 fs 10-90% risetime of this signal roughly represents the convolution of the sech^2 -shaped pump and probe pulses. This time resolution is partially

limited by the ~ 150 fs pulsewidth of the pump, which was not precompensated for the ~ 11 cm of glass of the AOM and other optics. It is expected that the time resolution can be further improved by precompensating the pump pulse and also by decreasing the laser output pulsewidth. For the experiments discussed in this thesis, no improvement of the temporal resolution has been necessary.

One issue of consideration in sending ultrafast pulses through NSOM fibers is the possibility that nonlinear effects in the fiber [68], such as self-phase modulation and stimulated Raman scattering, can warp the spectrum of the measured output pulse. To explore this effect, spectral measurements were made on the outputs of open-ended NSOM fibers, where the ~ 100 fs input pulses were first precompensated for the NSOM fiber length with the prism set-up described in the previous paragraph. These measurements are shown in Fig. 2.13. One can see that, for 25 mW output power, the output pulse spectrum is significantly warped with respect to the input pulse spectrum – revealing significant nonlinear effects. However, for output powers below ~ 4 mW, no significant nonlinear effects were observed. Though these results were measured with open ended fibers, it has been shown that the subwavelength aperture does not have an effect on the spectrum [69]. Only for 10 fs pulses it has been shown theoretically that a metal coated aperture probe can strongly modify the temporal and spectral pulse profile [70]. Therefore, for our 100 fs pulses and since optical powers within NSOM fibers cannot be much higher than 4 mW due to tip damage, the nonlinear effects are not significant.

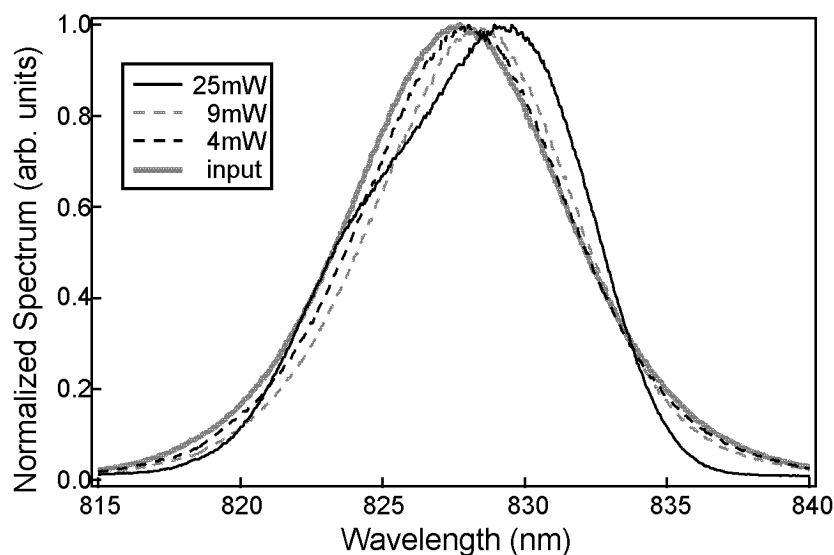


Fig. 2.13 Spectra of precompensated fiber output pulses for various fiber output powers and fiber input spectrum as a reference.

2.4 Topographical artifacts

A major issue of concern in most NSOM measurements are topographical artifacts [71] in which the topography of the measured surface can alter the optical image, independent of the variation in optical properties. This is of lesser concern in this instrument since the main physics which is explored involves the temporal dependence of the carrier dynamics. This means that we are mainly interested in the temporal shape of the pump-probe scan and how this temporal dependence varies across the sample, issues in which the topographical artifacts are less significant.

As the FIB samples studied in chapter 3 and the W-disk sample investigated in chapter 4 have flat surfaces, topographical artifacts do not have to be discussed. However, for samples with larger topographical variations, like the V-groove quantum wires in chapter 5, topographical artifacts must be taken into account when interpreting spatial variations in pump-probe amplitudes and in determining the spatial resolution.

2.5 Semiconductor sample preparation for NF measurements

Suitable samples for near-field measurements have to fulfill one main consideration, namely that the active region has to be close to the surface. This entails that the active region and top protection or barrier layers have to be very thin. Active regions in quantum structures like quantum wells, wires or dots are inherently thin, in the order of some nanometers. Bulk semiconductor samples should be designed with a thickness, that doesn't exceed 100 nm to maintain reasonable spatial resolution. With respect to energy barriers and protection layers, they should be as thin as possible without losing on their functionality, resulting in a thickness of a few tens of nanometer.

The used global pump / local transmitted probe configuration requires that the semiconductor samples are suitable for transmission measurements. Typically, the samples are grown on a opaque 0.4 mm thick GaAs substrate, which has to be removed. This is accomplished by growing on the GaAs substrate an etch stop layer sequence followed by the nanostructure of interest and a 400-500 nm thick transparent layer as a mechanical support, as schematically depicted in Fig. 2.14.

500 nm mechanical support
semiconductor nanostructure
40 nm $\text{Al}_x\text{Ga}_{1-x}\text{As}$
100 nm GaAs
300 nm $\text{Al}_x\text{Ga}_{1-x}\text{As}$
GaAs substrate

Fig. 2.14 Typical semiconductor nanostructure sample for transmission NSOM measurements, including GaAs/ $\text{Al}_x\text{Ga}_{1-x}\text{As}$ etch stop layers.

First, the sample is glued onto a 1 mm thick BK7 (RS10X1 from WZW Optic AG) glass substrate with the epitaxial layers facing downwards using a UV curing optical adhesive (NOA61 from Thorlabs). The GaAs substrate is thinned down to $\sim 100 \mu\text{m}$ using a bromine methanol solution. Subsequently, the GaAs/ $\text{Al}_x\text{Ga}_{1-x}\text{As}$ etch stop layers are removed by chemical wet etching with peroxide/ammonium-hydroxide ($\text{H}_2\text{O}_2/\text{NH}_4\text{OH}$) solution for GaAs [72] and fuming hydrochloric acid (HCl) solution for AlAs. The $\text{H}_2\text{O}_2/\text{NH}_4\text{OH}$ solution has its best selectivity at pH 7.05. In a more concentrated solution it etches faster [72-74]. The remaining structure consists of the mechanical support that prevents the sample from cracking due to stress implied by the glue, and of the nanostructure of interest.

2.6 Proof of principle of the ultrafast NSOM

In order to prove the imaging capability of the femtosecond NSOM, experiments on semiconductor nanostructures are performed. The requested structure must have a reasonable predictable lateral variation in carrier dynamics and preferentially a flat topographical profile.

2.6.1 Focused-ion beam implanted quantum well

The desired semiconductor nanostructures have been obtained by nanometer-scale lateral patterning of an undoped 80 Å GaAs/Al_{0.3}Ga_{0.7}As single quantum well with focused ion beam (FIB) implantation of 50 keV Ga ions, as shown in Fig. 2.15.

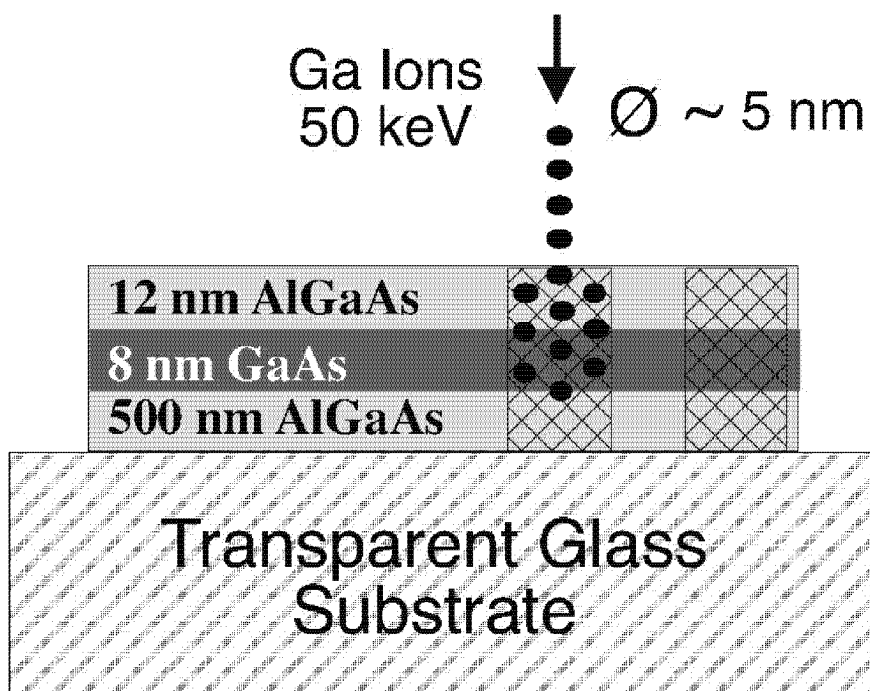


Fig. 2.15 Side view of the structure and the fabrication process of the FIB implanted quantum well.

The implantation energy was chosen to create damage in the GaAs quantum well, according to TRIM simulations [75]. The local ion implantation results in defect formation, which gives rise to carrier trapping with picosecond or sub-ps time constants [76, 77]. Sample 100/2000 is patterned with 100 nm implanted

stripes and 2000 nm spaces at a dose $8 \times 10^{11} \text{ cm}^{-2}$, sample 200/400 with 200 nm implanted stripes and 400 nm spaces at a dose $3 \times 10^{12} \text{ cm}^{-2}$ (see Fig. 2.16).

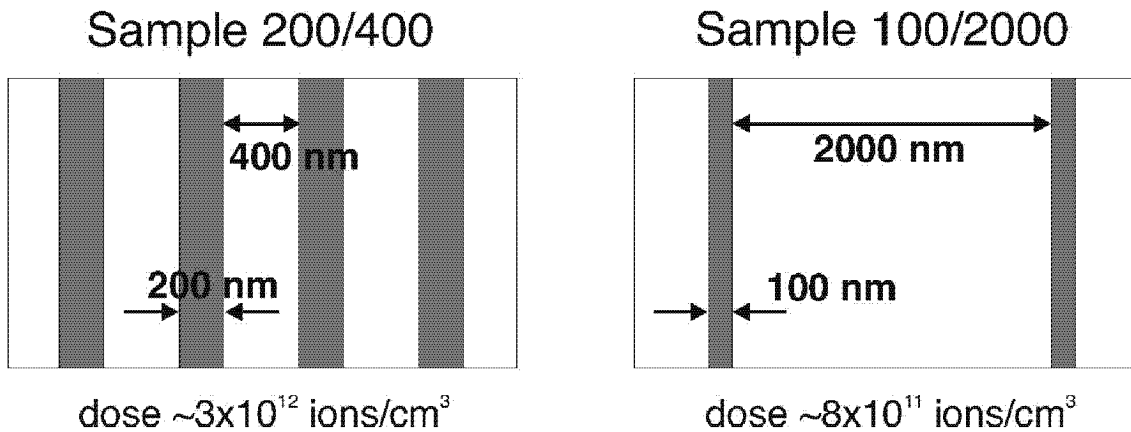


Fig. 2.16 Pattern of the two FIB samples 200/400 and 100/2000. The gray regions indicate the implanted stripes.

The FIB implantation creates a spatial defect profile with well-defined edges since TRIM simulations [75] show that the defects spread only 20 nm beyond the nominal width of the implanted stripes. The preparation of the samples for transmission experiments follows the description of section 2.5. The remaining quantum well has a 12 nm AlGaAs top barrier, which allows one to bring the NSOM tip close to the optically active layer, ensuring high spatial resolution in near-field experiments. In all experiments, the laser was tuned to the lowest heavy hole exciton resonance of the quantum well at 1.475 eV (840 nm). The pump fluence was $4 \mu\text{J/cm}^2$, corresponding to a carrier density of about 10^{11} cm^{-2} . It is noteworthy, that the focused-ion beam implanted quantum well sample has not only been used as a test sample to show the capabilities of the ultrafast NSOM but also to study carrier diffusion dynamics, which will be described later in chapter 3.

2.6.2 First spatially and temporally resolved measurements

Fig. 2.17 shows a two-dimensional image of the amplitude of the pump-probe signal at zero time delay, measured on sample 200/400. One can clearly distinguish variations in the pump-probe amplitude image which follow the 600 nm period of the FIB implantation pattern. The dark regions correspond to

smaller signals. Fast carrier trapping in the implanted stripes is at the origin of the pump-probe pattern. Carrier trapping reduces the carrier density in the implanted stripes already at zero time delay when the pump and the probe pulse temporally overlap, resulting in a smaller pump-probe amplitude. It should be noted that no contrast is seen in the simultaneously measured topography image of Fig. 2(b), excluding the possibility that the pattern in the pump-probe image is a topographical artifact [71]. Thus, the femtosecond NSOM can provide images of the optical nonlinearity at fixed time delays.

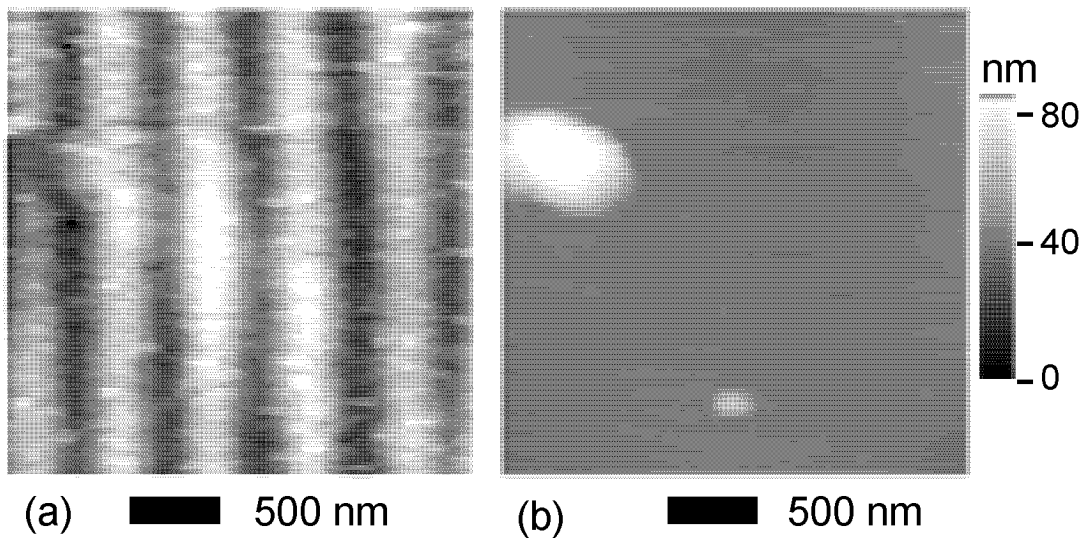


Fig. 2.17 (a) A two-dimensional image of the pump-probe amplitude at zero time delay. (b) The simultaneously measured topography of the GaAs/AlGaAs quantum well with 200 nm FIB implanted stripes and 400 nm spaces.

Fig. 2.18 shows a 2-D scan of sample 100/2000, in which the NSOM tip was scanned across the surface of the sample while various optical signals were measured – either amplitude of the pump-probe signal (ΔT), linear probe transmission (T), or probe light blocked (B) – as shown. Though the 2 μm periodicity of the implantation profile is clearly visible in the pump-probe amplitude variation, no such correlation is seen in the linear probe transmission profile. This shows that it is the nonlinear response of the sample which is measured, not the linear response.

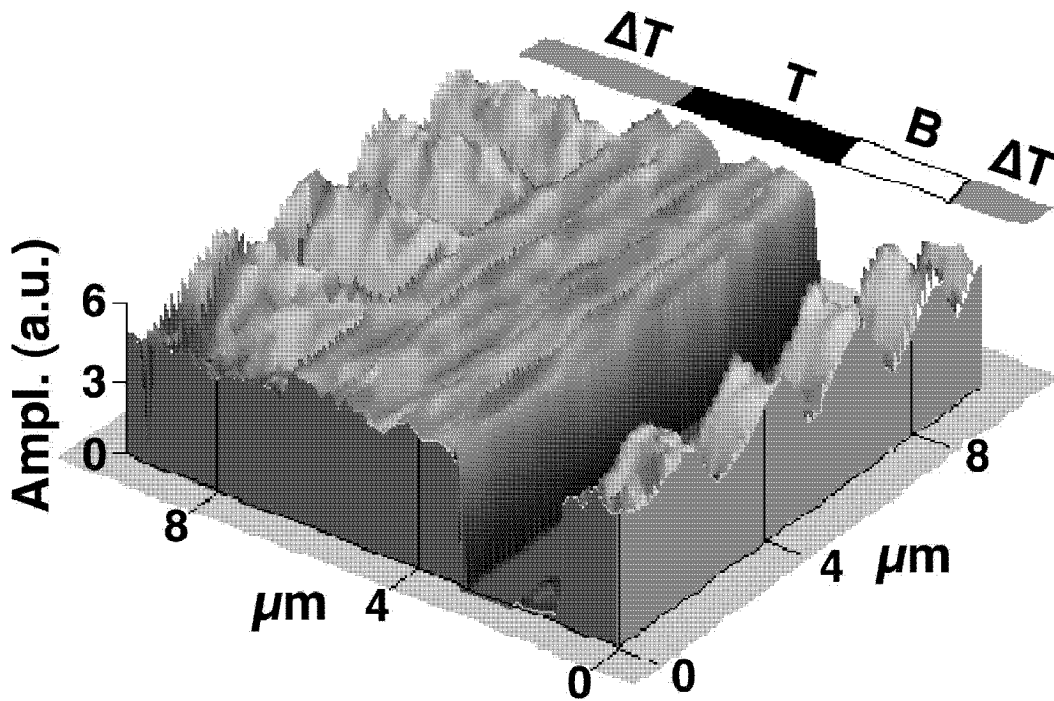


Fig. 2.18 Two-dimensional scan of sample 100/2000 where the measured optical signal is changed during the scan as shown. ΔT : differential probe transmission signal at 40 ps time delay, T : linear probe transmission, B : detector blocked.

For the determination of the spatial resolution of our home-built femtosecond NSOM, a series of pump-probe time-domain measurements are taken at various positions across the FIB pattern of Fig. 2.17. Fig. 2.19(a) shows normalized plots of a few of these scans, while Fig. 2.19(b) shows the amplitude of these scans from a single-exponential fit versus distance across the FIB pattern. The 10-90% lateral rise in the amplitude plot reveals a lateral resolution as high as ~ 150 nm. Indeed, this is a conservative estimate of lateral resolution since it assumes a step-like variation in the implantation profile, whereas TRIM [75] simulations suggested that the lateral damage was spread by ~ 20 nm.

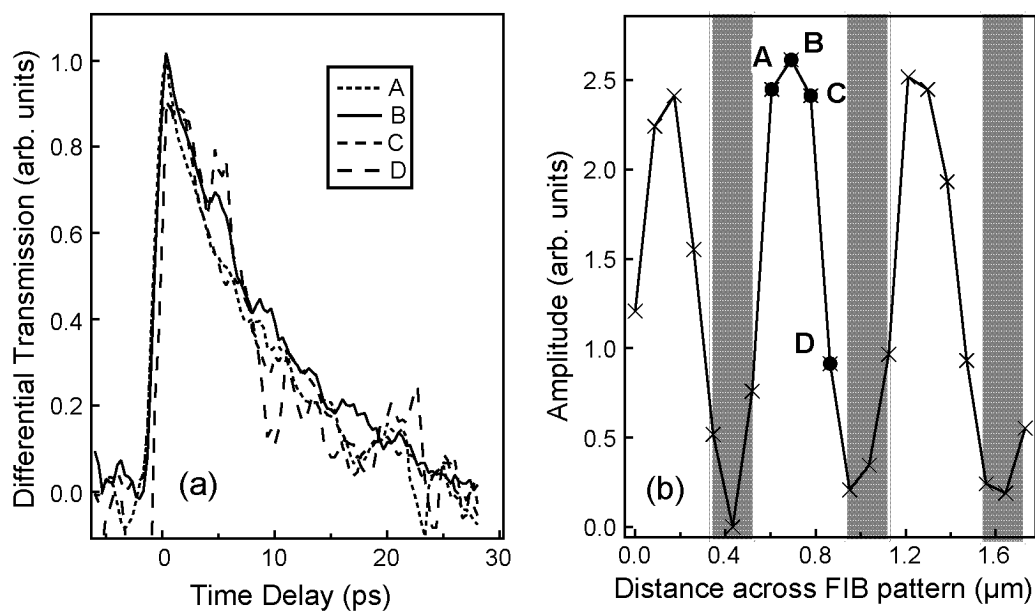


Fig. 2.19 (a) Normalized pump-probe scans taken at the positions indicated in (b). (b) Pump-probe amplitude at zero time delay vs distance across the FIB sample 200/400. The gray region correspond to the implanted stripe.

Summarizing this chapter, the described home-built femtosecond NSOM allows differential transmission measurements with 150 nm spatial and 250 fs temporal resolution and a high sensitivity of $\Delta T/T < 10^{-4}$.

3 Different diffusive transport regimes in focused ion beam implanted semiconductor quantum wells

In this chapter, we experimentally demonstrate that diffusive carrier transport in semiconductor nanostructures results in complex spatiotemporal carrier dynamics on the picosecond time and the nanometer length scale. We have studied nanostructured samples in which carrier drift can be neglected, facilitating the observation of the detailed features of carrier diffusion. Different diffusion regimes are identified. In an initial regime, we directly observe *non-sinusoidal* carrier density profiles in which the temporal diffusion decay depends on the spatial position. On longer time scales, a *quasi-sinusoidal* spatial carrier profile forms, in which the temporal diffusion decay is only weakly dependent on position, characteristic for the long-time diffusion regime. The femtosecond NSOM allows us to directly measure the shape of nanometer-scale spatial carrier profiles at different times.

The carrier diffusion studies have been performed on the focused ion beam (FIB) implanted quantum well samples 200/400 and 100/2000 described in the previous chapter, section 2.6.1.

3.1 Experimental results in the initial diffusion regime

All experiments in this chapter have been carried out at room temperature with 15 meV wide pump and probe spectra centered at the lowest heavy hole exciton resonance of the quantum well at 1.475 eV. The pump fluence is 4 $\mu\text{J}/\text{cm}^2$, corresponding to a carrier density of about 10^{11} cm^{-2} .

3.1.1 Spatially dependent time scans

Fig. 3.1 shows normalized pump-probe traces at different positions across the FIB pattern of sample 100/2000. The overall shape and the initial decay strongly depend on the position. To quantify this position dependence, we have fitted the experimental traces to double-exponential functions

$A\exp(-\Delta t/\tau_1) + B\exp(-\Delta t/\tau_2)$ where Δt is the time delay between pump and probe pulse. Here, τ_1 is the faster time constant and describes the initial decay while τ_2 is the slower time constant, which describes the decay at longer times. A detailed discussion of the physical meaning of τ_1 and τ_2 will be presented later. From our data, we find that τ_2 is 200-300 ps, independent of the spatial position.

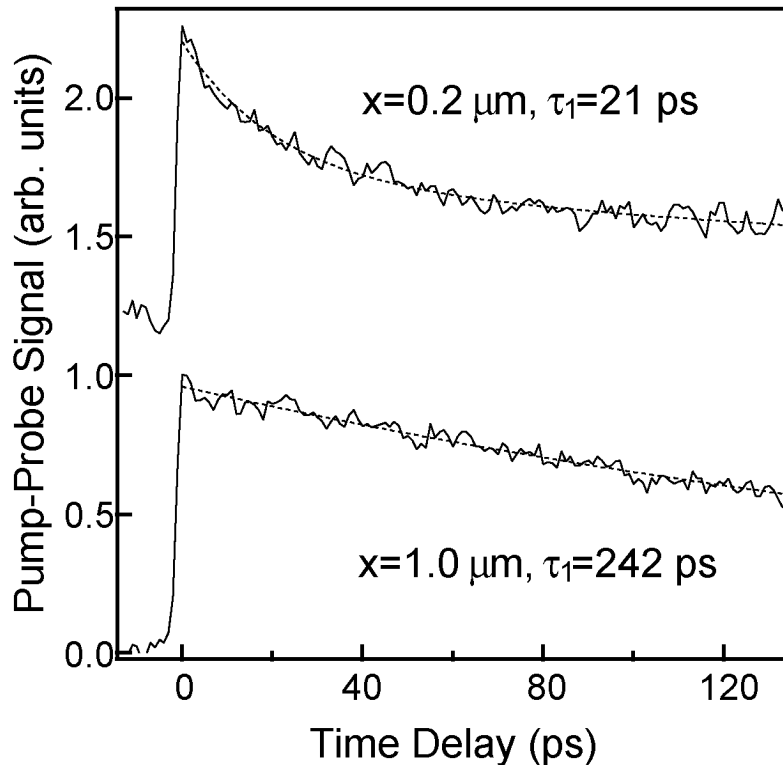


Fig. 3.1 Sample 100/2000 (100 nm implanted stripes, 2000 nm spaces): Normalized pump-probe traces at different distances x away from the stripes, experimental traces (solid), double exponential fits (dotted) from which the initial decay time τ_1 is obtained.

The faster initial decay time τ_1 and the pump-probe amplitude at $\Delta t = 0$ are plotted versus position in Fig. 3.2. The amplitude is reduced in the implanted stripe, as expected [77] [78]. Midway between the implanted stripes, the decay time τ_1 is roughly equal to the 250 ps. Surprisingly, the decay times over an 800 nm wide range around the 100 nm implanted stripe are much shorter at about 10-40 ps.

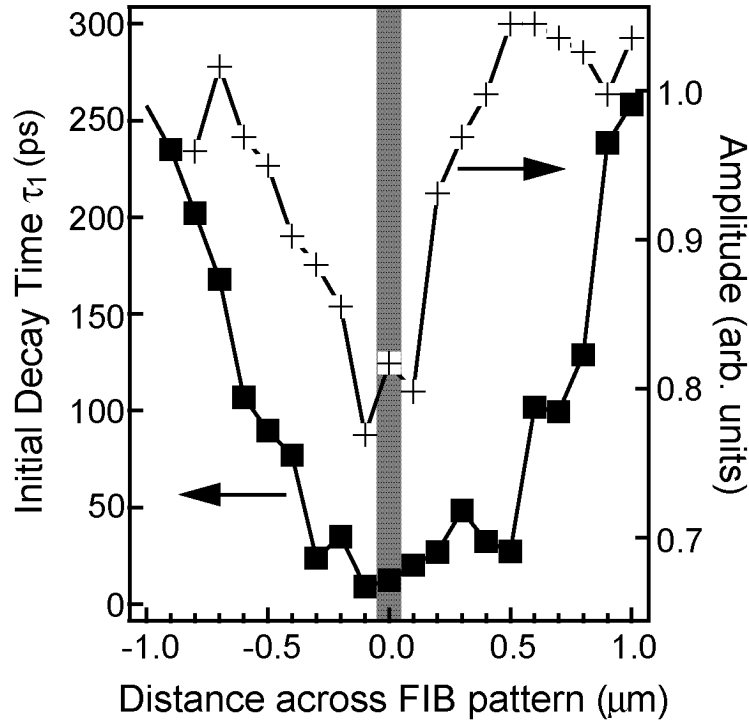


Fig. 3.2 Sample 100/2000: Initial decay time τ_1 (squares) and pump-probe amplitude at zero time delay (crosses) vs. position. The gray bar marks the implanted stripe.

Note that the pump-probe traces decay almost exponentially with a time constant of roughly 250 ps far away from the FIB patterned area. This decay time is independent of position and will be referred to as recombination time in the following². The short decay times around the implanted stripe cannot be due to recombination. Furthermore, they cannot be caused by spatial averaging with the fast trapping times in the implanted stripes since the rise in the amplitude signal shows that spatial averaging effects happen on a much shorter spatial scale. Lastly, carrier trapping due to a wider damage profile cannot be the reason for these short decay times either since the large amplitude, i.e. large nonlinearity, in much of this region shows that the implantation-induced defect

² The recombination times in samples 100/2000 and 200/400 are not due to intrinsic radiative recombination but result from non-radiative decay due to a small laterally uniform background implantation dose applied in the FIB patterning process. The background implantation dose varies between FIB implantation runs. This results in different recombination times in sample 100/2000 and 100/2000.

distribution is not much broader than the nominal stripe width of 100 nm, as expected from the TRIM simulations [75].

We conclude that the short decay times τ_1 of 10-40 ps result from carrier transport. In general, both carrier diffusion and drift can contribute to the transport. Carrier drift requires potential gradients. We note that the sample does not contain potential gradients in the plane of the quantum well before implantation. Moreover, the implantation is not expected to result in large potential gradients. This is because ion implantation into GaAs generates As antisite [79]. These defect states are located close to the center of the bandgap [80] and pin the Fermi level at mid-gap [81]. Since the Fermi level in the unimplanted regions is also at mid-gap in the undoped quantum well, we do not expect the formation of large potential gradients. Moreover, we do not expect the formation of large potential gradients due to compositional intermixing, which gives large energy shifts only at ion doses higher than the ones used in our samples [82]. Consequently, we conclude that carrier drift can be neglected and that carrier transport is mainly due to diffusion of carriers towards the implanted stripe.

3.1.2 Numerical model of the carrier diffusion dynamics

In our FIB samples, diffusion is driven by the carrier density gradient that is caused by the fast trapping of carriers in the stripe. This conclusion is confirmed by quantitative modeling which includes diffusion but neglects drift. Since the optical excitation of excitons is followed by ionization after about 300 fs at room temperature [83], the dynamics of the density n of band electron-hole pairs is modeled. We have solved the one-dimensional continuity equation for the electron-hole pair density n , coupled to the differential equation for the density n_t of occupied traps

$$\frac{\partial n(x,t)}{\partial t} = D_a \frac{\partial^2 n}{\partial x^2} - \frac{n}{\tau_{\text{rec}}} - \frac{n}{\tau_t(x)} \left(1 - \frac{n_t}{N_0} \right) + G(t) \quad (3.1)$$

$$\frac{\partial n_t(x,t)}{\partial t} = \frac{n}{\tau_t(x)} \left(1 - \frac{n_t}{N_0} \right) \quad (3.2)$$

Here, D_a is the ambipolar diffusion constant [84] [85], τ_{rec} the recombination time, τ_t the trapping time, and N_0 the total density of traps in the implanted stripes. The spatially uniform carrier excitation is described by the x independent generation term $G(t)$, for which we assume a sech^2 pulse with a full width at half maximum of 200 fs. The trapping rate $1/\tau_t$ decreases from a constant value in the implanted stripes to zero outside the stripes. This decrease occurs over a 20 nm wide transition region, determined from the TRIM simulations. Trap filling and the corresponding decrease of the trapping rate with time are accounted for in the third term on the RHS of eq. 3.1 in conjunction with eq. 3.2. The degree of trap filling is adjusted by the ratio $N_0 / \int G(t)dt$ in the implanted stripes.

The initial exciton ionization [83] as well as the thermalization of carriers with the lattice are not included in the model. At room temperature, the latter occurs in about a picosecond if carriers are injected at the band edge of GaAs/AlGaAs quantum wells [86] [87]. Therefore, equations 3.1 and 3.2 are used for time delays of 2 ps and longer. Moreover, for these time delays, the ambipolar diffusion constant D_a for room temperature can be used, neglecting any temperature dependence of diffusion [85].

In order to compare the calculated electron-hole pair density n to the measured pump-probe traces, we assume that the pump-probe signal is proportional to n [2]. In such comparisons, the calculated electron-hole pair density n is convoluted with a Gaussian function, which accounts for the spatial resolution of ~ 300 nm in these experiments. Fig. 3.3 shows measured and calculated pump-probe traces at different positions across the FIB pattern. For all positions, the calculation was performed with $D_a = 10 \text{ cm}^2/\text{s}$, $\tau_{\text{rec}} = 250 \text{ ps}$, $\tau_t = 3 \text{ ps}$, and $N_0 / \int G(t)dt = 4$ to account for trap filling. The value for D_a is reasonable in view of earlier work on GaAs/AlGaAs heterostructures and quantum wells [84] [85].

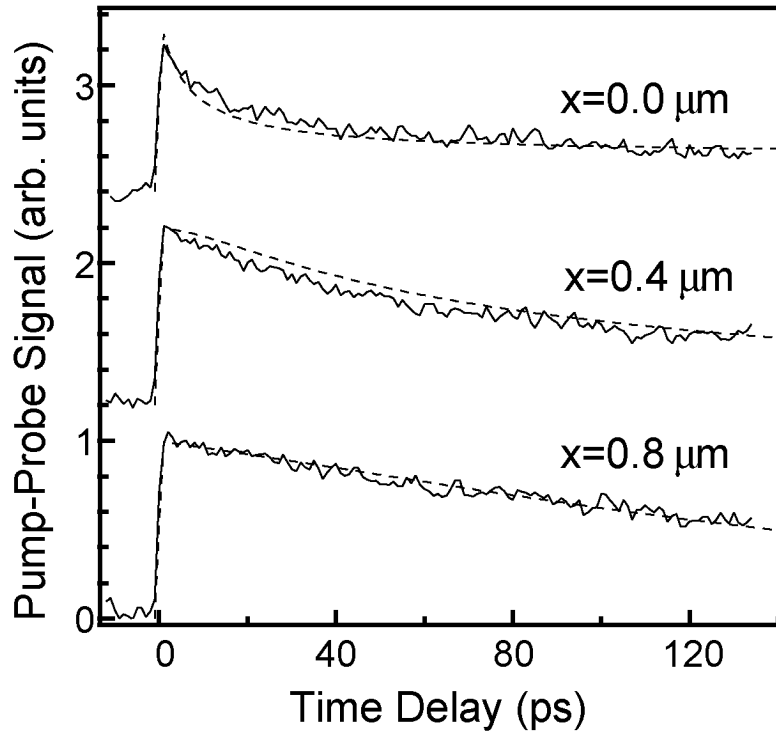


Fig. 3.3 Sample 100/2000: Measured (solid) and calculated (dashed) pump-probe traces at different positions, see text for the details of the calculation.

The good agreement between the experimental and the calculated pump-probe traces proves that diffusion substantially affects the dynamics in sample 100/2000 and strongly supports the argument that carrier drift can be neglected. Fig. 3.4 shows the faster time constants τ_1 , from double exponential fits to the measured and calculated pump-probe traces, versus position. Again, good agreement is obtained.

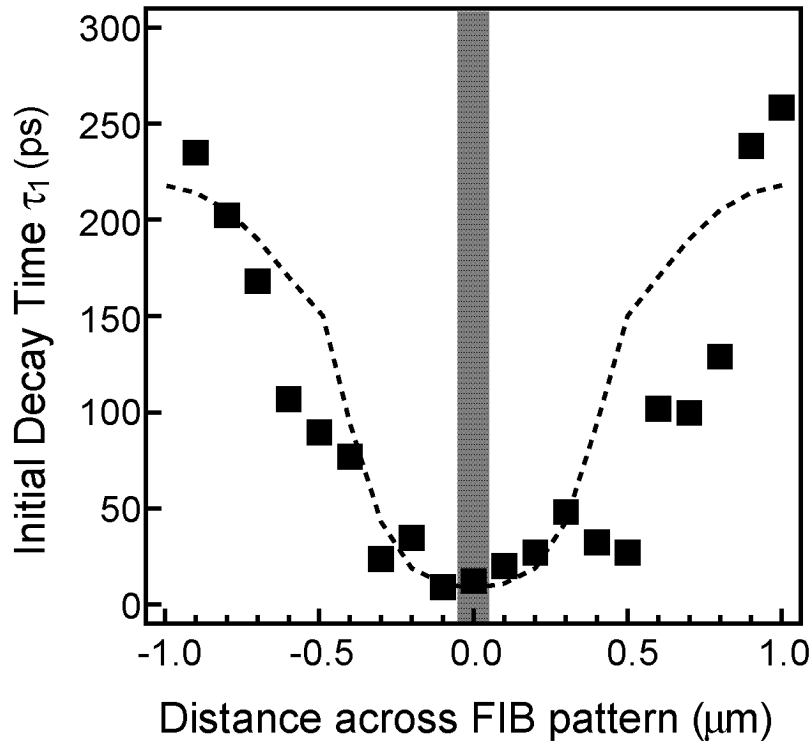


Fig. 3.4 Sample 100/2000: Initial decay times from double exponential fits to measured (squares) and calculated (dashed line) pump-probe traces vs. position.

3.1.3 Time dependent line scans

More details of the diffusion dynamics can be inferred from direct measurements of the pump-probe signal versus distance across the FIB pattern for fixed time delays Δt . This data is shown in Fig. 3.5. At an early time delay, $\Delta t=4$ ps, we observe a square-like pump-probe distance dependence, corresponding to a square-like carrier density profile. At a later time delay, $\Delta t=80$ ps, a smoother, quasi-sinusoidal profile is observed. These measurements show a good fit to the calculated profiles, which use the parameters obtained from the modeling in Fig. 3.3. The calculated carrier profile at $\Delta t=400$ ps is also shown³, revealing a profile which is almost flat.

³ For very long time delays, the measured pump-probe signal is so small that noise prevents detailed analysis. Therefore, only the calculated trace is shown in Fig. 3.5

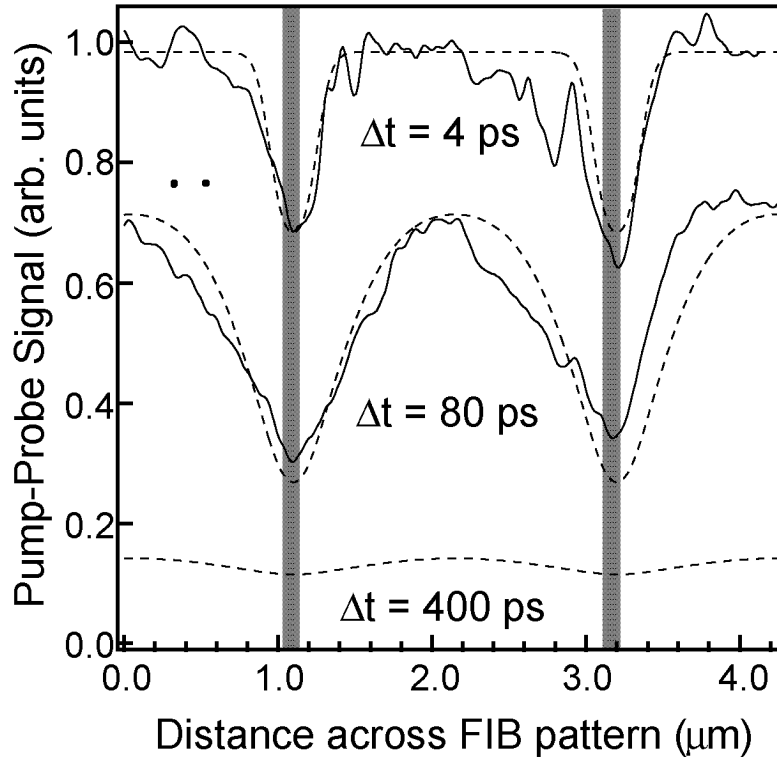


Fig. 3.5 Sample 100/2000: Measured (solid) and calculated (dashed) pump-probe signal vs. position for different time delays. Averaging over a 300 nm tip aperture was assumed in the calculation.

We conclude that the initial square-like profile at $\Delta t = 4$ ps is a result of the fast carrier trapping in the well-defined FIB implanted stripes. Enhanced diffusion at the edges of the square-like carrier profile then smoothes out the sharp edges, leading to the quasi-sinusoidal profile at $\Delta t = 80$ ps. At $\Delta t = 400$ ps, the flat carrier profile shows that diffusion has evened out the carrier density gradients. The smoothing of the initial square-like carrier profile in Fig. 3.5 results in the spatially dependent decay time τ_1 shown in Fig. 3.4. Fast decay times are observed close to the edges due to strong diffusion. In contrast, midway between the implanted stripes, diffusion is slow and the decay time τ_1 is much longer.

These effects can also be understood in the spatial frequency domain. We recall that, in a sinusoidal carrier distribution with period L , the carrier density exponentially decays due to diffusion with a time constant $\tau_D = L^2 / (4\pi^2 D_a)$ [88]. The linearity of the continuity equation implies that the dynamics of a *non-sinusoidal* periodic profile is simply the sum of the dynamics of its harmonic

components. These arguments show that the higher spatial harmonics of the initial square-like carrier profile decay much faster than the fundamental period due to their smaller L . The fast decay of higher spatial harmonics corresponds to the smoothing of the edges of the carrier profile in real space. Since the higher spatial harmonics decay much faster than the fundamental period, a quasi-sinusoidal profile is expected at long times, as observed in Fig. 3.5. With respect to the position dependence of the diffusion decay time $\tau_D = L^2 / (4\pi^2 D_a)$, we note that this decay time does not depend on position in sinusoidal carrier distributions [88]. Summarizing this discussion, we can distinguish two different diffusion regimes: (i) An initial diffusion regime, which is characterized by a square-like carrier profile containing higher spatial harmonics, and by position dependent temporal diffusion decay, and (ii) a long-time diffusion regime, in which the carrier profile is quasi-sinusoidal with only weakly position dependent temporal diffusion decay.

We now comment on the physical meaning of the time constants τ_1 and τ_2 of the double-exponential fit. The time constant τ_1 describes the initial diffusion regime. Close to the edges of the implanted stripes, τ_1 is much faster than the recombination time due to the fast diffusion corresponding to the decay of the higher spatial harmonics in the initial diffusion regime. Midway between the stripes, the diffusion current is negligible in the initial diffusion regime since the carrier profile is almost flat with negligible gradient. Therefore, τ_1 reflects the recombination time midway between the implanted stripes in sample 100/2000. In fact, the time constant $\tau_1=250$ ps determined experimentally midway between the stripes is identical to the recombination time determined far away from the FIB patterned area.

3.2 Experimental results in the long-time diffusion regime

In the long-time diffusion regime, diffusion with $D_a=10$ cm²/s in a sinusoidal profile with period $L=2.1$ μm leads to a decay of the carrier density with the time constant $\tau_D=110$ ps in sample 100/2000. This number is relatively close to the recombination time $\tau_{\text{rec}}=250$ ps. Therefore, both recombination and diffusion contribute to the decay of the pump-probe traces from sample 100/2000 at long times. This long-time decay is described by the slow time constant τ_2 . We have found that τ_2 is 200-300 ps from fits to both experimental and calculated pump-

probe traces, in agreement with the combined recombination and trapping dynamics. This discussion shows, that sample 100/2000 is not appropriate for the experimental observation of the long-time diffusion regime unperturbed by recombination.

The long-time diffusion regime is experimentally more accessible in sample 200/400 in which the overall diffusion is much faster due to the smaller distances. Fig. 3.6 shows a measured and a calculated pump-probe trace. The calculation uses $D_a=20 \text{ cm}^2/\text{s}$, $\tau_{\text{rec}}=100 \text{ ps}^2$ measured far away from the FIB patterned area, and $\tau_t=0.3 \text{ ps}$. The faster trapping time as compared to sample 100/2000 reflects the higher implantation dose. Trap filling could be neglected in sample 200/400 due to the larger dose and the larger ratio of implanted to unimplanted area.

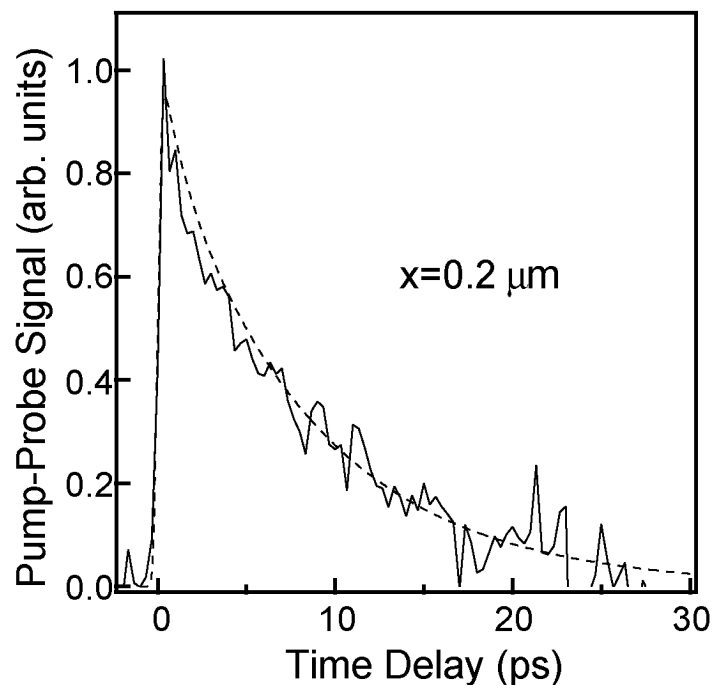


Fig. 3.6 Sample 200/400 (200 nm implanted stripes, 400 nm spaces): (a) Measured (solid) and calculated (dashed) normalized pump-probe trace 0.2 μm away from the center of an implanted stripe.

Both the experimental and the calculated pump-probe traces show a single exponential decay in the time window from 2 ps to 30 ps. This is because the higher spatial harmonics have diffusion decay times of less than 2 ps in sample 200/400 and the initial diffusion regime is already over at 2 ps. This

implies that the term $A\exp(-\Delta t/\tau_1)$ of the fit function $A\exp(-\Delta t/\tau_1)+B\exp(-\Delta t/\tau_2)$ has decayed to zero in the time window of observation. Therefore, a single exponential decay is obtained and τ_2 can be determined from a fit to the function $B\exp(-\Delta t/\tau_2)$.

The decay times τ_2 of measured and calculated traces are plotted versus position in Fig. 3.7 together with the pump-probe amplitude at $\Delta t=0$. Between the implanted stripes, the time constants τ_2 of about 8 ps are much faster than the recombination time. Spatial averaging and trapping do not determine these time constants, as shown by the rise of the amplitude and the arguments presented for sample 100/2000.

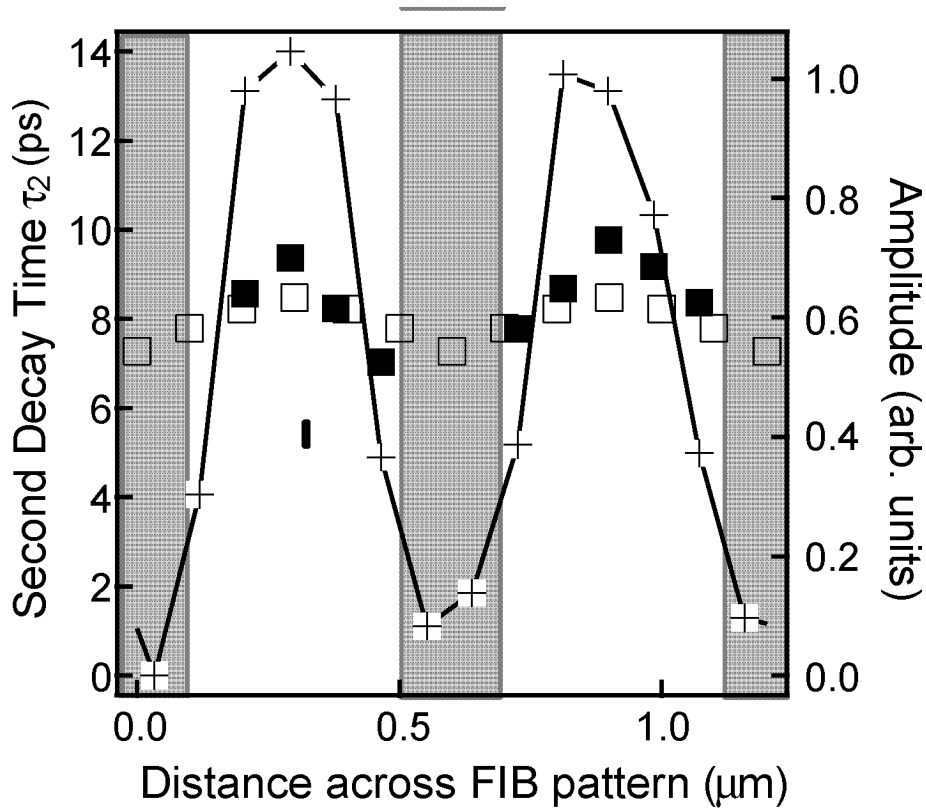


Fig. 3.7 Sample 200/400: Second decay time, describing the long-time diffusion regime, from fits to measured (filled squares) and calculated (open squares) pump-probe traces and pump-probe amplitude at zero time delay (crosses) vs. position.

The decay between the implanted stripes is dominated by diffusion in the long-time diffusion regime, unperturbed by the much slower recombination. The decay time depends only very weakly on position, as expected for quasi-sinusoidal carrier profiles in this regime. We note that diffusion could not have

been studied by far-field transient grating techniques [89] in sample 200/400 since diffraction of 800 nm light from a grating with a 600 nm period is impossible.

3.3 FIB QW summary

In this chapter we have presented, that femtosecond NF spectroscopy allows to experimentally observe different diffusion regimes in semiconductor nanostructures. The results directly demonstrate a complex dependence of spatiotemporal carrier dynamics on the lateral structure and the time window of observation.

With respect to the transport studies presented in the next chapter, we would like to emphasize that the signature of diffusive transport in square-like carrier density profiles is the spatial dependence of the decay of the pump-probe traces. The decay becomes faster as the probe position is moved towards the edge of the square-like carrier density profile.

4 Carrier and field dynamics around nano-scale Schottky contacts

In this chapter we will present carrier transport dynamics in nanostructured samples with intrinsic trapping centers and electric fields. Such transport dynamics is the generalized continuation of the diffusion dynamics, studied in the previous chapter 3.

In many metal-semiconductor composite materials Schottky contacts are formed at the interfaces between the semiconductor and the metal inclusions. Around the Schottky contacts electric fields and potentials exist even if no external bias field is applied [90]. If charge carriers are optically excited in such a material, the dynamics of the carriers will be substantially influenced by the built-in electric fields. More specifically, the fields will separate positive and negative charges. This charge separation results in the generation of space charge, which, in turn, changes the electric field distribution. Thus, complex carrier and field dynamics can be anticipated. If the metal inclusions act as carrier trapping centers, one expects that the built-in fields also directly affect carrier trapping into the metal. This is because the electric fields lead to carrier transport towards or away from the metal-semiconductor interface, depending on the sign of the charge and the direction of the fields.

Without external bias, the electric field is non-zero only in the depletion zone of a Schottky contact with a typical extension in the micro- or submicrometer range. This short length scale implies that the carrier dynamics occurs on a short time scale [91]. Therefore, only experimental techniques with both high temporal and high spatial resolution can provide detailed insight into the carrier dynamics close to a Schottky contact. As a consequence, femtosecond-resolved pump-probe measurements in the optical near-field (NF) lend themselves well to the study of carrier dynamics around Schottky contacts.

In this chapter, we present a comprehensive study of free carrier and field dynamics around nano-scale Schottky contacts. Experimental data are obtained using both conventional spatially averaging FF and spatially resolving NF pump-probe techniques. The experiments have been performed on a lithographically produced model system, which consists of tungsten (W) nanodisks embedded

in GaAs. The pattern of the embedded W disk can be chosen by the lithographic fabrication process. It is therefore possible to adjust the spacing between the disks for the desired purposes.

By means of far-field measurements we will identify the metallic inclusions as efficient trapping centers at high optically excited carrier densities. In this regime, carrier transport towards and trapping into the metal is efficient and occurs on a picosecond time scale. We find that smaller disk spacings result in shorter time constants in these spatially averaged measurements. Thus, control of the disk spacing allows one to tailor the structures for ultrafast applications.

More details will be inferred from spatially and time resolved near-field measurements. In samples with larger disk spacing the depletion zones of adjacent disks do not overlap [92]. In such samples, the femtosecond NSOM pump-probe measurements reveal the ultrafast carrier dynamics in the close vicinity of a *single* tungsten nanodisk in GaAs. Thus, we can directly observe the interplay between free carrier and field dynamics and carrier trapping around a *single* Schottky contact. This experimental approach avoids complications due to averaging over an ensemble of Schottky contacts, which arise in the far-field experiments.

We will present systematic experimental and theoretical investigations of the complex spatio-temporal carrier dynamics around nano-scale Schottky contacts in different carrier density regimes. We will introduce a theoretical model based on a selfconsistent treatment of the drift-diffusion equation for the carriers and Poisson's equation for the electric field. The model allows us to calculate the electron and hole dynamics as well as the temporal and spatial variation of the electric field and potential around a single Schottky contact. Two different carrier density regimes are revealed by the measurements and the calculations. At lower carrier densities, the built-in electric field is only weakly reduced, leading to a repulsion of electrons from the Schottky barrier. Therefore electron trapping into the W disk is strongly suppressed. In contrast, at higher carrier densities, the built-in field is screened, resulting in an efficient diffusive electron transport towards and trapping into the W disk. In both density regimes, the experimental data and the numerical calculations are in very good agreement.

Another important metal-semiconductor composite material is annealed low-temperature (LT) grown GaAs, which can be produced without lithographic processing. Annealed LT-GaAs contains metallic As precipitates [93], which can

form Schottky contacts with the embedding GaAs [93, 94]. Ultrafast carrier trapping times into the As precipitates [95] and high resistivity [81, 96] make this metal-semiconductor composite material very attractive for many optoelectronic and photonic devices. Examples include terahertz emitters [97], ultrafast photoconductive switches [98], ultrafast all-optical switches [99], and semiconductor saturable absorbers [100]. We will show in the last section of this paper that optical far-field experiments on annealed LT-GaAs can be described by the picture of carrier and field dynamics that has been deduced from the experiments on the *W*-disk material with Schottky contacts. The study of a *single* As precipitate in the NF is not possible as the typical distance between precipitates is well below 100 nm [101], i.e., smaller than the spatial resolution of our ultrafast NSOM.

4.1 Sample descriptions and experimental set-up

In this section we introduce the tungsten disk and the LT-GaAs sample and explain briefly the experimental conditions. We describe the design and the fabrication of the samples as well as the process used to prepare the *W* disk sample for near-field experiments.

4.1.1 *W* disk structure

The investigated tungsten disk sample has been grown by metalorganic vapor phase epitaxy (MOVPE). On a GaAs substrate we have grown AlAs/GaAs etch stop layers, a 20 nm GaInP protection layer and a 20 nm thick GaAs layer. Afterwards, *W*-disks with ~80 nm diameter and a thickness of 20 nm have been deposited in a rectangular pattern with 0.3, 1 and 2 μm disk spacing as shown in Fig. 4.1 by electron beam lithography and a subsequent lift-off process. The disks have then been epitaxially overgrown with an 80 nm thick GaAs layer, followed by a 500 nm thick GaInP layer. The exact structure of the sample is depicted in Fig. 4.2. The GaAs is n-doped (electron density $\sim 10^{16} \text{ cm}^{-3}$) and Schottky barriers are formed at the *W*/GaAs interface [92, 102]. A detailed description of the fabrication process can be found in Ref.[92] and [102]. With respect to our choice of system, we like to mention that *W*-disk/GaAs structures have potential for semiconductor device technology as the electrical properties

of the GaAs can be changed from conducting to semi-insulating by varying the disk spacing [102].

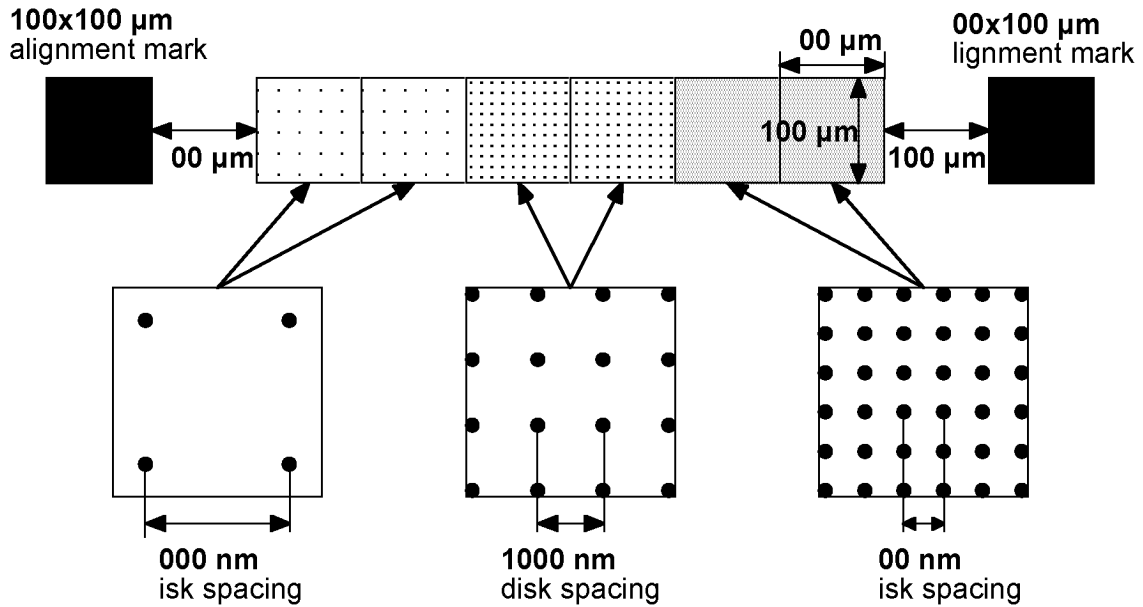


Fig. 4.1 W disk pattern produced by electron beam lithography and subsequent lift-off process. There are two fields for each disk spacing. The 6 fields are aligned between two tungsten alignment marks that are visible in a normal optical microscope to coarsely position the NSOM tip.

500 nm GaInP mechanical support
80 nm GaAs overgrowth
W disk pattern
20 nm GaAs
20 nm GaInP passivation layer (top surface after etching)
10 nm GaAs layer
3 nm GaAs passivation layer
40 nm AIAs
100 nm GaAs
300 nm AIAs
GaAs substrate

Fig. 4.2 Layer sequence of the W disk sample grown on a GaAs substrate.

As discussed already before, suitable samples for transmission NF measurements have to fulfill two main requirements. Light of the wavelength of interest should only be absorbed in the active region and the active region has to be as close as possible to the surface to preserve spatial resolution. Therefore we have glued our sample upside down on a glass substrate and removed the GaAs substrate and the etch-stop layers by chemical wet etching. The remaining structure, schematically shown in Fig. 4.3, consists of the absorbing GaAs with the embedded W-disks, sandwiched between high band gap GaInP layers. The bottom one acts as a mechanical support. The top one is very important as it serves as protection layer to avoid surface trapping of the optically excited carriers. On previous samples without a top GaInP layer, we have found that the carrier density decays very rapidly within a few picoseconds. This decay was independent of the position with regard to the W disk and therefore was attributed to surface trapping.

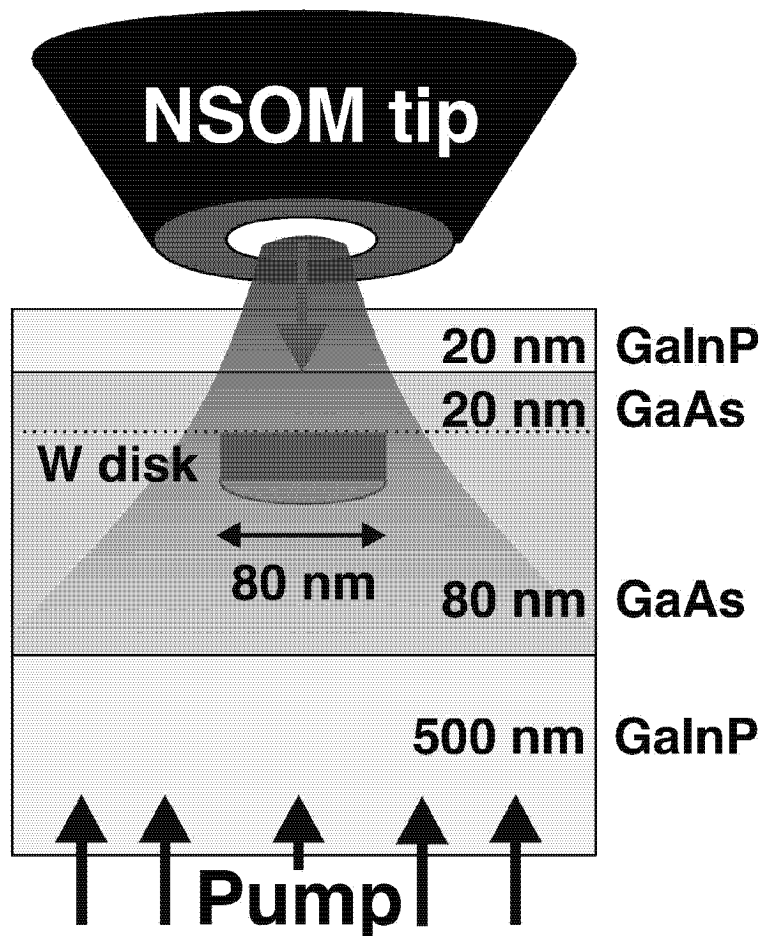


Fig. 4.3 Schematic illustration of the tungsten disk sample, showing the GaAs layer with the embedded W disk, sandwiched between GaInP layers. Additionally, the global pump / local probe NSOM configuration is depicted.

4.1.2 LT-GaAs sample

For comparison with the *W* disk sample we have designed an LT-GaAs sample, which is sufficiently n-doped to expect large built-in fields close to the As precipitates. Additionally, we have grown an undoped LT-GaAs sample to measure the carrier dynamics in the presence of only weak built-in fields. The two 500 nm thick LT-GaAs samples have been grown on a GaAs substrate by molecular beam epitaxy (MBE) at As_4/Ga -flux ratios of 3 and 4.5, respectively, and a growth temperature of 320 °C. One sample is undoped, the other one is n-doped with Si at a concentration of $1 \times 10^{18} \text{ cm}^{-3}$. This Si concentration has been chosen much larger than the concentration of ionized arsenic anitsites As_{Ga}^+ , which is smaller than $1 \times 10^{17} \text{ cm}^{-3}$ [95, 103]. Therefore the majority of the doping electrons will contribute to the formation of Schottky contacts with large built-in fields. After the growth, both samples have been annealed in-situ under arsenic overpressure at 600 °C for 1 hour. Such conditions ensure the formation of metallic As precipitates [93]. For transmission measurements, the GaAs substrate has been removed by chemical wet etching.

4.1.3 Experimental set-up

The far-field measurements on the *W* disk sample and the LT-GaAs samples have been performed with the NSOM setup described in chapter 2, in which the NSOM fiber has been replaced by a cleaved fiber, resulting in a probe spot diameter of $\sim 4 \mu\text{m}$ on the sample. The degenerate NF pump-probe measurements on the *W* disk sample are performed in the standard configuration with 100 fs pulses, centered at a photon energy of 1.46 eV. The *W* disk sample is excited uniformly from the bottom side with a pump beam of $\sim 10 \mu\text{m}$ diameter. All data have been taken at room temperature.

4.2 Theoretical model

We have performed numerical simulations in order to obtain a better understanding of the experimental NF pump-probe data. The electron and hole density and the electric field in the vicinity of a *W* disk are calculated with the drift-diffusion equation and Poisson's equation in a selfconsistent way (see equations 2.4, 2.5 and 2.7 in section 2.2.2). In our model, we neglect dynamics

in the direction perpendicular to the W disk plane. This simplification is justified by the geometry of the sample. The carriers are confined in a thin slab of 100 nm thick GaAs by the top and bottom GaInP layer. Therefore, carrier transport occurs mainly in the much larger W-disk plane. The symmetry of the W disk structure then allows us to use a one-dimensional model with the radius r in the W disk plane as the only space coordinate. The zero point is chosen at the center of the disk. The calculations of the electron/hole dynamics have been performed in an area extending from the W/GaAs interface at $r_{disk}=40$ nm (r_{disk} radius of a single W disk) to $r=1$ μ m. At $r=1$ μ m the influence of the W disk on the carrier dynamics has found to be negligible.

The internal static electric field $E_{intern}(r)$ inside the depletion region is obtained by a simple integration of Poisson's equation without optical excited carriers, analogous to the calculations in [90]:

$$E_{intern}(r) = \frac{qN_d}{2\epsilon} \left(r - \frac{w^2}{r} \right). \quad (4.1)$$

Here, q is the electron charge, $N_d=10^{16}$ cm⁻³ the donor impurity density and ϵ the dielectric constant of GaAs. Outside the depletion region E_{intern} is zero. The position of the edge of the depletion zone is denoted by w , measured from the center of the W disk. This position w can be obtained from

$$V_{bi} = \frac{q^2 N_d}{2\epsilon} \left(w^2 \log \frac{w}{r_{disk}} - \frac{1}{2} (w^2 - r_{disk}^2) \right) \quad (4.2)$$

Here, V_{bi} denotes the built-in potential. V_{bi} is given by the difference between the barrier height of the metal-semiconductor contact and the potential difference between the Fermi level and the conduction band energy outside the depletion region, see Fig. 4.4(a).

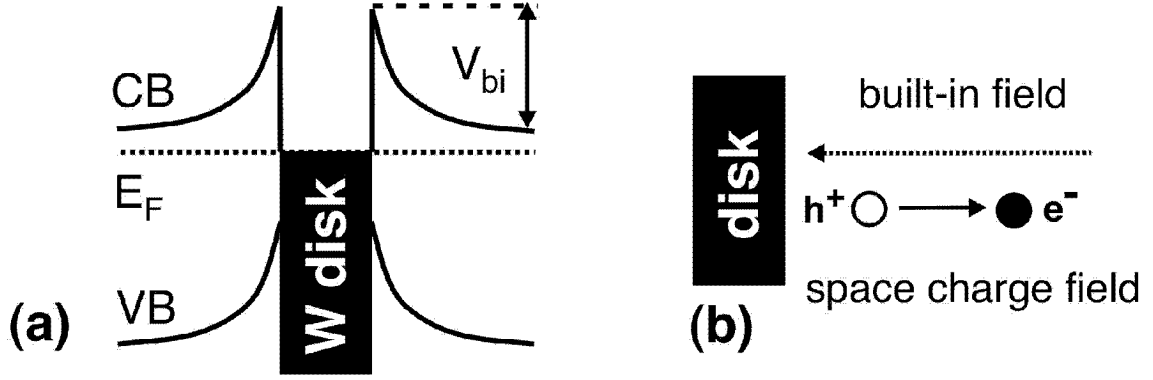


Fig. 4.4 (a) Schematic diagram of the GaAs band structure with the bent conduction and valence band (CB and VB, respectively) and the Fermi energy (E_F) around the W disk. V_{bi} denotes the built-in potential. (b) Schematic illustration of the built-in electric field pointing towards the disk. The field separates electrons and holes. The resulting space-charge field points in the opposite direction as the built-in field.

The dynamics of the electron density $n(r,t)$ depends on the total electric field E and the hole density $p(r,t)$ and is given by the continuity equation:

$$\partial_t n(r,t) = D_n \left(\partial_r^2 n + \frac{1}{r} \partial_r n \right) + \mu_n \left(\frac{n}{r} \partial_r (rE) + E \partial_r n \right) - Bnp + g(t) \quad (4.3)$$

$$\partial_t n(r_{disk}, t) = - \frac{n(r_{disk}, t)}{\tau_n} \quad (4.4)$$

The electron diffusion constant D_n and the mobility μ_n are linked by the Einstein relation (equation 2.6) and amount to 220 cm²/s and 8500 cm²/Vs [90], respectively. The term $-Bnp$ on the right-hand side of Eq. 4.3 accounts for bimolecular recombination. The spatially uniform carrier excitation is described by the r -independent generation term $g(t)$, for which we assume a sech² pulse with a full width at half maximum of 200 fs. The second equation describes the trapping of electrons into the disk at the W/GaAs interface, where τ_n denotes the trapping time. We have calculated τ_n multiplying the Richardson constant of 0.4 Acm⁻²K⁻² for electrons [104] with the surface of the W disk shell of 5x10⁻¹¹ cm² and the square of the room temperature. Following this procedure and dividing by the electron charge, a trapping time $\tau_n=90$ fs is deduced. This approach is based on the assumption that electron emission and trapping at the W/GaAs interface occurs at the same rate. Equivalent equations to Eq. 4.3 and 4.4 are used to calculate the hole density $p(r,t)$. The corresponding values for D_p

and μ_p are $10 \text{ cm}^2/\text{s}$ and $400 \text{ cm}^2/\text{Vs}$ [90], respectively. The trapping time $\tau_p=5 \text{ fs}$ is again obtained from the Richardson constant of $7 \text{ Acm}^{-2}\text{K}^{-2}$ for holes [104].

The electric field E is composed of the internal static field $E_{intern}(r)$ and the space-charge field, which is related to the dynamics of the electrons and holes by the equations:

$$E(r,t) = E_{intern}(r) + \frac{q}{\epsilon r} \int_{r_{disk}}^r r' (Q_{capt} \delta(r' - r_{disk}) + p - n) dr' \quad (4.5)$$

$$Q_{capt}(t) = \int_{-\infty}^t \frac{p(r_{disk}, t')}{\tau_p} - \frac{n(r_{disk}, t')}{\tau_n} dt' \quad (4.6)$$

The captured charge density Q_{capt} accounts for the trapped electrons and holes at the W/GaAs interface. The consideration of carrier trapping into the W-disks in our model results in a time-dependent total electric field at $r=r_{disk}$ in contrast to previous works [105, 106], where trapping has been neglected. From the electric field we can deduce the electric potential $U(r,t)$ integrating the equation $E(r,t) = -\partial_r U(r,t)$. The integration has been performed for the boundary condition $U(r_{disk}, t) = \text{const.}$, i.e., the potential at $r=r_{disk}$ is kept fixed while it varies with time for $r > r_{disk}$. This choice of boundary condition emphasizes that the Schottky barrier height remains constant, whereas the potential barrier is changing. Note that, for the interpretation of the physics, only the potential difference between $r=r_{disk}$ and $r > r_{disk}$ matters.

All parameters for the calculations are taken from literature, except for the built-in potential V_{bi} and the bimolecular recombination constant B . Those parameters are obtained by comparing the simulations with the experimental results. We find for the built-in potential $V_{bi}=0.15 \text{ eV}$, leading to the depletion region edge at $w=160 \text{ nm}$. We like to recall that V_{bi} denotes the built-in potential and not the full Schottky barrier height. As shown in Fig. 4.4(a), V_{bi} is smaller than the full Schottky barrier height. The bimolecular recombination process is introduced, because the experiments have shown that the decay of the electron density far away from the disks is strongly dependent on the density. Such a behavior cannot be modeled by a monomolecular recombination process. From the comparison with the measurements, we deduce a bimolecular recombination constant of $B=5.6 \times 10^{-7} \text{ cm}^3/\text{s}$. The large value of B compared to the bimolecular *radiative* recombination constant ($\sim 10^{-10} \text{ cm}^3/\text{s}$ in GaAs [107])

suggests that the bimolecular recombination process is nonradiative and possibly related to impurities.

The comparison of the experimental results with the numerical simulations and the discussion in Sec. 4.4 are based on the assumption that the pump-probe traces directly reflect the carrier density dynamics in the GaAs [2]. As we detect the pump-induced transmission changes at an energy close to the band edge, the electrons yield the major contribution to the pump-probe signal [108]. Therefore, we compare the calculated electron density n to the experimental pump-probe data. In such comparisons, we convolute the calculated electron density n with a Gaussian function that accounts for the spatial resolution of 230 nm in the experiment⁴. If no comparison is made to experimental data, the calculated data are not convoluted, i.e., unlimited spatial resolution is assumed when presenting purely theoretical results. In this way, maximum information is obtained.

4.3 Far-field experiments

The far-field measurements presented in this section are important to identify the metallic inclusions as efficient trapping centers at high optically excited carrier densities. Fig. 4.5 shows FF pump-probe traces obtained from the pattern with 0.3 μm disk spacing at different optically excited carrier densities. At low carrier densities, the differential transmission signal $\Delta T/T$ is essentially constant over 80 ps. In contrast, above a threshold carrier density, we observe a fast decay within the first 20 ps, followed by a contribution that decays very slowly. The transition from the quasi-constant signal to the decaying one occurs at a carrier density of approximately 10^{16} cm^{-3} , equal to the doping level.

⁴ As the W disk plane is 40 nm away from the NSOM tip, the spatial resolution is reduced to 230 nm even though the aperture of the tip is smaller.

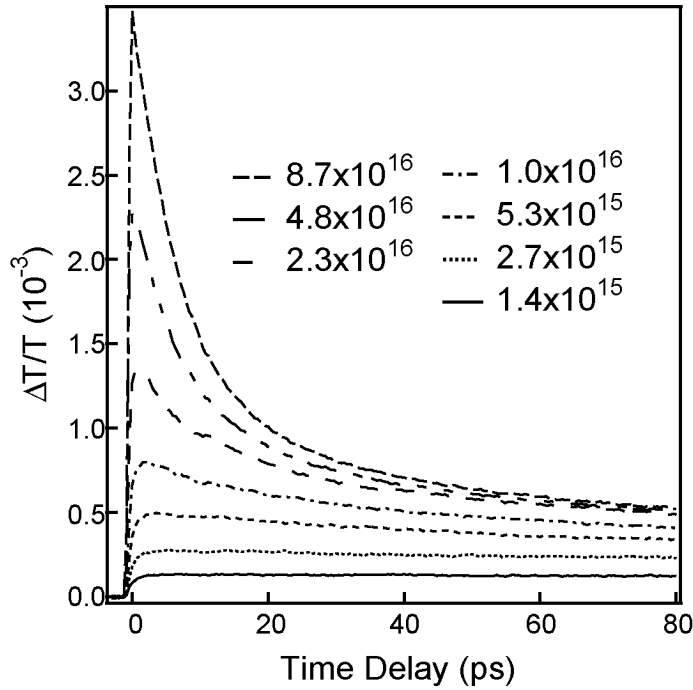


Fig. 4.5 Far-field differential transmission traces from the sample region with 0.3 μm W disk spacing for different carrier densities (in cm^{-3}).

Decay times τ are extracted fitting the pump-probe traces to $\left(\frac{\Delta T}{T}\right)_{\text{offset}} + \left(\frac{\Delta T}{T}\right)_{\text{fast}} e^{-\Delta t/\tau}$ (Δt time delay). The offset $\left(\frac{\Delta T}{T}\right)_{\text{offset}}$ describes the long time behavior and is assumed to be time-independent in the time window of observation; $\left(\frac{\Delta T}{T}\right)_{\text{fast}}$ is the amplitude of the time dependent signal contribution. The decay times τ are shown in Fig. 4.6 versus carrier density for the three different disk spacings. We observe a faster decay for smaller disk spacings. This result indicates that the disks are responsible for the fast decay but not intraband relaxation processes, which should not depend on the disk spacing. Moreover, Fig. 4.6 demonstrates that the decay time can be controlled by the disk spacing and can be as short as 10 ps.

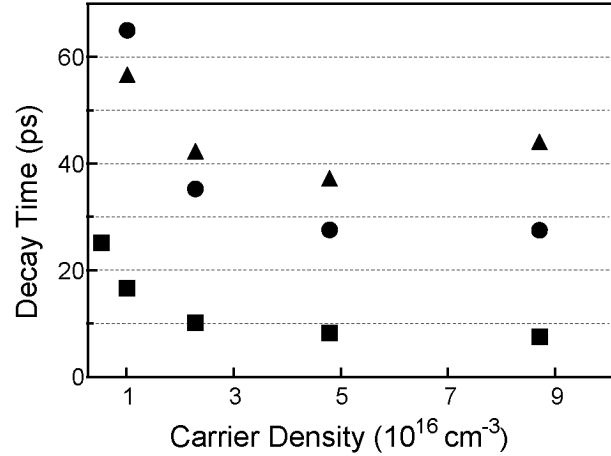


Fig. 4.6 Decay times τ vs carrier density for different disk spacings: 0.3 μm (squares), 1 μm (circles), 2 μm (triangles).

In Fig. 4.7 we have plotted $(\Delta T/T)_{fast}$ and $(\Delta T/T)_{offset}$ versus carrier density for the three different disk spacings. One can clearly see that the amplitude $(\Delta T/T)_{fast}$ substantially contributes to the pump-probe signal only above the threshold density of $\sim 10^{16} \text{ cm}^{-3}$. Above this density, the amplitude $(\Delta T/T)_{fast}$ increases linearly with carrier density. In contrast, the offset is constant at higher carrier densities.

In the following, we assume that the pump-probe traces directly reflect the carrier dynamics in the GaAs [2] in the presence of Schottky contacts and built-in electric fields. Before optical excitation, the built-in fields in the depletion regions of the Schottky contacts point to the W disks, i.e., the bands are bent upwards [102], as shown in Fig. 4.4. At optically excited carrier densities smaller than the doping density, any changes in the space-charge region can be neglected and the built-in fields and the band bending persist. Thus, the transport of optically excited electrons towards the W disks is suppressed since diffusion towards the W disks and drift away from the disks cancel each other. As a consequence, most of the electrons remain in the GaAs where they recombine on a nanosecond time scale [90]. This slow process is observed in the pump-probe traces since electrons yield the major contribution to the signal for detection close to the band edge [108].

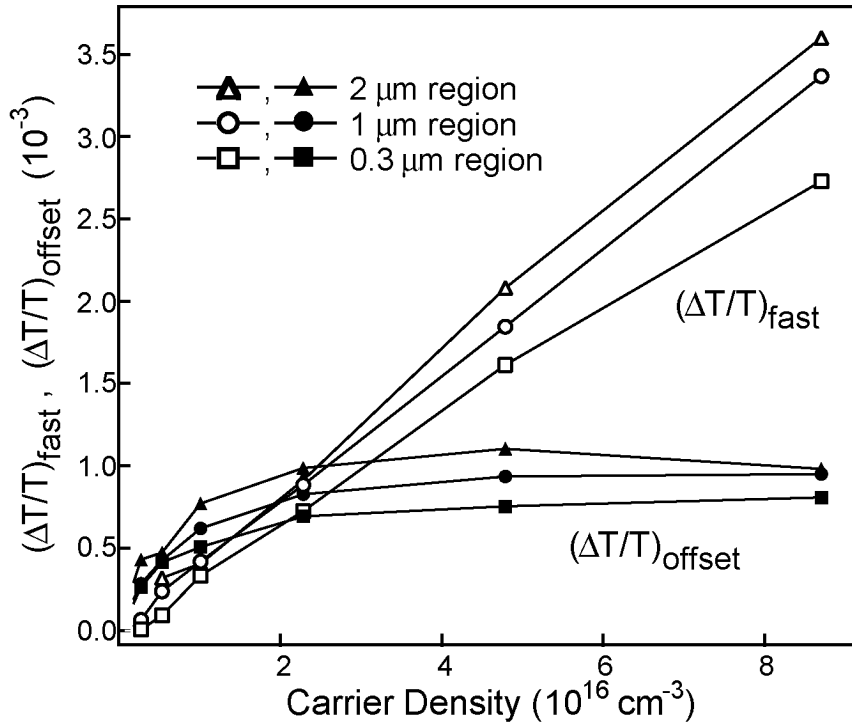


Fig. 4.7 Amplitude (open symbols) and offset (filled symbols) of far-field pump-probe traces obtained from exponential fits vs carrier density for different disk spacings.

We note that the holes in the depletion region move towards the W disks driven by the built-in field. If the optically excited carrier density exceeds the doping density, a substantial screening field builds up as the electrons and holes are separated. The total field is decreased and the band bending is diminished [109]. Both electrons and holes can then diffuse towards the W disks where they are trapped and recombine. We attribute the fast decay seen for initial optically excited carrier density $>10^{16} \text{ cm}^{-3}$ to this effect. Once the carrier density has decreased to $\sim 10^{16} \text{ cm}^{-3}$, the built-in field is restored. Then electron transport towards the disks is again suppressed, reflected by the offset $(\Delta T/T)_{\text{offset}}$ of the pump-probe data. These conclusions are strongly supported by the density dependence of the data in Fig. 4.5, Fig. 4.6 and Fig. 4.7. We like to emphasize that the decay time τ includes the dynamics of diffusion towards the disks as well as trapping and recombination at the disks.

Additional and much more detailed insight into the carrier dynamics are obtained from near-field measurements, which support the previous reasoning.

4.4 Near-field experiments

In this section we will present and discuss near-field measurements and simulations of the carrier dynamics in the 2 μm W disk sample. Two different cases are considered, namely carrier dynamics at lower and at higher optically excited carrier densities. With respect to our analysis of the carrier dynamics, we like to recall the properties of the built-in potential and field close to a Schottky contact before optical excitation. A schematic illustration is shown in Fig. 4.4 (a) and (b), respectively.

4.4.1 Low-density regime

First, we will discuss the carrier and field dynamics for a low optically excited carrier density of $6 \times 10^{15} \text{ cm}^{-3}$. Fig. 4.8 shows pump-probe traces taken either over or 1 μm away from a W disk. Apart from a small difference in amplitude both traces look the same. The curves are essentially constant within the 10 ps time window of the measurement. No fast dynamics is observable, neither over the disk nor far away, in this experiment with a temporal resolution of 250 fs. We conclude that carrier trapping is inefficient despite the presence of a trapping center in form of the W disk.

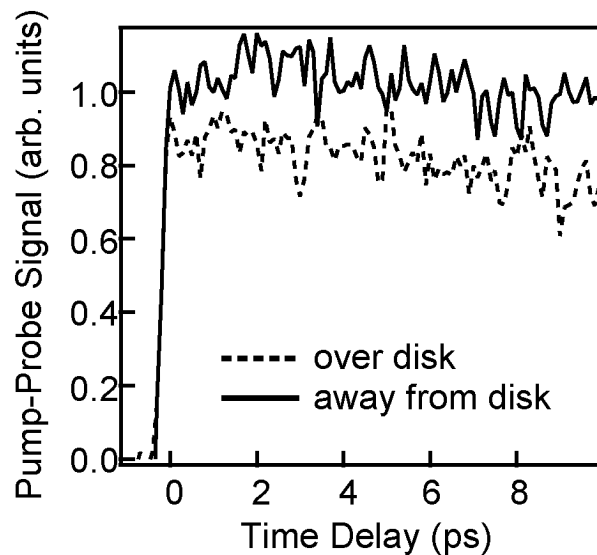


Fig. 4.8 Low-density regime: near-field pump-probe traces taken either over (dashed line) or 1 μm away (solid line) from the W disk.

Fig. 4.9(a) shows a 2-dimensional (2D) image of the pump-probe signal taken at a time delay of $\Delta t=2$ ps. In the center of the image, where the W disk is located, a clear reduction of the signal is visible. Around this region, one observes a ring-shaped region in which the nonlinear signal is slightly larger. The same features are seen in the 2D-image of the calculated electron density in Fig. 4.9(b). The 2D images suggest electron transfer from the border of the disk to the outside region, leading to a reduction of the electron density over the disk and to an enhancement of the density at a distance of 200 nm around the disk. One might wonder why this process does not lead to a fast decaying contribution to the pump-probe trace in Fig. 4.8 that has been taken over the disk. The absence of such a fast decaying signal (Fig. 4.8) is due to the finite temporal resolution of ~ 250 fs. We conclude that the electrons are redistributed already during the pump excitation pulse, resulting in the electron distribution seen in Fig. 4.9 at $\Delta t=2$ ps. This interpretation is confirmed by the numerical simulations that will be discussed next. The numerical simulations also confirm that carrier trapping into the W disk is inefficient in the low-density regime and elucidate the reason for this experimental finding.

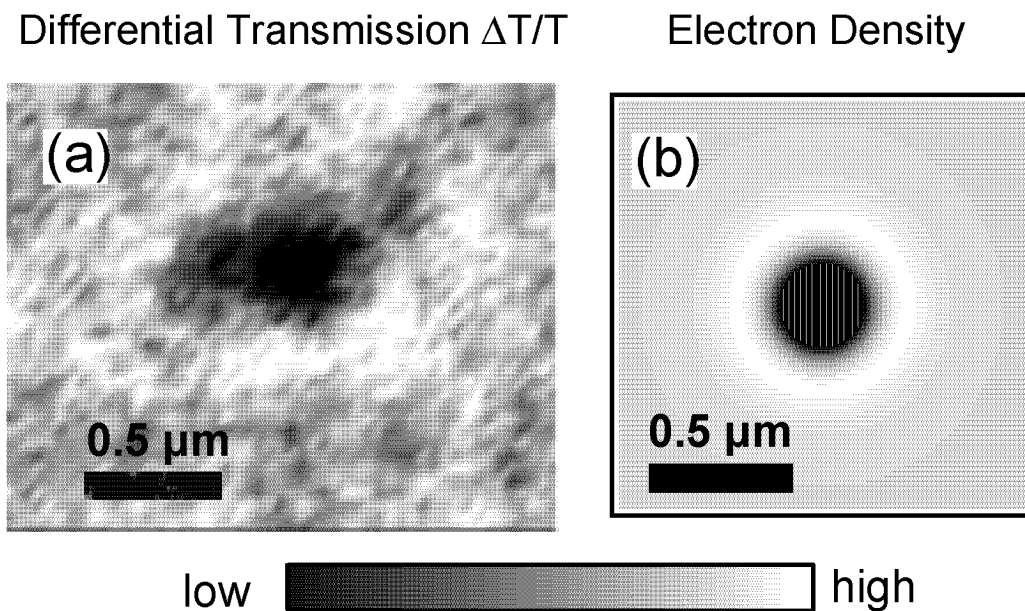


Fig. 4.9 Low-density regime: (a) two-dimensional optical near-field image of the differential transmission $\Delta T/T$ taken at a time delay $\Delta t=2$ ps over a single W disk at an optically excited carrier density of 6×10^{15} cm^{-3} . (b) Calculated electron density obtained from the theoretical model of Sect. 4.2 for the experimental condition of (a).

With regards to the simulations, we like to emphasize that very good agreement between the calculated and the experimental data is obtained in Fig. 4.9. This result testifies to the validity of the model presented in section 4.2. In particular, it is a valid procedure to identify the pump-probe signal with the electron density and to neglect hole contributions, many-body effects [2], and field-induced transmission changes due to the Franz-Keldysh effect [110]. As a consequence, we can extract the spatial dependence and the temporal evolution of important parameters from the model.

Fig. 4.10 shows the electron density n , the hole density p , the total electric field E and the (energy) potential $-|q|U$ vs. distance r from the center of the disk for different time delays Δt . We begin with the discussion of the total electric field E and the potential $-|q|U$. Later, we will comment on the dynamics of the electrons and holes. We like to recall that all four variables n , p , E and $-|q|U$ are coupled by the equations of section 4.2 and, therefore, should always be considered together. In Fig. 4.10(a) we show the temporal evolution of the total electric field. The trace at time delay $\Delta t = -1$ ps indicates the built-in field before optical excitation. The field is negative as it points towards the disk. After optical excitation the electron-hole pairs are separated by the electric field. The holes drift towards the disk, where they get trapped at the W/GaAs interface whereas the electrons drift away from the disk. The spatially separated electrons and holes induce a space charge field that is opposite to the built-in field; see the schematic picture of Fig. 4.4(b). Therefore, we find that the absolute value of the electric field decreases to less than half of its initial value within the first 10 ps. This behavior is reflected by the evolution of the energy potential in Fig. 4.10(b). The potential barrier is reduced to a third of its initial value within the first 10 ps. The field and the energy potential remain almost unchanged for several tens of picoseconds (data not shown). For example, the curves at $\Delta t = 10$ ps and $\Delta t = 40$ ps almost coincide. We like to emphasize that a considerable field and potential barrier remain after optical excitation. The remaining electric field leads to a non-negligible electron drift current away from the disk, which counteracts electron diffusion towards the disk. Thus, net electron transport to the disk is reduced and the trapping of electrons into the disk is inefficient, as seen from the pump-probe traces of Fig. 4.8.

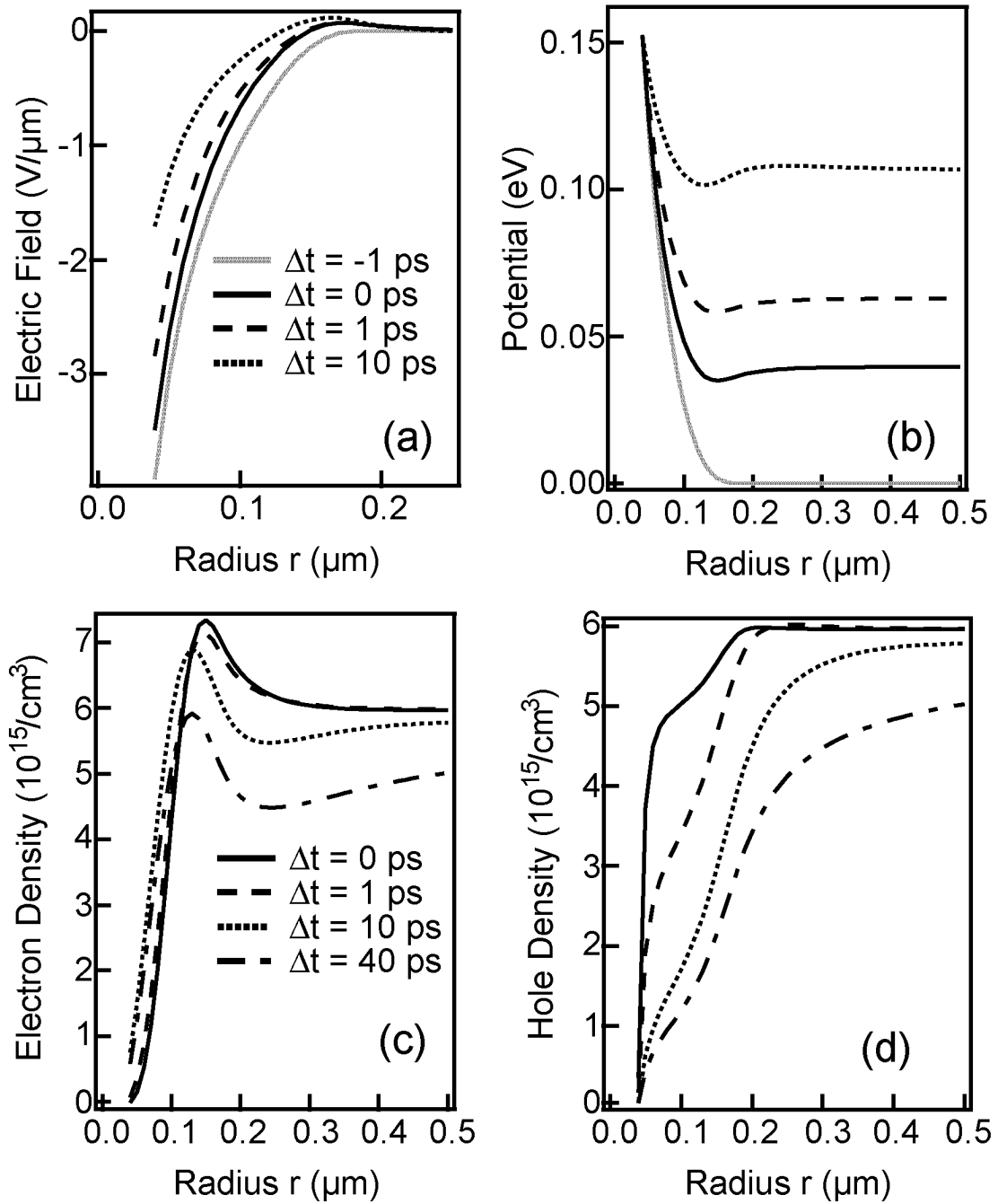


Fig. 4.10 Low-density regime: results from the theoretical model plotted vs. radius r from the center of the W disk at different time delays Δt . (a) electric field, (b) energy potential, (c) electron density and (d) hole density. In (a) and (b) the traces at $\Delta t = -1$ ps indicate the electric field and the potential before optical excitation. The legend in (a) applies to (b). Likewise, the legend in (c) applies to (d). Note the different r -scale in (a).

Focusing now on details of the field dynamics, one observes a sign change of the electric field and a dip in the potential at $r=0.14 \mu\text{m}$ already at very early time delays ($\Delta t=0 \text{ ps}$). The positive electric field for $r > 0.14 \mu\text{m}$ reflects the increase of the potential that leads to the formation of a potential well. The well is self-induced by the electron and hole dynamics and the resulting space-charge field, i.e., it arises from the coupling of the carrier and the electric field dynamics. From the discussion in the previous paragraph, it follows that the well persists up to 40 ps.

The temporal evolution of the electric field and the potential are closely related to the electron and hole dynamics shown in Fig. 4.10(c) and (d), respectively. Already during the pump excitation ($\Delta t=0 \text{ ps}$) the electrons are efficiently pulled away from the W disk by the electric field and accumulate at the edge of the depletion zone. This numerical result is in agreement with the absence of a fast contribution in the pump-probe traces of Fig. 4.8. The maximum in the electron density seen in Fig. 4.10(c) is consistent with the dip in the potential and the sign change of the electric field. In other words, the electrons accumulate in the potential well. The maximum in the electron density is the reason for the ring-shaped signal enhancement in Fig. 4.9. The maximum is still seen at $\Delta t=40 \text{ ps}$, corresponding to the long lifetime of the potential well.

The hole dynamics in Fig. 4.10(d) is dominated by hole drift and diffusion towards and trapping into the disk. These processes are slower than the corresponding electron processes due to the smaller hole mobility and diffusion constant. Nevertheless, these processes substantially reshape the hole distribution during the first 40 ps. In particular, diffusion smoothes the hole distribution. The weak overall reduction of both the electron and hole density is due to the inefficiency of bimolecular recombination at low carrier density.

4.4.2 High-density regime

In the high-density regime we consider an excited carrier density of $7-8 \times 10^{16} \text{ cm}^{-3}$, which is significantly higher than the doping level. Fig. 4.11 shows a 2D image of the pump-probe amplitude at a time delay of 15 ps. The disk pattern is clearly visible as the measured signal is substantially reduced over the disks.

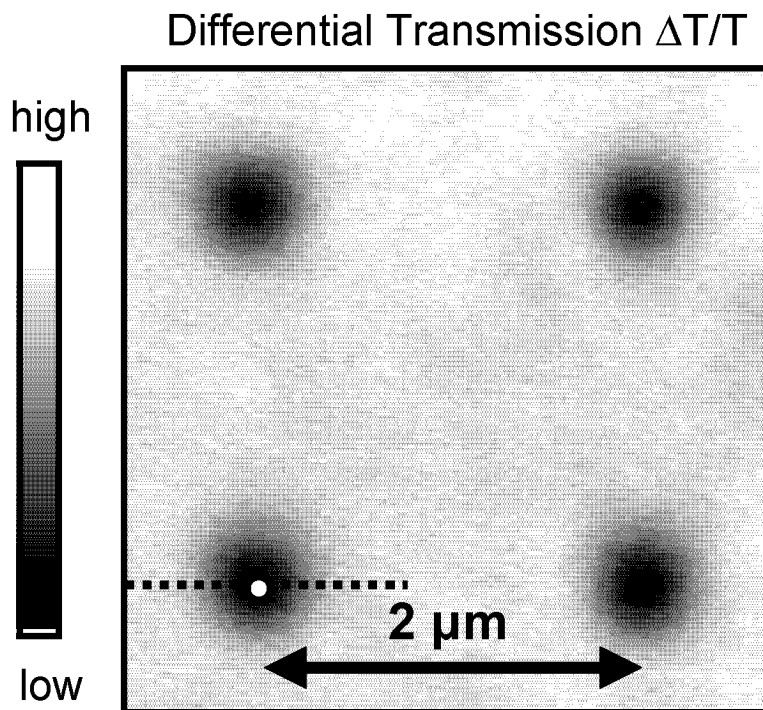


Fig. 4.11 High-density regime: two dimensional image of the differential transmission $\Delta T/T$ at time delay $\Delta t=15$ ps. The white disk in the lower left corner schematically marks the size of a W disk.

In Fig. 4.12 we show a line scan of the pump-probe signal together with a Gaussian function that indicates the spatial resolution in the experiment. The electron density is reduced not only over the disks, but also in a wide region around the disks. This region has a full width at half maximum (FWHM) of 410 nm and is much broader than the spatial resolution function with a FWHM of 230 nm. We conclude that the electrons from this region have moved towards the disk, where they have been trapped, in contrast to the dynamics seen in the low-density regime. Efficient electron transport towards the disks is only

possible if the built-in field is screened [25]. Otherwise electron drift away from the disks counteracts diffusion towards them, suppressing net electron transport. This reasoning indicates that diffusion is the main transport mechanism for electrons under this experimental condition.

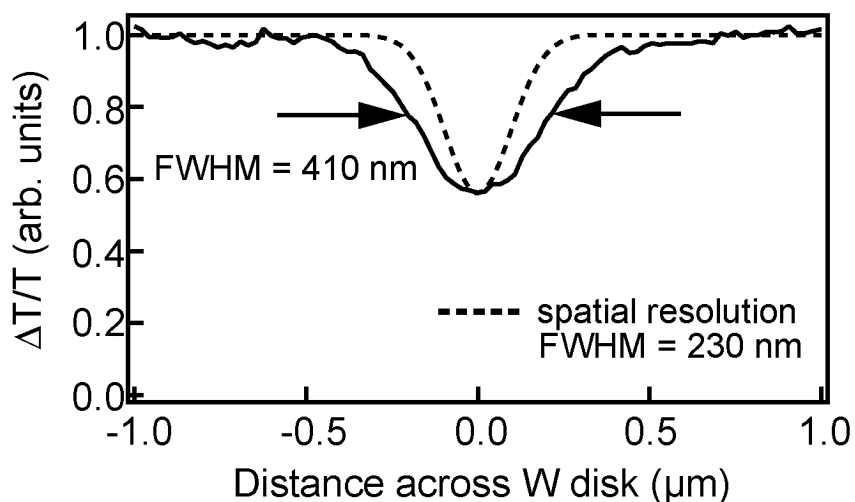


Fig. 4.12 High-density regime: Line scan of the differential transmission $\Delta T/T$ (solid line) along the dashed line in Fig. 4.11 together with a Gaussian function showing the spatial resolution (dashed line).

In Fig. 4.13, pump-probe traces are shown, which have been taken either over or 1 μm away from the disk. Over the disk, the signal decays within 7.5 ps to half of its initial value, significantly faster than away from the disk, where it takes 37 ps to reach the half-maximum point. Both traces decay faster than the corresponding low-density curves in Fig. 4.8. This data confirms that efficient electron trapping takes place in the high-density regime. Note that the density dependence of the bimolecular recombination cannot be the main reason for the results in Fig. 4.13. This is because bimolecular recombination alone would not lead to different decays at different positions.

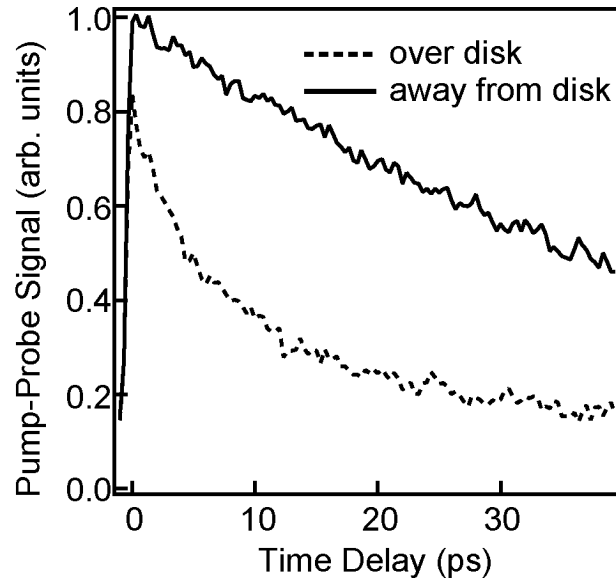


Fig. 4.13 High-density regime: near-field pump-probe traces taken either over (dashed line) or 1 μm away from the disk.

More details of the spatiotemporal carrier dynamics can be inferred from direct measurements of the pump-probe signal versus distance across a single W disk for fixed time delays Δt . These data together with the simulated electron density are shown in Fig. 4.14(a). At zero time delay, the electron density is mainly reduced in the close vicinity of the W disk. With time, the shape of the traces changes and a reduction of the electron density is also observed farther away from the disk. The calculated electron density agrees very well with the measured pump-probe line scans. The good agreement shows that the model of section 4.2 is also valid in the high-density regime. We will later on deduce details of the carrier and field dynamics from the model.

Fig. 4.14(b) shows how the FWHM of the dip increases with time. After an initial fast broadening of the signal dip, the increase of the FWHM slows down at longer time delays. A fast broadening of the carrier density dip has been found in quantum wells with artificially introduced trapping centers [22]. In such samples, only trapping and diffusion determine the carrier dynamics; carrier drift does not contribute. Therefore, the data of Fig. 4.14 suggest that the electron dynamics is strongly affected by diffusion during the first several picoseconds when the broadening of the pump-probe dip is pronounced. The overall signal reduction is due to the bimolecular recombination, which is efficient at high carrier densities.

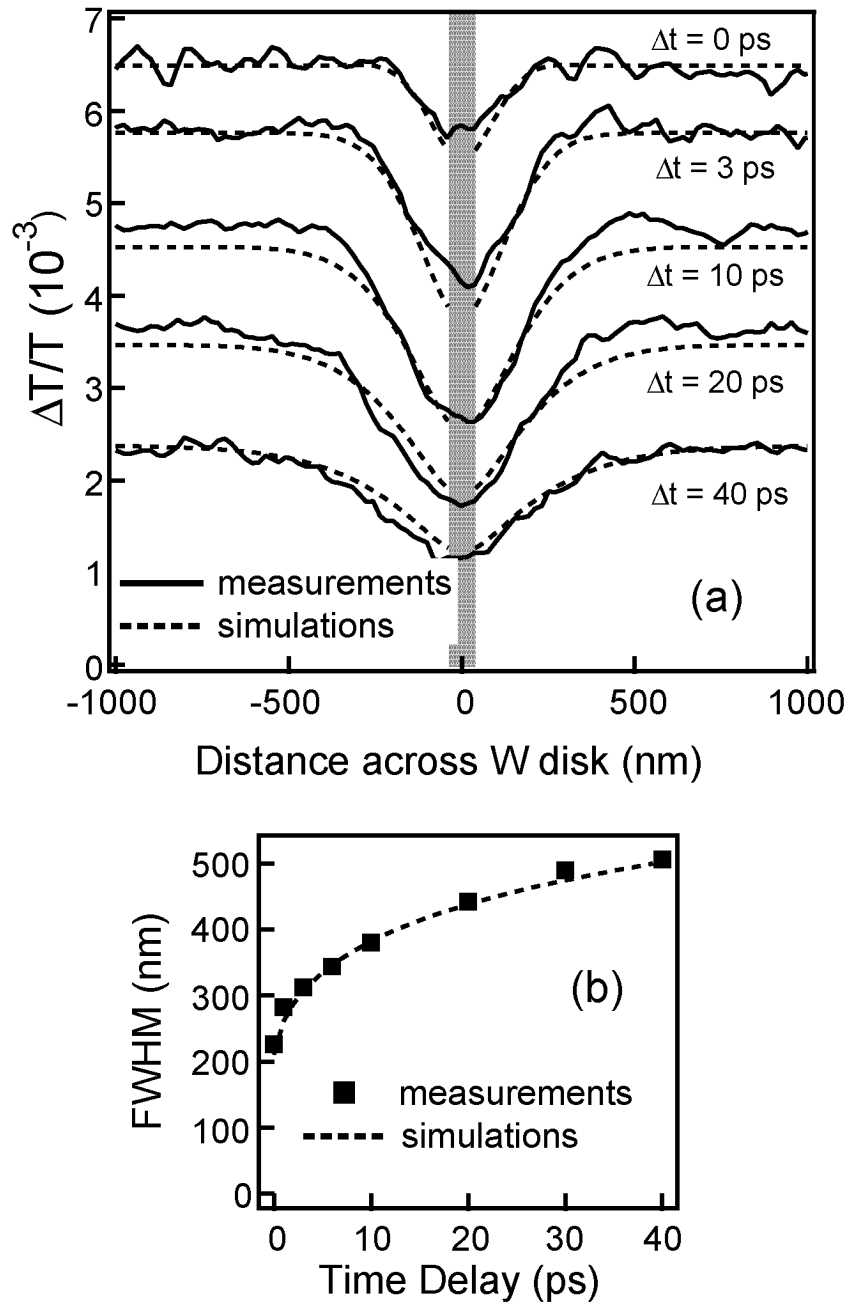


Fig. 4.14 High-density regime: (a) Line scans of the measured differential transmission signal (solid lines) and the calculated electron density (dashed lines) across a single tungsten disk for different time delays Δt . The gray bar marks the extension of the tungsten disk. (b) Full width at half maximum (FWHM) of Gaussian fits to the measured curves (squares) and FWHM of Gaussian fits to calculated traces (dashed line).

Summarizing the results of Fig. 4.11 to Fig. 4.14, the experimental data indicate that the electric field is strongly screened in the high-density regime, giving rise

to efficient diffusive transport of electrons towards the W disk and efficient electron trapping. These results are reconfirmed by the numerical simulation shown in Fig. 4.15. Fig. 4.15(a) demonstrates that the electric field is considerably suppressed almost immediately after excitation, in contrast to the low-density regime. Likewise, the energy potential is almost flat, as shown in Fig. 4.15(b). In the high-density regime, where the excitation density is well above the doping level, already at short times the built-in field is efficiently screened by the large amount of holes that are rapidly trapped into the W disk. At longer time delays the electric field and the potential slowly recover. The recovery is clearly seen if one compares the potential curves at 1 ps and 40 ps in Fig. 4.15(b).

In Fig. 4.15(c) and (d) we present the calculated electron and hole densities. During the excitation at $\Delta t=0$ ps the electrons are removed from the W disk border by the internal electric field and we observe a maximum of the electron density at the edge of the depletion zone (Fig. 4.15(c)). Compared to the low-density situation this drift induced process is weaker at higher densities and disappears almost immediately⁵. Following the optical excitation, the electric field rapidly breaks down. As a consequence, drift contributions can be neglected and diffusion dominates the carrier transport in the first 10 ps after excitation. Electrons and holes are transferred to the disk, where they get trapped and recombine. The diffusion dynamics is driven by the carrier density gradient resulting from carrier trapping into the W disk. Additionally, diffusion smoothes out the electron and hole density profiles and therefore leads to the broadening of the pump-probe signal dip seen in Fig. 4.14(b).

As the diffusion is faster for electrons than for holes, the charge of the initially trapped holes is slowly compensated. This process and the significant reduction of the carrier density due to efficient carrier trapping and bimolecular recombination result in the slow recovery of the built-in electric field and the potential. Once the potential barrier has acquired a sufficient height, it again suppresses electron transport towards the disk. Therefore, electron trapping becomes less efficient at longer times. The suppression of electron transport and trapping at longer times is observed in Fig. 4.13. Fig. 4.13 shows that the

⁵ The maximum of the electron density is not visible in Fig. 4.11 and Fig. 4.14, because it is very weak. Moreover it is averaged out due to limited spatial resolution.

decrease of the pump-probe signal over the disk significantly slows down for long time delays, resulting in a signal offset.

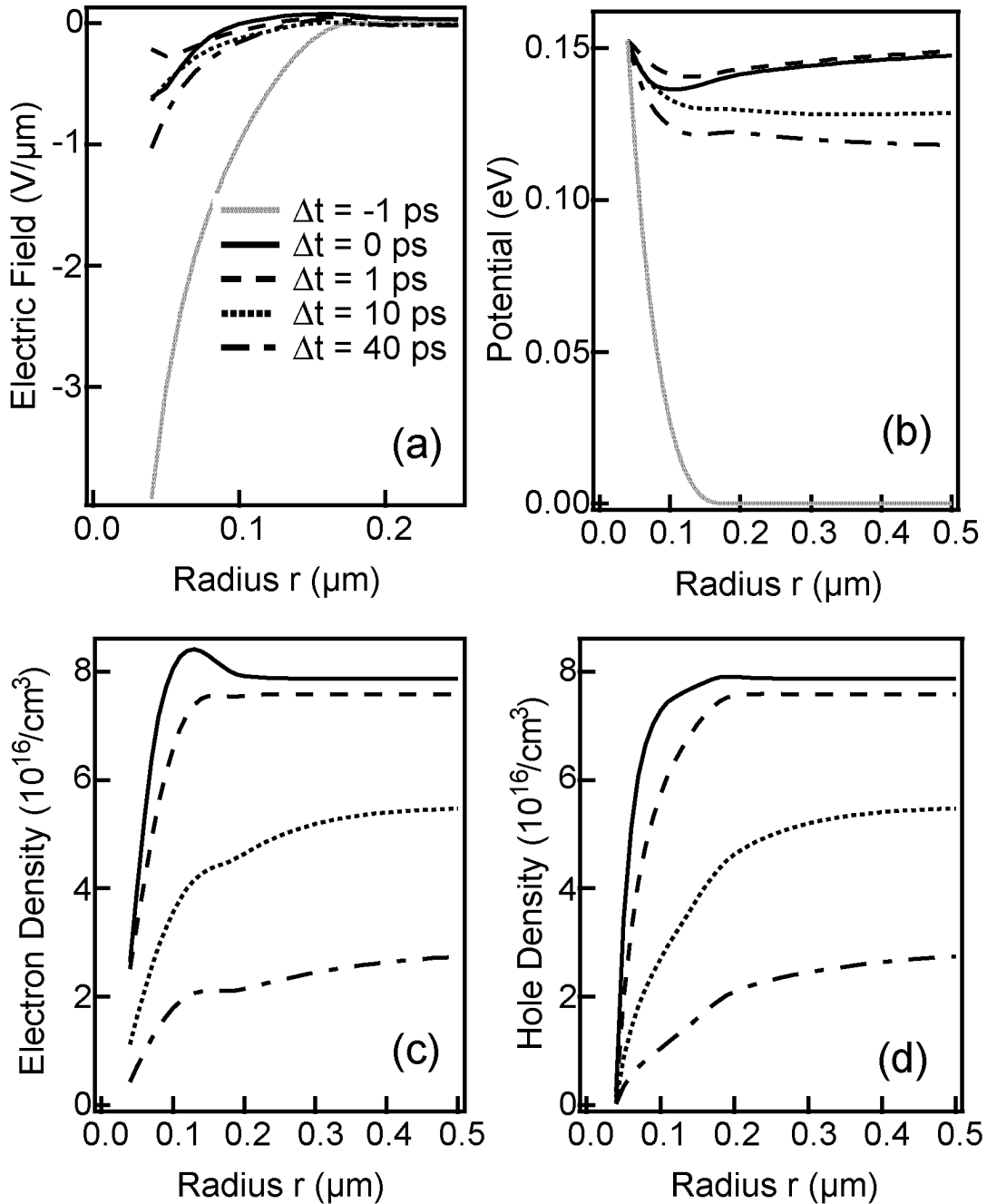


Fig. 4.15 High-density regime: Results from the theoretical model in the high-density regime plotted vs. radius r from the center of the W disk at different time delays Δt . (a) electric field, (b) energy potential, (c) electron density, and (d) hole density. In (a) and (b) the traces at $\Delta t = -1$ ps indicate the electric field and the potential before optical excitation. Traces for $\Delta t = -1$ ps are not shown in (c) and (d). The legend in (a) also applies to (b)-(d). Note the different r -scale in (a).

4.4.3 Annealed LT-GaAs

The results obtained from the study of the W disk model sample for nano-scale Schottky contacts can now be used to discuss the carrier dynamics in annealed LT-GaAs. Fig. 4.16 shows pump-probe signals for low and high optically excited carrier densities in undoped and n-doped LT-GaAs. The excitation photon energy is 1.46 eV. As shown in Fig. 4.16(a), in the undoped sample the signal decays exponentially for both low and high carrier densities with a typical $1/e$ time of 3.5 ps. We find the same decay even for carrier densities below 10^{15} cm^{-3} (data not shown). In Ref. [95] it has been shown that the decay of the pump-probe signal in undoped LT-GaAs is due to electron trapping into As precipitates. Fig. 4.16(a) shows that the efficiency of this fast trapping process is independent of the optically excited carrier density. We recall that electrons have first to move to the precipitates before being trapped at the metal/semiconductor interface. Therefore, we conclude that the built-in fields of the Schottky contacts around the precipitates in the undoped annealed LT-GaAs sample are too small to substantially suppress electron transport towards the As precipitates even at very low densities.

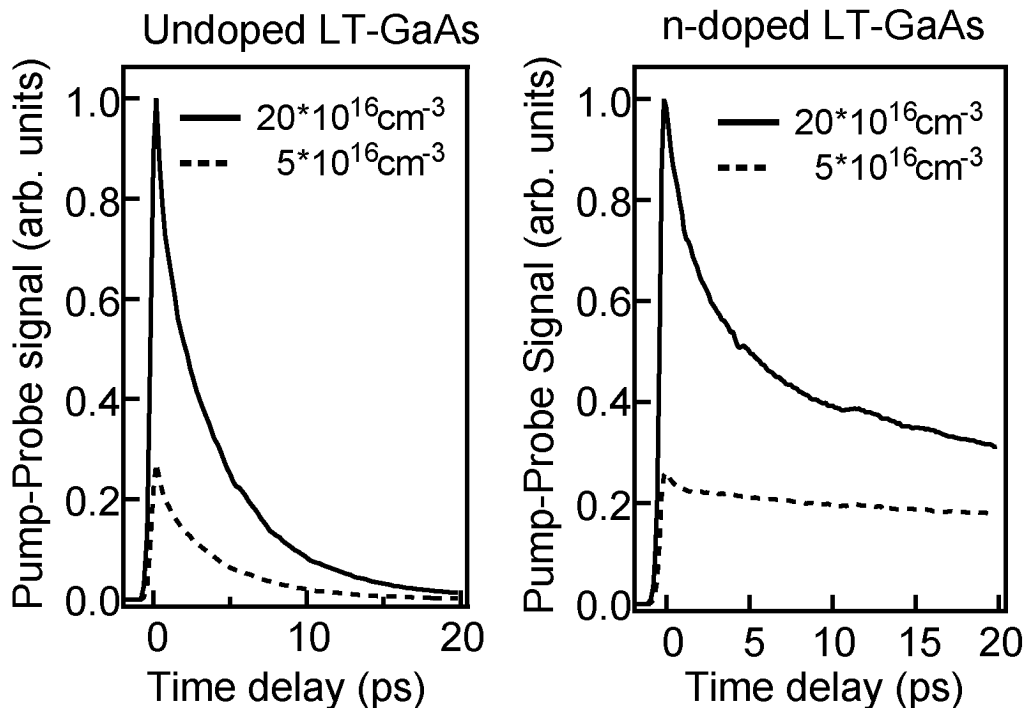


Fig. 4.16 Far-field pump-probe traces of undoped (a) and n-doped (b) annealed LT-GaAs samples taken at low (dashed lines) and high (solid lines) excitation carrier densities.

In contrast, the pump-probe signals in the n-doped sample show a strong carrier density dependence, as seen in Fig. 4.16(b). At high carrier densities, we find a fast initial decay that slows down at later times, resulting in an offset. At low carrier densities, there is no significant fast reduction of the signal, but the signal remains almost constant over the whole time window of the measurement. This behavior is very similar to the carrier dynamics that have been observed in the W-disk sample at low (Fig. 4.8) and high (Fig. 4.13) carrier densities. Therefore we conclude that the underlying physics is the same in both cases. As expected from the design of the n-doped LT-GaAs sample, our data indicate that strong built-in electric fields are present around the Schottky contacts before optical excitation in the n-doped LT-GaAs. At low optically excited carrier densities the fields suppress electron transport towards and trapping into the As precipitates. In contrast, at high carrier densities above the n-doping level, the trapped holes substantially screen the built-in fields, resulting in efficient diffusion and trapping of electrons. The electron transport is again suppressed when the optically excited electron density has substantially decreased to a value comparable to the doping level.

4.5 Nanoscale W-disk summary

We have presented a detailed study of the carrier and field dynamics around Schottky nanocontacts for different optically excited carrier densities. Tungsten disks embedded in GaAs have been investigated by femtosecond near-field optics. The dynamics has been modeled by the drift-diffusion and Poisson's equation. Experiments and numerical simulations agree very well and reveal two different density regimes. The low-density regime is characterized by the transfer of electrons away from the disk and their accumulation at the edge of the depletion zone. As the holes move towards the disk, a space-charge field is formed which points in the opposite direction as the built-in field. However, the space-charge field is weak. The total field and the corresponding potential barrier are still strong enough to suppress electron transport towards and electron trapping into the W disk. Hence, the optically excited electrons live for a long time outside the depletion region.

In the high-density regime, the built-in field is substantially screened by the trapped holes leading to efficient electron transport towards and trapping into the W disk. Once the carrier density is considerably reduced, the built-in electric

field is restored and electron trapping is again suppressed. These results demonstrate that the coupling of the carrier and field dynamics can substantially affect carrier trapping in metal-semiconductor composite materials in which Schottky contacts are formed.

As a second metal-semiconductor composite material, we have investigated annealed LT-GaAs, in which Schottky contacts are formed around metallic As precipitates. We have shown that the carrier dynamics significantly depends on the doping density of the LT-GaAs. In n-doped LT-GaAs, the dynamics is very sensitive to the optically excited carrier density: a fast decay of the electron population is observed at high densities and a slow one at low densities. In contrast, in undoped LT-GaAs, the electron population decays rapidly independent of the optically excited carrier density. Thus, the doping concentration and the optically excited carrier density are important parameters for the recovery time of devices produced from annealed LT-GaAs. We attribute the observed effects to the screening of the built-in fields and conclude that the same mechanisms are at work as in the *W* disk sample.

5 Quantization energy mapping of single V-groove GaAs quantum wires

Studies of single nanostructures are one of the most important applications of the femtosecond NSOM technique. Such studies allow one to gain insight into the intrinsic properties of nanostructures, unperturbed by spatial averaging over an ensemble of structures. Moreover, studies of single nanostructures can characterize growth inhomogeneities in nanostructured materials. In this chapter, we discuss experiments on single semiconductor quantum wires (QWRs). We will demonstrate that femtosecond NSOM measurements on single V-groove QWRs are possible with the instrument described in chapter 2. Moreover, we present a novel method for the mapping of quantization energy fluctuations along single quantum wires with nanometer-scale spatial resolution. This method takes advantage of the sensitive photon energy dependence of the near-field pump-probe traces around the lowest exciton resonance of the QWRs.

5.1 V-groove GaAs QWRs

The QWRs have been produced by low-pressure organometallic chemical vapor deposition (OMCVD) on V-groove substrates [111]. Quantum wires produced by this method are promising one-dimensional systems due to their large confinement energy [112]. The basic idea relies on the self-ordering of extremely narrow channels or ridges, formed during epitaxy on non-planar substrates under certain growth conditions. In particular, the growth of AlGaAs cladding layers on a (100) GaAs substrate patterned with [011]-oriented V-grooves leads to the formation of a very sharp corner between two {111} crystal planes. The active GaAs quantum well, on the other hand, grows faster along the [100] direction, which results in the formation of a crescent-shaped QW at the bottom of the groove shown in Fig. 5.1(a). The lateral tapering of the QW crescent provides lateral variation in the effective band gap due to the increase in the carrier confinement energy with decreasing QW thickness. This lateral

variation, in turn, results in a 2D potential well which confines the electrons and holes to a quasi-1D quantum wire (Fig. 5.1(b)).

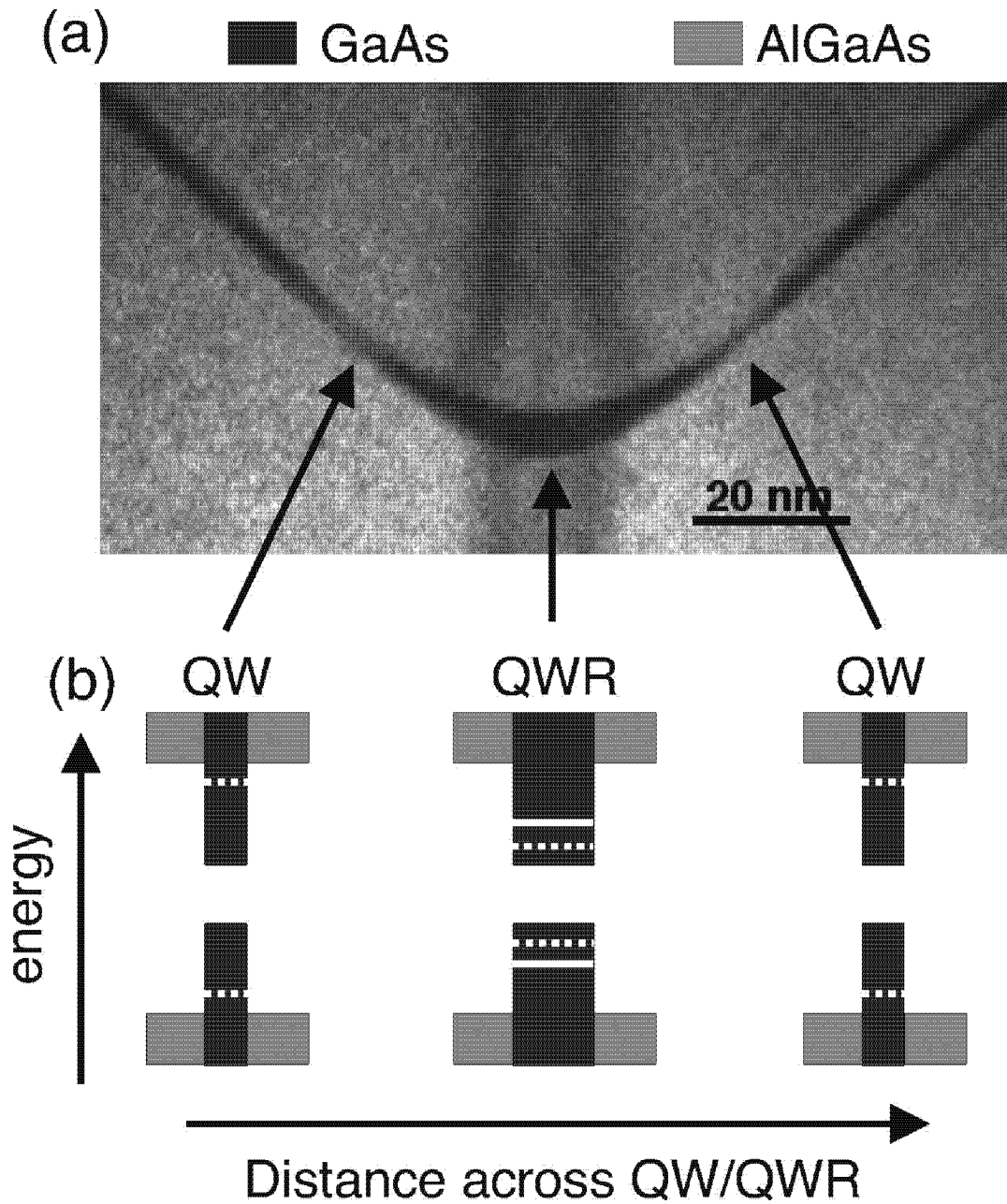


Fig. 5.1 (a) Transmission electron micrograph (TEM) cross section of a GaAs/AlGaAs quantum wire heterostructure. (b) Energy diagram vs. distance across the QW/QWR showing the band gap of the AlGaAs barriers (dark gray) and the GaAs QW/QWR (light gray). The dashed and the solid white lines schematically indicate the ground state of the QW and the QWR, respectively.

The investigated sample consists of a 0.5 μm pitch lateral array of single V-groove GaAs/ $\text{Al}_x\text{Ga}_{1-x}\text{As}$ ($x=0.33$) QWRs. Fig. 5.2(a) shows a schematic picture of the sample before any further processing. One can see the GaAs substrate, the AlGaAs energy barriers and, between the barriers, the GaAs quantum well with the QWR at the bottom of the V-groove. The nominal GaAs epilayer thickness is 1.7 nm, resulting in a QWR thickness of 4.2 nm. To prepare the sample for the NSOM measurements, it was mounted upside down on a glass disk and the GaAs substrate was removed by selective wet etching (see section 2.5). The etching leaves a 35 nm thick $\text{Al}_x\text{Ga}_{1-x}\text{As}$ barrier layer on top of the QWRs, as shown in Fig. 5.2(b). The thickness of this layer was chosen to ensure both QWR energy confinement and good spatial resolution in NSOM measurements. The high quality of the etching process becomes obvious from Fig. 5.2(c), where the topography of the sample after etching is shown, measured with an atomic force microscope (AFM). Further sample characterization was performed with photoluminescence (PL) measurements. At 20 K, the sample shows the QWR PL peak at 1.675 eV with a full width at half maximum (FWHM) of 14 meV. From these PL measurements and PL excitation spectra, we estimate that the lowest exciton has a transition energy of 1.59-1.60 eV at room temperature.

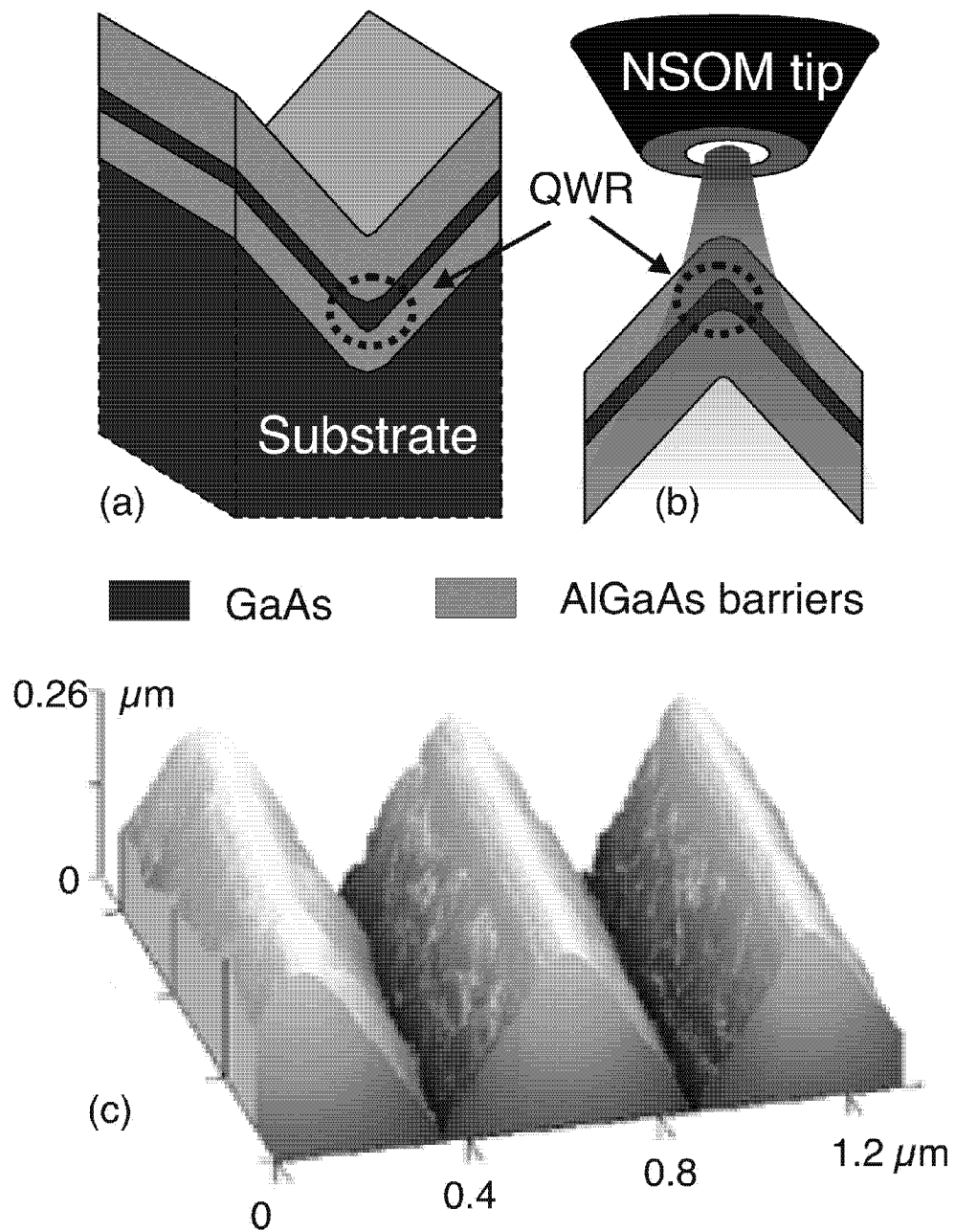


Fig. 5.2 Schematic diagrams of the QWR sample (a) before and (b) after etching with its orientation regarding the NSOM tip. (c) A two-dimensional AFM image of the topography of the QWR sample after etching.

5.2 Experimental results

5.2.1 Spatially resolved QWRs

In a first experiment, the pump pulse with center photon energy 1.58 eV is transmitted through the NSOM tip to excite the QWRs locally. The pump-induced changes of the reflected probe pulse intensity are globally measured in the far-field (see inset of Fig. 5.3). The excited carrier density was calculated to be about 10^5 cm^{-1} . Fig. 5.3 shows a two-dimensional image of the amplitude of the pump-probe signal at zero time delay. The quantum wires, separated by a distance of $0.5 \mu\text{m}$, are well discernable, proving high spatial resolution. Along a single wire, intensity variations of the pump-probe signal indicate fluctuations of the energy or the oscillator strength of the QWR excitonic resonance.

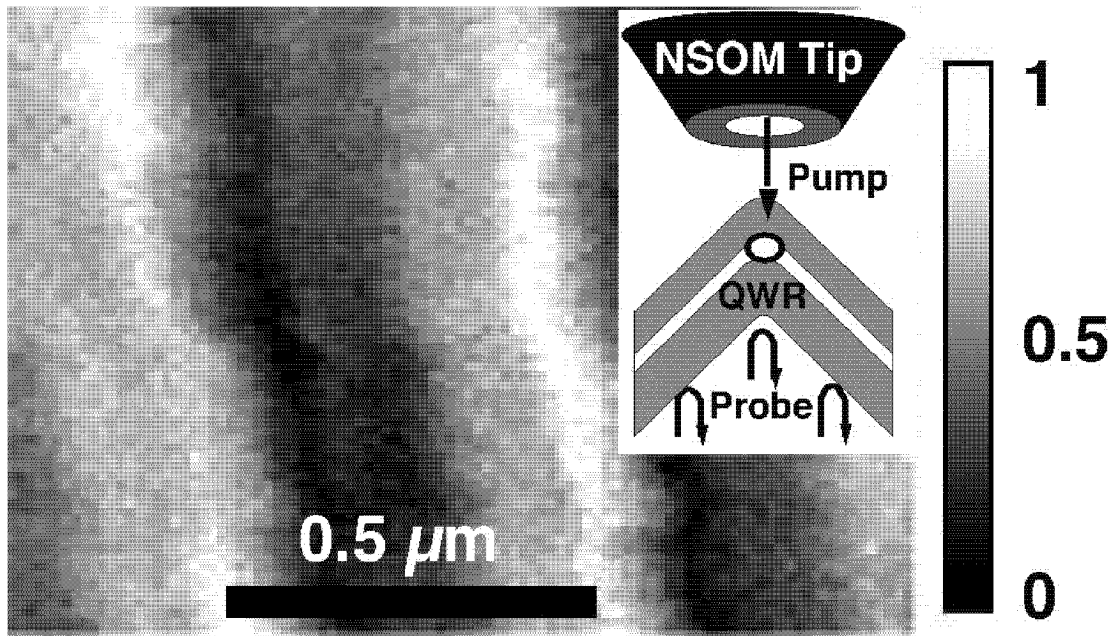


Fig. 5.3 Two-dimensional image of the pump-probe amplitude at zero time delay. The bending of the wires in the center of the image is due to scanner drift. Inset: Schematic of the back-etched V-groove QWR sample (gray: AlGaAs; white: GaAs) and the experimental configuration

Fig. 5.4 shows a line scan perpendicular to the QWRs. Between the QWRs the pump-probe signal disappears completely, proving that high spatial resolution

and strong contrast is obtained with the applied method. In contrast, if one measures the transmitted pump intensity, one finds that its modulation is only a few percent. This means that the coupling of the near-field pump and the sample changes only slightly across the sample. Therefore, the topographical artifacts [71] give negligible contribution to the nonlinear probe modulation shown in Fig. 5.4. Especially, if we scan along a single QWR, the topographical artifacts will be even more strongly reduced in comparison to a scan perpendicular to the QWRs. Thus, nonlinear optical near-field spectroscopy lends itself well to the characterization of these QWR samples.

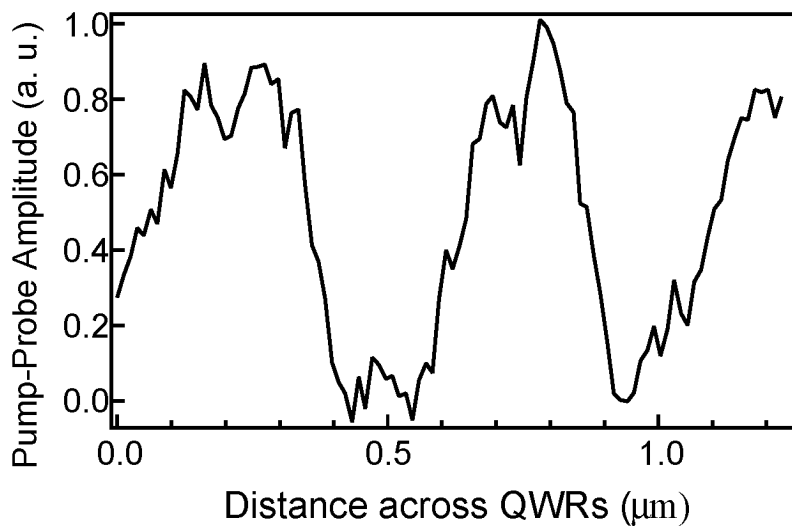


Fig. 5.4 Line scan of the pump-probe amplitude perpendicular to the quantum wires.

5.2.2 Single QWR carrier dynamics

The fluctuations in quantization energy along a single QWR are determined from measurements in the standard femtosecond NSOM configuration with a global pump and a local probe. The aperture of the NSOM tip is ~ 200 nm in these measurements. For resonant excitation of a QWR, the measured differential transmission is mainly due to pump-induced absorption changes and its decay reflects the carrier dynamics in the QWR [23]. Fig. 5.5 shows near-field pump-probe traces for different laser photon energies around the lowest exciton resonance. The traces are taken at a fixed position on a single wire. The measurements are performed with constant laser excitation power, resulting in

a carrier density of $2 \times 10^6 \text{ cm}^{-1}$ for resonant excitation of the exciton. For all photon energies, a positive bleaching signal is observed at early times due to excitonic phase space filling and screening. The bleaching signals show a fast initial decay with a time constant of 300-400 fs. We attribute this decay to exciton ionization by LO phonons which reduces the phase space filling contribution to the pump-probe signal [83].

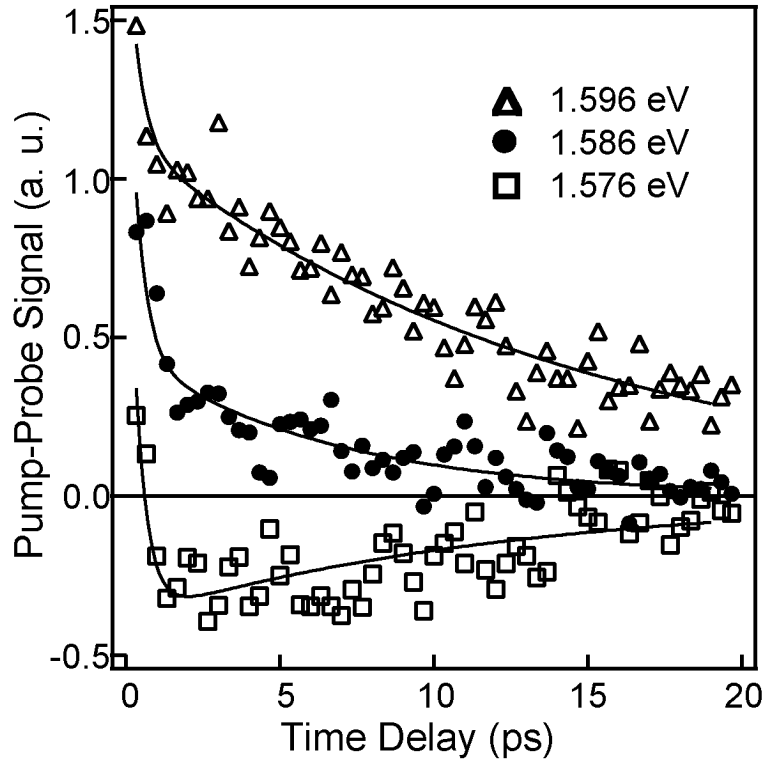


Fig. 5.5 Near-field pump-probe traces taken at the same position of the QWR but at various photon energies around the lowest exciton resonance.

After the initial fast decay, the pump-probe traces sensitively depend on the laser photon energy. At higher photon energies close to the exciton resonance, the non-linear signal is positive indicating a bleaching process. In contrast, at photon energies well below the exciton resonance, the signal becomes negative demonstrating induced absorption. We attribute the induced absorption to pump-induced broadening of the exciton resonance. Fig. 5.6 schematically shows the broadening of an absorption resonance due to excited carriers, resulting in an increase of the absorption on the low-energy side.

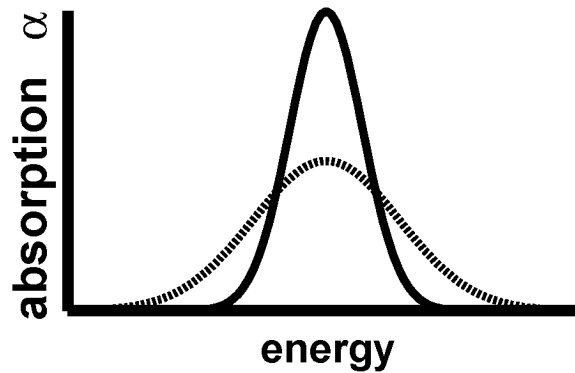


Fig. 5.6 A schematic picture showing an absorption resonance α before excitation (full line) and the broadened resonance after pump excitation (broken line).

For all photon energies, the pump-probe signal approaches zero with a second time constant of 10-12 ps. Since radiative recombination occurs on a much longer time scale [113], the slow decay is due to non-radiative processes, such as fast carrier trapping by activated interface impurities [114].

5.2.3 QWR quantization energy fluctuations

In order to quantify the dependence on detuning, we have fitted the pump-probe traces to double exponential functions $(\Delta T/T)_{fast} \exp(-\Delta t/\tau_{fast}) + (\Delta T/T)_{slow} \exp(-\Delta t/\tau_{slow})$. In Fig. 5.6, we show the extracted amplitude $(\Delta T/T)_{slow}$ of the slowly decaying contribution of a set of pump-probe traces versus laser photon energy. The measurements are performed at a fixed position on the QWR, i.e. for a fixed exciton resonance energy E_x ⁶.

⁶ The data of Fig. 5.5 and Fig. 5.7 have been taken at different positions. This explains why the amplitude at 1.586 eV is positive in Fig. 5.5 but negative in Fig. 5.7.

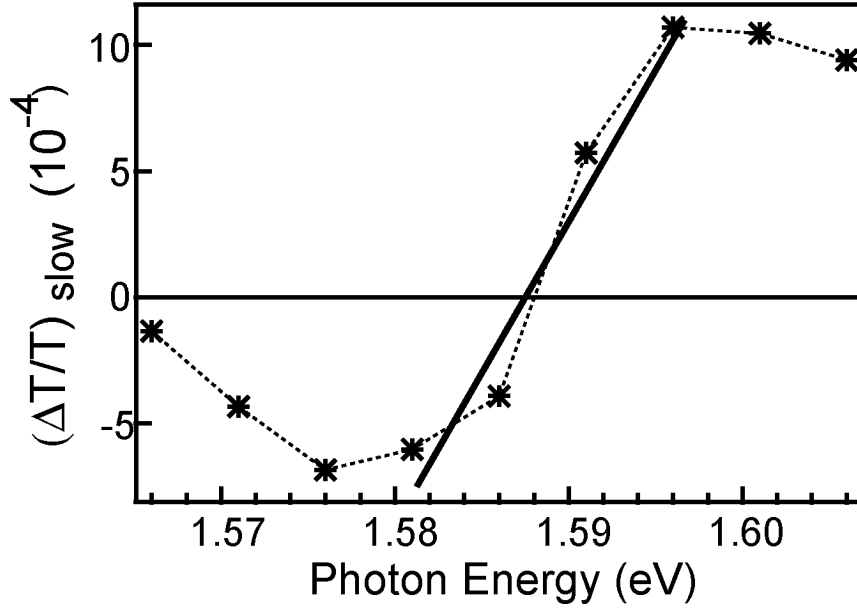


Fig. 5.7 The amplitude $(\Delta T/T)_{slow}$ of the slowly decaying contribution of near-field pump-probe traces versus the photon energy for a fixed QWR position. The full line indicated the slope used to calculate the variations in quantization energy.

In a photon energy region around the zero-crossing of the amplitude $(\Delta T/T)_{slow}$, the shape of the pump-probe signal is very sensitive to the photon energy. In this region we obtain, in a first approximation, a linear relation between the amplitude and the detuning between the laser photon energy $\hbar\omega$ and E_x with the following slope (the full line in Fig. 5.6):

$$\frac{\Delta[(\Delta T/T)_{slow}]}{\Delta[\hbar\omega - E_x]} = 1.2 * 10^{-4} \text{ meV}^{-1} \tag{5.3}$$

From this slope, one can calculate the variation of the energy detuning for a given change of the amplitude. Equation 5.3 is valid for a certain excitation power. If this excitation power is used, Eq. 5.3 allows for the mapping of quantization energy fluctuations along a single quantum wire. This will be discussed in the following.

If the NSOM tip is scanned along a QWR for a fixed laser photon energy, the detuning between the photon energy $\hbar\omega$ and the exciton resonance energy E_x may change due to fluctuations of the exciton quantization energy. In turn, the change of the detuning will substantially change the shape of the pump-probe

traces. This effect is illustrated in Fig. 5.8(a) and Fig. 5.8(b), which show pump-probe traces taken at two different positions for a fixed laser photon energy $\hbar\omega = 1.578$ eV. For the quantitative determination of the exciton energy fluctuations, the change of the amplitude $\left(\frac{\Delta T}{T}\right)_{slow}$ is considered. Fig. 5.8(c) shows $\left(\frac{\Delta T}{T}\right)_{slow}$ versus position along a single QWR for the fixed photon energy 1.578 eV. The values of $\left(\frac{\Delta T}{T}\right)_{slow}$ are calculated from pump-probe traces taken every 200 nm along a single QWR with an NSOM tip providing a spatial resolution of ~ 200 nm. As expected, $\left(\frac{\Delta T}{T}\right)_{slow}$ varies with position. We like to emphasize that the variation of $\left(\frac{\Delta T}{T}\right)_{slow}$ in Fig. 5.8(c) is due to detuning variations that result from the fluctuation of the exciton resonance energy since the photon energy is constant.

The fixed photon energy of 1.578 eV is chosen to give the smallest amplitude $\left(\frac{\Delta T}{T}\right)_{slow}$ at the start position of the scan. This ensures that Eq. 5.3 is valid. Using Eq. 5.3, we can calculate the change of the detuning between photon energy and exciton resonance energy from the variation of $\left(\frac{\Delta T}{T}\right)_{slow}$. Following this procedure, the right vertical axis of Fig. 5.8(c) has been obtained. From this axis, it can be determined how the energy detuning changes with position along a single quantum wire. The change of the energy detuning is equal to the change of the exciton quantization energy. We note that an increase (decrease) of $\left(\frac{\Delta T}{T}\right)_{slow}$ reflects a red shift (blue shift) of the excitonic resonance and, therefore, a smaller (larger) quantization energy.

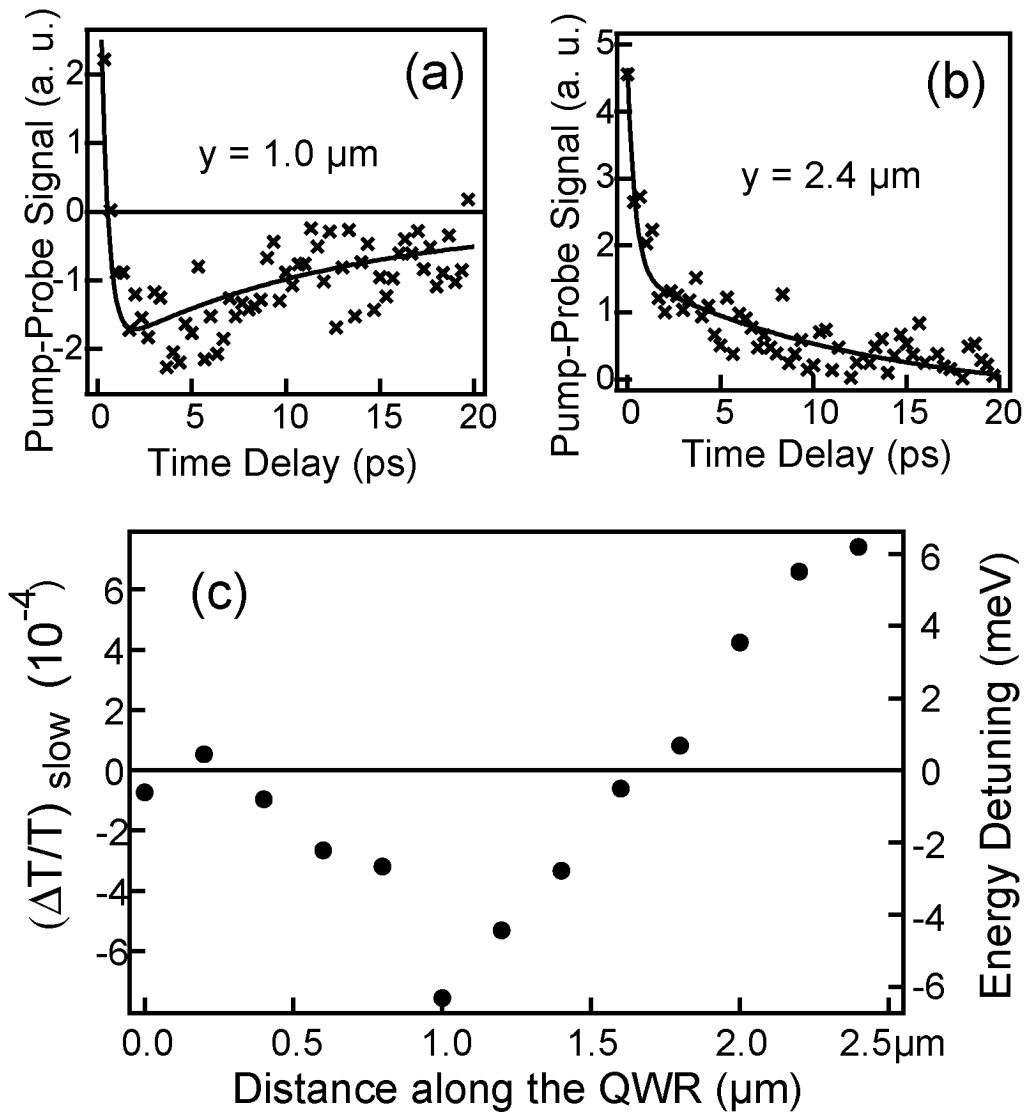


Fig. 5.8 Pump-probe traces (a) and (b) for two different positions y of a single quantum wire for a fixed laser photon energy of 1.578 eV. (c) The amplitude $(\Delta T/T)_{\text{slow}}$ of the slowly decaying contribution of near-field pump-probe traces versus position along a single QWR at the fixed laser photon energy of 1.578 eV. The right-hand vertical axis shows the calculated energy detuning variation along the wire.

Energy variations of 12 meV are observed over 2 μm wire length. Such energy variations are often deduced from the inhomogeneous broadening of spatially integrated PL spectra. At low temperatures, the FWHM of the QWR PL peak is 14 meV, directly giving the inhomogeneous broadening. From the comparison to the measured quantization energy fluctuations of 12 meV, we conclude that the inhomogeneous broadening mainly arises from energy fluctuations along

the wires. The quantization energy fluctuations result from variations of the wire thickness. Considering the first electron - heavy hole transition in a simple finite potential model for the V-groove QWRs, the energy variation of 12 meV corresponds to a wire thickness fluctuation of about 3 Å or 1 monolayer of GaAs. It is noteworthy that energy fluctuations of less than 12 meV are resolved in Fig. 5.8(c). These fluctuations correspond to thickness variations of less than one monolayer, showing that monolayer fluctuations are averaged over the NSOM tip diameter. Therefore, the monolayer fluctuations have to occur on a length scale smaller than the tip diameter.

5.3 V-groove QWR summary

We have demonstrated that the femtosecond NSOM technique can be used to study carrier dynamics in a single semiconductor quantum wire. Moreover, we have presented an experimental method for the mapping of energy fluctuations along a single quantum wire with high spatial resolution. With this method, quantitative information is obtained on the magnitude of quantum wire thickness fluctuations and on the length scale over which these fluctuations occur. These results demonstrate the potential of femtosecond NSOM for the characterization of nanostructured materials.

6 Conclusion and outlook

In this theses, we have shown that femtosecond spectroscopy with a spatial resolution beyond the diffraction limit can be performed if scanning near-field optical microscopy is combined with ultrafast pump-probe techniques. Today, the spatial and temporal resolution simultaneously achieved in near-field pump-probe measurements is on the order of 100 nm and 100 fs, respectively. Moreover, the results presented in this work show that, with a well-engineered femtosecond NSOM instrument, a high sensitivity below 1×10^{-4} can be obtained in near-field pump-probe measurements, even in a degenerate configuration. For the future, the whole near-field optics field will increasingly gain of importance in microscopy⁷. In particular, further progress can be expected due to the recent development of high-throughput, small-aperture NSOM fiber probes [115, 116]. These NSOM probes should allow one to push the spatial resolution without sacrificing sensitivity. Moreover, the time resolution can also be improved building on the recent progress in femtosecond technology [117].

Already today, the combination of high spatial and temporal resolution and high sensitivity achieved in femtosecond NSOM provides considerable insight into the spatiotemporal evolution of physical quantities. In fact, the ultrafast NSOM is the leading instrument among the ultrafast SPM techniques, as the ultrafast AFM and STM are still in the proof of principle stage. Current results in ultrafast STM [118-120] show a spatio-temporal resolution as small as 1 nm-20 ps [120], whereas measurements with ultrafast AFMs present a high temporal resolution of ~2 ps without indicating data on the spatial resolution [121, 122]. However, with both the ultrafast STM and AFM no measurements beyond the determination of spatial or temporal resolution have been realized so far.

Typical femtosecond NSOM measurements can be placed in two categories: studies of single nanostructures and transport studies. As an example for the

⁷ A good overview of the present research activities in near-field optics can be found in the proceedings of the NFO-6 conference, which has been held at the University of Twente, the Netherlands, in August 2000. The proceedings are published by Blackwell Science in the Journal of Microscopy, Vol. 202, April 2001,

former, we have discussed femtosecond NSOM experiments on single semiconductor quantum wires. These measurements yield information on the carrier relaxation in a single QWR and on the fluctuations of the quantization energy and the wire thickness along a single QWR. In general, the characterization of nanostructured and low-dimensional materials is an important application of the femtosecond NSOM technique.

As examples for transport studies, we have presented experiments on laterally patterned semiconductor quantum wells and on a metal-semiconductor composite material. The latter consists of nano-scale tungsten disks embedded in GaAs. In the patterned quantum well samples, the details of carrier diffusion in square-like carrier density profiles have been observed. Carrier transport in the tungsten disk material has been found to involve both carrier drift and carrier diffusion.

While carrier drift and diffusion have been studied by several groups [17, 19, 20, 22, 25, 26], ballistic transport phenomena have not yet been observed in femtosecond NSOM experiments. For semiconductors, ballistic transport in optical near-field experiments has been treated in detail theoretically [123-126]. Experimental studies of ballistic transport are a wide field for future femtosecond NSOM work.

Exciting future nanomaterials for characterization as well as transport femtosecond NSOM studies include not only low-dimensional single structures but also combined systems, such as semiconductor wire-dot structures [127, 128] or polymer-nanocrystal composite materials [129, 130], which may play an important role in future optoelectronic applications. In such combined systems the femtosecond NSOM allows for the investigation of spatially and temporally resolved carrier transport from one to the other system, interface dynamics, such as carrier and energy transfer, and carrier or energy relaxation dynamics.

References

- [1] M. Chergui, *Femtochemistry* (World Scientific, Singapore, 1996)
- [2] J. Shah, *Ultrafast spectroscopy of semiconductors and semiconductor nanostructures* (Springer-Verlag, Berlin, 1999)
- [3] R. W. Schoenlein, W. Z. Lin, J. G. Fujimoto, G. L. Eesley, "Femtosecond studies of nonequilibrium electronic processes in metals," *Phys. Rev. Lett.* **58**, 1680 (1987).
- [4] H. E. Elsayed–Ali, T. B. Norris, M. A. Pessot, G. A. Mourou, "Time-resolved observation of electron-phonon relaxation in copper," *Phys. Rev. Lett.* **58**, 1212 (1987).
- [5] E. Kapon, in *Optical Spectroscopy of Low-Dimensional Semiconductors* G. A. e. al., Eds. (Kluwer Academic, Amsterdam, 1997) 99.
- [6] G. Binnig, H. Rohrer, C. Gerber, E. Weibel, "Surface Studies by Scanning Tunneling Microscopy," *Phys. Rev. Lett.* **49**, 57 (1982).
- [7] G. Binnig, C. F. Quate, C. Gerber, "Atomic force microscope," *Phys. Rev. Lett.* **56**, 930 (1986).
- [8] D. W. Pohl, W. Denk, M. Lanz, "Optical stethoscopy: image recording with resolution $\lambda/20$," *Appl. Phys. Lett.* **44**, 651 (1984).
- [9] A. Lewis, M. Isaacson, A. Harootunian, A. Muray, "Development of a 500-Å spatial-resolution light-microscope," *Ultramicroscopy* **13**, 227 (1984).
- [10] E. Betzig, J. K. Trautman, "Near-Field Optics: Microscopy, Spectroscopy, and Surface Modification Beyond the Diffraction Limit," *Science* **257**, 189 (1992).
- [11] A. S. Hou, F. Ho, D. M. Bloom, "Picosecond electrical sampling using a scanning force microscope," *Electr. Lett.* **28**, 2302 (1992).
- [12] G. Nunes, M. R. Freeman, "Picosecond resolution in scanning tunneling microscopy," *Science* **262**, 1029 (1993).
- [13] S. Weiss, D. F. Ogletree, D. Botkin, M. Salmeron, D. S. Chemla, "Ultrafast scanning probe microscopy," *Appl. Phys. Lett.* **63**, 2567 (1993).
- [14] K. Takeuchi, Y. Kasahara, "High-speed optical sampling measurement of electrical wave form using a scanning tunneling microscope," *Appl. Phys. Lett.* **63**, 3548 (1993).
- [15] J. B. Stark, U. Mohideen, E. Betzig, R. E. Slusher, in *Ultrafast Phenomena IX* P. F. Barbara, W. H. Knox, G. A. Mourou, A. H. Zewail, Eds. (Springer, Heidelberg, 1994)
- [16] S. Smith, B. G. Orr, R. Kopelman, T. Norris, "100 femtosecond / 100 nanometer near-field probe," *Ultramicroscopy* **57**, 173 (1995).

-
- [17] J. Levy, V. Nikitin, J. M. Kikkawa, A. Cohen, N. Samarth, R. Garcia, D. D. Awschalom, "Spatiotemporal near-field spin microscopy in patterned magnetic heterostructures," *Phys. Rev. Lett.* **76**, 1948 (1996).
- [18] A. Vertikov, M. Kuball, A. V. Nurmikko, H. J. Maris, "Time-resolved pump-probe experiments with subwavelength lateral resolution," *Appl. Phys. Lett.* **69**, 2465 (1996).
- [19] S. Smith, N. C. R. Holme, B. Orr, R. Kopelman, T. Norris, "Ultrafast measurement in GaAs thin films using NSOM," *Ultramicroscopy* **71**, 213 (1998).
- [20] B. A. Nechay, U. Siegner, F. Morier-Genoud, A. Schertel, U. Keller, "Femtosecond near-field optical spectroscopy of implantation patterned semiconductors," *Appl. Phys. Lett.* **74**, 61 (1999).
- [21] B. A. Nechay, U. Siegner, M. Achermann, H. Bielefeldt, U. Keller, "Femtosecond pump-probe near-field optical microscopy," *Rev. of Sci. Instr.* **70**, 2758 (1999).
- [22] M. Achermann, B. A. Nechay, F. Morier-Genoud, A. Schertel, U. Siegner, U. Keller, "Direct experimental observation of different diffusive transport regimes in semiconductor nanostructures," *Phys. Rev. B* **60**, 2101 (1999).
- [23] T. Guenther, V. Emiliani, F. Intonti, C. Lienau, T. Elsaesser, R. Nötzel, K. H. Ploog, "Femtosecond near-field spectroscopy of single GaAs quantum wire," *Appl. Phys. Lett.* **75**, 3500 (1999).
- [24] M. Achermann, B. A. Nechay, U. Siegner, A. Hartmann, D. Oberli, E. Kapon, U. Keller, "Quantization energy mapping of single V-groove GaAs quantum wires by femtosecond near-field optics," *Appl. Phys. Lett.* **76**, (2000).
- [25] M. Achermann, U. Siegner, L. E. Wernersson, U. Keller, "Ultrafast carrier dynamics around nanoscale Schottky contacts studied by femtosecond far- and near-field optics," *Appl. Phys. Lett.* **77**, 3370 (2000).
- [26] V. Emiliani, T. Guenther, C. Lienau, R. Nötzel, K. H. Ploog, "Ultrafast near-field spectroscopy of quasi-one-dimensional transport in a single quantum wire," *Phys. Rev. B* **61**, R10583 (2000).
- [27] Y. Toda, T. Sugimoto, M. Nishioka, Y. Arakawa, "Near-field coherent excitation spectroscopy of InGaAs/GaAs self-assembled quantum dots," *Appl. Phys. Lett.* **76**, 3887 (2000).
- [28] H. Kawashima, M. Furuki, S. Tatsuura, M. Tian, Y. Sato, L. S. Pu, T. Tani, "Optical gate action of a molecular thin film probed with femtosecond near-field optical microscopy," *Appl. Phys. Lett.* **77**, 1283 (2000).
- [29] B. Hecht, B. Sick, U. P. Wild, V. Deckert, R. Zenobi, O. J. F. Martin, D. W. Pohl, "Scanning near-field optical microscopy with aperture probes: Fundamentals and applications," *J. Chem. Phys.* **112**, 7761 (2000).
- [30] J. A. Veerman, M. F. Garcia-Parajo, L. Kuipers, N. F. v. Hulst, "Time-varying triplet state lifetimes of single molecules," *Phys. Rev. Lett.* **83**, 2155 (1999).
- [31] H. Gersen, M. F. Garcia-Parajo, L. Novotny, J. A. Veermann, L. Kuipers, N. F. v. Hulst, "Influencing the angular emission of a single molecule," *Phys. Rev. Lett.* **85**, 5312 (2000).

- [32] B. Sick, B. Hecht, L. Novotny, "Orientational imaging of single molecules by annular illumination," *Phys. Rev. Lett.* **85**, 4482 (2000).
- [33] Y. Toda, O. Moriwaki, M. Nishioka, Y. Arakawa, "Efficient carrier relaxation mechanism in InGaAs/GaAs self-assembled quantum dots based on the existence of continuum states," *Phys. Rev. Lett.* **82**, 4114 (1999).
- [34] O. Mauritz, G. Goldoni, F. Rossi, E. Molinari, "Local optical spectroscopy in quantum confined systems: A theoretical description," *Phys. Rev. Lett.* **82**, 847 (1999).
- [35] F. Intonti, V. Emiliani, C. Lienau, T. Elsaesser, V. Savona, E. Runge, R. Zimmermann, R. Nötzel, K. H. Ploog, "Quantum mechanical repulsion of exciton levels in a disordered quantum well," *Phys. Rev. Lett.* **87**, 076801 (2001).
- [36] M. L. M. Balistreri, J. P. Korterik, L. Kuipers, N. F. v. Hulst, "Local observations of phase singularities in optical fields in waveguide structures," *Phys. Rev. Lett.* **85**, 294 (2000).
- [37] S. I. Bozhevolnyi, J. Erland, K. Leosson, P. M. W. Skovgaard, J. M. Hvam, "Waveguiding in surface plasmon polariton band gap structures," *Phys. Rev. Lett.* **86**, 3008 (2001).
- [38] J. R. Krenn, A. Dereux, J. C. Weeber, E. Bourillot, Y. Lacroute, J. P. Goudonnet, G. Schider, W. Gotschy, A. Leitner, F. R. Aussenegg, C. Girard, "Squeezing the optical near-field zone by plasmon coupling of metallic nanoparticles," *Phys. Rev. Lett.* **82**, 2590 (1999).
- [39] S. Gresillon, L. Aigouy, A. C. Boccara, J. C. Rivoal, X. Quelin, C. Desmarest, P. Gadenne, V. A. Shubin, A. K. Sarychev, V. M. Shalaev, "Experimental observation of localized optical excitations in random metal-dielectric films," *Phys. Rev. Lett.* **82**, 4520 (1999).
- [40] R. Carminati, J. J. Greffet, "Near-field effects in spatial coherence of thermal sources," *Phys. Rev. Lett.* **82**, 1660 (1999).
- [41] R. Carminati, J. J. Saenz, "Scattering theory of Bardeen's formalism for tunneling: New approach to near-field microscopy," *Phys. Rev. Lett.* **84**, 5156 (2000).
- [42] P. S. Carney, V. A. Markel, J. C. Schotland, "Near-field tomography without phase retrieval," *Phys. Rev. Lett.* **86**, 5874 (2001).
- [43] L. Salomon, F. Grillot, A. V. Zayats, F. d. Fornel, "Near-field distribution of optical transmission of periodic subwavelength holes in a metal film," *Phys. Rev. Lett.* **86**, 1110 (2001).
- [44] E. Abbe, "Beiträge zur Theorie des Mikroskops und der mikroskopischen Wahrnehmung," *Archiv. f. Mikroskop.* **9**, 413 (1873).
- [45] E. H. Syngé, "A suggested method for extending microscopic resolution into the ultra-microscopic region," *Philos. Mag.* **6**, 356 (1928).
- [46] F. Zenhausern, Y. Martin, H. K. Wickramasinghe, "Scanning interferometric apertureless microscopy - Optical imaging at 10 Angstrom resolution," *Science* **269**, 1083 (1995).

-
- [47] B. Knoll, F. Keilmann, "Near-field probing of vibrational absorption for chemical microscopy," *Nature* **399**, 134 (1999).
- [48] E. J. Sanchez, L. Novotny, X. S. Xie, "Near-field fluorescence microscopy based on two photon excitation with metal tips," *Phys. Rev. Lett.* **82**, 4014 (1999).
- [49] R. Hillebrand, F. Keilmann, "Complex optical constants on a subwavelength scale," *Phys. Rev. Lett.* **85**, 3029 (2000).
- [50] H. A. Bethe, "Theory of diffraction by small holes," *Phys. Rev.* **66**, 163 (1944).
- [51] C. J. Bouwkamp, "On Bethe's theory of diffraction by small holes," *Philips Res. Rep.* **5**, 321 (1950).
- [52] A. H. Rosa, B. I. Yakobson, H. D. Hallen, "Origins and effects of thermal processes on near-field optical probes," *Appl. Phys. Lett.* **67**, 2597 (1995).
- [53] M. Stähelin, M. A. Bopp, G. Tarrach, A. J. Meixner, I. Zschokke-Gränacher, "Temperature profile of fiber tips used in scanning near-field optical microscopy," *Appl. Phys. Lett.* **68**, 2603 (1996).
- [54] E. Betzig, J. K. Trautman, T. D. Harris, J. S. Weiner, R. L. Kostelak, "Breaking the diffraction barrier: Optical microscopy on a nanometric scale," *Science* **251**, 1468 (1991).
- [55] S. Jiang, H. Ohsawa, K. Yamada, T. Pangaribuan, M. Ohtsu, K. Imai, A. Ikai, "Nanometric scale biosample observation using a photon scanning tunneling microscope," *Jpn. J. Appl. Phys.* **31**, 2282 (1992).
- [56] R. Stöckle, C. Fokas, V. Deckert, R. Zenobi, B. Sick, B. Hecht, U. P. Wild, "High-quality near-field optical probes by tube etching," *Appl. Phys. Lett.* **75**, 160 (1999).
- [57] P. Lambelet, A. Sayah, M. Pfeffer, C. Philipona, F. Marquis-Weible, "Chemically etched fiber tips for near-field optical microscopy: a process for smoother tips," *Appl. Optics* **37**, 7289 (1998).
- [58] R. M. Stöckle, N. Schaller, V. Deckert, C. Fokas, R. Zenobi, "Brighter near-field optical probes by means of improving the optical destruction threshold," *J. Microsc.* **194**, 378 (1999).
- [59] E. Betzig, P. L. Finn, J. S. Weiner, "Combined shear force and near-field scanning optical microscopy," *Appl. Phys. Lett.* **60**, 2484 (1992).
- [60] K. Karrai, R. D. Grober, "Piezoelectric tip-sample distance control for near field optical microscopes," *Appl. Phys. Lett.* **66**, 1842 (1995).
- [61] M. A. Paesler, P. J. Moyer, *Near-Field Optics: Theory, Instrumentation, and Applications* (John Wiley & Sons, Inc., New York, 1996)
- [62] U. Siegner, U. Keller, in *Handbook of Optics* M. Bass, E. W. Stryland, D. R. Williams, W. L. Wolfe, Eds. (McGRAW-HILL, INC., New York, 2000), **Vol. III**,
- [63] P. C. Becker, H. L. Fragnito, C. H. Brito Cruz, R. L. Fork, J. E. Cunningham, J. E. Henry, C. V. Shank, "Femtosecond photon echoes from band-to-band transitions in GaAs," *Physical Review Letters* **61**, 1647 (1988).

- [64] S. Arlt, U. Siegner, J. Kunde, F. Morier-Genoud, U. Keller, "Ultrafast dephasing of continuum transitions in bulk semiconductors," *Physical Review B* **59**, 14860 (1999).
- [65] W. H. Knox, C. Hirlimann, D. A. B. Miller, J. Shah, D. S. Chemla, C. V. Shank, "Femtosecond excitation of nonthermal carrier populations in GaAs quantum wells," *Physical Review Letters* **56**, 1191 (1986).
- [66] S. Hunsche, H. Heesel, A. Ewertz, H. Kurz, J. H. Collet, "Spectral-hole burning and carrier thermalization in GaAs at room temperature," *Phys. Rev. B* **48**, 17818 (1993).
- [67] F. J. Duarte, J. A. Piper, "Dispersion Theory of Multiple-Prism Beam Expanders for Pulsed Dye Lasers," *Optics Communications* **43**, 303 (1982).
- [68] G. P. Agrawal, *Nonlinear Fiber Optics* (Academic Press, Inc., 1989)
- [69] A. Lewis, U. Ben-Ami, N. Kuck, G. Fish, D. Diamant, L. Lubovsky, K. Lieberman, S. Katz, A. Saar, M. Roth, "NSOM the Fourth Dimension: Integrating Nanometric Spatial and Femtosecond Time Resolution," *Scanning* **17**, 3 (1995).
- [70] R. Müller, C. Lienau, "Propagation of femtosecond optical pulses through uncoated and metal-coated near-field probes," *Appl. Phys. Lett.* **76**, 3367 (2000).
- [71] B. Hecht, H. Bielefeldt, Y. Inouye, D. W. Pohl, "Facts and Artifacts in Near-Field Optical Microscopy," *J. Appl. Phys.* **81**, 2492 (1997).
- [72] R. A. Logan, F. K. Reinhart, "Optical waveguides in GaAs-AlGaAs epitaxial layers," *J. Appl. Phys.* **44**, 4172 (1973).
- [73] J. J. LePore, "An improved technique for selective etching of GaAs and Ga(1-x)Al(x)As," *J. Appl. Phys.* **51** (12), 6441 (1980).
- [74] K. Kenefick, "Selective etching characteristics fo peroxide/ammonium-hydroxide solutions for GaAs/Al_{0.16}Ga_{0.84}As," *J. Electrochem. Soc* **129**, 2380 (1982).
- [75] J. F. Ziegler, J. P. Biersack, U. Littmark, *The Stopping and Range of Ions in Solids* (Pergamon, New York, 1989), vol. 1.
- [76] M. Lambsdorff, J. Kuhl, J. Rosenzweig, A. Axmann, J. Schneider, "Subpicosecond carrier lifetimes in radiation-damaged GaAs," *Appl. Phys. Lett.* **58**, 1881 (1991).
- [77] M. J. Lederer, B. Luther-Davies, H. H. Tan, C. Jagadish, M. Haiml, U. Siegner, U. Keller, "Nonlinear optical absorption and temporal response of Arsenic- and Oxygen-implanted GaAs," *Appl. Phys. Lett.* **74**, 1993 (1999).
- [78] Y. Silverberg, P. W. Smith, D. A. B. Miller, B. Tell, A. C. Gossard, W. Wiegmann, "Fast nonlinear optical response from proton-bombarded multiple quantum well structures," *Appl. Phys. Lett.* **46**, 701 (1985).
- [79] W. Walukiewicz, Z. Liliental-Weber, J. Jasinski, M. Almonte, A. Prasad, E. E. Haller, E. R. Weber, P. Grenier, J. F. Whitaker, "High resistivity and ultrafast carrier lifetime in argon implanted GaAs," *Appl. Phys. Lett.* **69**, 2569 (1996).
- [80] P. Omling, P. Silverberg, L. Samuelson, "Identification of a second energy level in n-type GaAs," *Phys. Rev. B* **38**, 3606 (1988).

-
- [81] G. L. Witt, "LTMBE GaAs: present status and perspectives," *Mater. Sci. Eng.* **B22**, 9 (1993).
- [82] P. G. Piva, P. J. Poole, M. Buchanan, G. Champion, I. Templeton, G. C. Aers, R. Williams, Z. R. Wasilewski, E. S. Koteles, S. Charbonneau, "Enhanced compositional disordering of quantum wells in GaAs/AlGaAs and InGaAs/GaAs using focused Ga⁺ ion beams," *Appl. Phys. Lett.* **65**, 621 (1994).
- [83] W. H. Knox, R. L. Fork, M. C. Downer, D. A. B. Miller, D. S. Chemla, C. V. Shank, A. C. Gossard, W. Wiegmann, "Femtosecond dynamics of resonantly excited excitons in room-temperature GaAs quantum wells," *Phys. Rev. Lett.* **54**, 1306 (1985).
- [84] A. Olsson, D. J. Erskine, Z. Y. Xu, A. Schremer, C. L. Tang, "Nonlinear luminescence and time-resolved diffusion profiles of photoexcited carriers in semiconductors," *Appl. Phys. Lett.* **41**, 659 (1982).
- [85] H. Hillmer, A. Forchel, C. W. Tu, "Enhancement of electron-hole pair mobilities in thin GaAs/AlGaAs quantum wells," *Phys. Rev. B* **45**, 1240 (1992).
- [86] Y. L. Lam, J. Singh, "Carrier thermalization by phonon absorption in quantum-well modulators and detectors," *IEEE J. Quantum Electron.* **31**, 923 (1995).
- [87] A. M. T. Kim, S. Hunsche, T. Dekorsy, H. Kurz, K. Köhler, "Time-resolved study of intervalence band thermalization in a GaAs quantum well," *Appl. Phys. Lett.* **68**, 2956 (1996).
- [88] H. J. Eichler, P. Guenter, D. W. Pohl, *Laser-induced dynamic gratings* (Springer-Verlag, Berlin, 1986)
- [89] T. Chang, H. Kim, H. Yu, "Spatial harmonic analysis of transient optical gratings," *Chem. Phys. Lett.* **111**, 64 (1984).
- [90] S. M. Sze, *Physics of Semiconductor Devices* (John Wiley & Sons, 1981)
- [91] U. Siegner, M. Achermann, U. Keller, "Spatially resolved femtosecond spectroscopy," *Mat. Sci. and Tech.* **12**, (2001).
- [92] L.-E. Wernersson, N. Carlsson, B. Gustafson, A. Litwin, L. Samuelson, "Lateral current-constriction in vertical devices using openings in buried lattices of metallic discs," *Appl. Phys. Lett.* **71**, 2803 (1997).
- [93] A. C. Warren, J. M. Woodall, J. L. Freeouf, D. Grischkowsky, M. R. Melloch, N. Otsuka, "Arsenic precipitates and the semi-insulating properties of GaAs buffer layers grown by low-temperature molecular beam epitaxy," *Appl. Phys. Lett.* **57**, 1331 (1990).
- [94] R. M. Feenstra, A. Vaterlaus, J. M. Woodal, G. D. Pettit, "Tunneling spectroscopy of midgap states induced by arsenic precipitates in low-temperature-grown GaAs," *Appl. Phys. Lett.* **63**, 2528 (1993).
- [95] M. Haiml, U. Siegner, F. Morier-Genoud, U. Keller, M. Luysberg, R. C. Lutz, P. Specht, E. R. Weber, "Optical nonlinearity in low-temperature grown GaAs: microscopic limitations and optimization strategies," *Appl. Phys. Lett.* **74**, 3134 (1999).

- [96] J. F. Whitaker, " Optoelectronic applications of LTMBE III-V materials," *Mater. Sci. Eng.* **B22**, 61 (1993).
- [97] C. Ludwig, J. Kuhl, "Studies of the temporal and spectral shape of terahertz pulses generated from photoconducting switches," *Appl. Phys. Lett.* **69**, 1194 (1996).
- [98] T. Motet, J. Nees, S. Williamson, G. Mourou, "1.4 ps rise-time high-voltage photoconductive switching," *Appl. Phys. Lett.* **59**, 1455 (1991).
- [99] H. S. Loka, P. W. E. Smith, "Ultrafast all-optical switching in an asymmetric Fabry-Perot device using low-temperature-grown GaAs," *IEEE Phot. Tech. Lett.* **10**, 1733 (1998).
- [100] U. Keller, K. J. Weingarten, F. X. Kärtner, D. Kopf, B. Braun, I. D. Jung, R. Fluck, C. Hönninger, N. Matuschek, J. Aus der Au, "Semiconductor saturable absorber mirrors (SESAMs) for femtosecond to nanosecond pulse generation in solid-state lasers," *IEEE J. Sel. Top. Quantum Electron.* **2**, 435 (1996).
- [101] E. S. Harmon, M. R. Melloch, J. M. Woodall, D. D. Nolte, N. Otsuka, C. L. Chang, "Carrier lifetime versus anneal in low temperature growth GaAs," *Appl. Phys. Lett.* **63**, 2248 (1993).
- [102] L.-E. Wernersson, A. Litwin, L. Samuelson, W. Seifert, "Controlled carrier depletion around nano-scale metal discs embedded in GaAs," *Jpn. J. Appl. Phys.* **36**, L 1628 (1997).
- [103] X. Liu, A. Prasad, W. M. Chen, A. Kurpiewski, A. Stoschek, Z. Liliental-Weber, E. R. Weber, "Mechanism responsible for the semi-insulating properties of low-temperature-grown GaAs," *Appl. Phys. Lett.* **65**, 3002 (1994).
- [104] M. Missous, E. H. Rhoderick, "On the Richardson constant for aluminum/gallium arsenide Schottky diodes," *J. of Appl. Phys.* **69**, 7142 (1991).
- [105] T. Dekorsy, T. Pfeifer, W. Kütt, H. Kunz, "Subpicosecond carrier transport in GaAs surface-space-charge fields," *Phys. Rev. B* **47**, 3842 (1993).
- [106] R. Kersting, J. N. Heyman, G. Strasser, K. Unterrainer, "Coherent plasmons in n-doped GaAs," *Phys. Rev. B* **58**, 4553 (1998).
- [107] B. E. A. Saleh, M. C. Teich, *Fundamentals of Photonics* (John Wiley & Sons, Inc., 1991)
- [108] R. Tommasi, P. Langot, F. Vallée, "Femtosecond hole thermalization in bulk GaAs," *Appl. Phys. Lett.* **66**, 1361 (1995).
- [109] P. C. M. Christianen, P. J. v. Hall, H. J. A. Bluyssen, M. R. Leys, L. Drost, J. H. Wolter, "Ultrafast carrier dynamics at a metal-semiconductor interface," *J. Appl. Phys.* **80**, 6831 (1996).
- [110] H. Heesel, S. Hunsche, M. Mikkelsen, T. Dekorsy, K. Leo, H. Kurz, "Dynamics of electric-field screening in a bulk GaAs modulator," *Phys. Rev. B* **47**, 16000 (1993).
- [111] A. Gustafsson, F. Reinhardt, G. Biasiol, E. Kapon, "Low-pressure organometallic chemical vapor deposition of quantum wires on V-grooved substrates," *Appl. Phys. Lett.* **67**, 3673 (1995).

-
- [112] G. Abstreiter, A. Aydinli, J.-P. Leburton, Eds., *Optical spectroscopy of low-dimensional semiconductors*, vol. 344 (Kluwer Academic, Amsterdam, 1997).
- [113] D. Y. Oberli, M.-A. Dupertuis, F. Reinhardt, E. Kapon, "Effect of disorder on the temperature dependence of radiative lifetimes in V-groove quantum wires," *Phys. Rev. B* **59**, 2910 (1999).
- [114] J. E. Fouquet, R. D. Burnham, "Recombination dynamics in GaAs/AlGaAs quantum well structures," *IEEE J. Quantum Electron.* **QE-22**, 1799 (1986).
- [115] R. Eckert, J. M. Freyland, H. Gersen, H. Heinzelmann, G. Schürmann, W. Noell, U. Staufer, N. F. d. Rooij, "Near-field fluorescence imaging with 32 nm resolution based on microfabricated cantilevered probes," *Appl. Phys. Lett.* **77**, 3695 (2000).
- [116] B. J. Kim, J. W. Flamma, E. S. t. Have, M. F. Garcia-Parajo, N. F. v. Hulst, J. Brugger, "Moulded photoplastic probes for Near-field optical applications," *J. Microsc.* **202**, 16 (2001).
- [117] G. Steinmeyer, D. H. Sutter, L. Gallmann, N. Matuschek, U. Keller, "Frontiers in Ultrashort Pulse Generation: Pushing the Limits in Linear and Nonlinear Optics," *Science* **286**, 1507 (1999).
- [118] U. D. Keil, J. R. Jensen, J. M. Hvam, "Transient measurements with an ultrafast scanning tunneling microscope on semiconductor surfaces," *Appl. Phys. Lett.* **72**, 1644 (1998).
- [119] G. M. Steeves, A. Y. Elezzabi, M. R. Freeman, "Nanometer-scale imaging with an ultrafast scanning tunneling microscope," *Appl. Phys. Lett.* **72**, 504 (1998).
- [120] N. N. Khusnatdinov, T. J. Nagle, G. N. Jr., "Ultrafast scanning tunneling microscopy with 1 nm resolution," *Appl. Phys. Lett.* **77**, 4434 (2000).
- [121] K. Takeuchi, A. Mizuhara, "Low-temperature grown GaAs probe for ultrafast electrical signal measurement," *Electron. Lett.* **33**, 325 (1997).
- [122] W. M. Steffens, S. Heisig, U. D. Keil, E. Oesterschulze, "Spatio-temporal imaging of voltage pulses with a laser-gated photoconductive sampling probe," *Appl. Phys. B* **69**, 455 (1999).
- [123] F. Steininger, A. Knorr, T. Stroucken, P. Thomas, S. W. Koch, "Dynamic evolution of spatiotemporally localized electronic wave packets in semiconductor quantum wells," *Physical Review Letters* **77**, 550 (1996).
- [124] F. Steininger, A. Knorr, P. Thomas, S. W. Koch, "The influence of electron-phonon scattering on the spatio-temporal dynamics of electronic wavepackets in semiconductor quantum wells," *Z. Phys. B* **103**, 45 (1997).
- [125] A. Knorr, F. Steininger, B. Hanewinkel, S. Kuckenburg, P. Thomas, S. W. Koch, "Theory of ultrafast spatio-temporal dynamics in semiconductor quantum wells: electronic wavepackets and near-field optics," *Phys. Stat. Sol.* **206**, 139 (1998).
- [126] B. Hanewinkel, A. Knorr, P. Thomas, S. W. Koch, "Near-field dynamics of excitonic wave packets in semiconductor quantum wells," *Phys. Rev. B* **60**, 8975 (1999).

- [127] A. Hartmann, L. Loubies, F. Reinhardt, E. Kapon, "Self-limiting growth of quantum dot heterostructures on nonplanar {111}B substrates," *Appl. Phys. Lett.* **71**, 1314 (1997).
- [128] J. Fricke, R. Nötzel, U. Jahn, H.-P. Schönherr, L. Däweritz, K. H. Ploog, "Patterned growth on GaAs (311)A substrates: Dependence on mesa misalignment and sidewall slope and its application to coupled wire-dot arrays," *J. Appl. Phys.* **86**, 3576 (1999).
- [129] G. Yu, J. Gao, J. C. Hummelen, F. Wudl, A. J. Heeger, "Polymer photovoltaic cells: Enhanced efficiencies via a network of internal donor-acceptor heterojunctions," *Science* **270**, 1789 (1995).
- [130] N. C. Greenham, X. Peng, A. P. Alivisatos, "Charge separation and transport in conjugated-polymer/semiconductor-nanocrystal composites studied by photoluminescence quenching and photoconductivity," *Phys. Rev. B* **54**, 17628 (1996).

Curriculum Vitae

Personal data

Name Marc Achermann
Date of birth June 11th, 1972
Nationality Swiss

School Education

1979 - 1985 *Primarschule St.Gallen*
1985 - 1992 *Kantonsschule St.Gallen*
01 / 1992 *Matura Typus C*

University

1992 - 1998 Study of Physics at the Federal Institute of Technology
Zürich (ETH Zürich), Switzerland
1995 - 1996 Study of Physics at the Federal Institute of Technology
Lausanne (EPFL Lausanne), Switzerland
03 / 1998 *Diplom ETH Zürich*
Diploma thesis: "Ultrafast electron dynamics in silver films
and nanoparticles" (*Laboratoire d'Optique Quantique, Ecole
Polytechnique Paris, France*)
1998 - 2001 Ph.D. studies at the ETH Zürich

Danksagung

An dieser Stelle möchte ich mich herzlich bei den vielen Leuten bedanken, die wesentlich zum Gelingen dieser Arbeit beigetragen haben. Mein besonderer Dank gilt:

Prof. Dr. Ursula Keller, die mir die Möglichkeit gegeben hat, in ihrer Gruppe diese Arbeit auf einem aktuellen und interessanten Gebiet durchzuführen. Sie hat mich während dem ganzen Doktorat motiviert und unterstützt und mir das Vertrauen entgegen gebracht, selbständig die Projekte zu realisieren und deren Resultate zu präsentieren.

PD Dr. Uwe Siegner, der sich nicht nur bereit erklärt hat, als Koreferent zu wirken, sondern mich auch gewissenhaft zuerst in Zürich und später aus Braunschweig betreut hat. Er hat sich immer die Zeit genommen, meinen Papierkram gründlich durchzuschauen, um den richtigen *Flow* zu geben.

Dr. Bettina Nechay, die mir viele der Tricks und Kniffs zur Handhabung des launischen NSOMs beibrachte, und die mich in die NSOM Gemeinschaft einführte.

Rosmarie Ehrsam, für ihre herzliche Unterstützung bei administrativen Angelegenheiten.

der verschworenen Spektroskopiesubgruppe mit Dr. Sebastian Arlt, für seine Ausführungen über Exzitonen, Dr. Jens Kunde, für seine besonderen Fähigkeiten im schnellen Aufdampfen von Aluminium, und Markus Haiml, der LT-GaAs Spezialist und ausdauerndste Bürogenosse.

der Gruppe von Prof. Dr. Eli Kapon, insbesondere Dr. Arno Hartmann, Dr. Yann Ducommun und Dr. Daniel Oberli, für das Wachstum und die Charakterisierung der QWR Proben und ihre Unterstützung bei der Interpretation der teilweise verwirrenden Messungen (*BGR, oder nicht?!).*

der Gruppe von Prof. Dr. Lars Samuelson, im Speziellen Dr. Lars-Erik Wernersson, für die herzliche Zusammenarbeit am W Disk Projekt, und Prof. Dr. Werner Seifert, für das Wachstum der W Disk Proben.

François Morier-Genoud, für das Wachstum der LT-GaAs Halbleiterproben.

Dr. Andreas Schertel, für die FIB-implantierten Quantenfilme.

Christian Fokas, der mir die Geheimnisse des *tube-etching* verriet.

Dr. Alexandre Bouhelier, für seine französisch-schweizerischen Spitzen in der Endphase meiner Doktorarbeit.

meinen Bürogefährten Dr. Bettina Nechay, aMy Dunlop, Lukas Krainer, Markus Haiml und Alex Aschwanden, für die interessanten nicht nur physikalischen Diskussionen.

Reto Härig, der mir ermöglichte, ein bisschen abzuheben und mich dabei fast nie fallen liess.

Lukas Gallmann, der auch bei schlechtem Wetter in den Wald joggen kam.

meinem Diplomanden Martin Steiger, mit dem man sich genüsslich durch Bündner Spezialitäten essen kann.

Ich möchte mich zudem bei allen Mitgliedern der Ultrafast Gruppe herzlich bedanken für ihre Hilfsbereitschaft und das aussergewöhnlich angenehme Arbeitsklima.

Ferner gilt mein Dank meiner Familie und meinen WG-Mitbewohnern.

Mein letzter und ganz spezieller Dank geht an Sibylle für ihre Freundschaft bei all den Hochs und Tiefs ("Und schon wieder ist eine Spitze zerbrochen!") während der ganzen Doktoratszeit.

Zürich, Oktober 2001



(M. Achermann)